

Titre: Design of a Grasping and Machining end Effector for Thin
Title: Aluminium Panel

Auteur: Apple Mahmud
Author:

Date: 2015

Type: Mémoire ou thèse / Dissertation or Thesis

Référence: Mahmud, A. (2015). Design of a Grasping and Machining end Effector for Thin
Citation: Aluminium Panel [Thèse de doctorat, École Polytechnique de Montréal].
PolyPublie. <https://publications.polymtl.ca/1776/>

 **Document en libre accès dans PolyPublie**
Open Access document in PolyPublie

URL de PolyPublie: <https://publications.polymtl.ca/1776/>
PolyPublie URL:

**Directeurs de
recherche:** J. R. René Mayer, & Luc Baron
Advisors:

Programme: Génie mécanique
Program:

UNIVERSITÉ DE MONTRÉAL

DESIGN OF A GRASPING AND MACHINING END EFFECTOR FOR THIN ALUMINUM
PANEL

APPLE MAHMUD

DÉPARTEMENT DE GÉNIE MÉCANIQUE
ÉCOLE POLYTECHNIQUE DE MONTRÉAL

THÈSE PRÉSENTÉE EN VUE DE L'OBTENTION
DU DIPLÔME DE PHILOSOPHIAE DOCTOR
(GÉNIE MÉCANIQUE)

JUILLET 2015

© Apple Mahmud, 2015.

UNIVERSITÉ DE MONTRÉAL

ÉCOLE POLYTECHNIQUE DE MONTRÉAL

Cette thèse intitulée :

DESIGN OF A GRASPING AND MACHINING END EFFECTOR FOR THIN ALUMINUM
PANEL

présentée par : MAHMUD Apple

en vue de l'obtention du diplôme de : Philosophiae Doctor

a été dûment acceptée par le jury d'examen constitué de :

M. BALAZINSKI Marek, Docteur ès Sciences, président

M. MAYER René, Ph. D., membre et directeur de recherche

M. BARON Luc, Ph. D., membre et codirecteur de recherche

M. ACHICHE Sofiane, Ph. D., membre

M. BONEV Ilian, Ph. D., membre externe

DEDICATION

I dedicate this work to my mother and father.

ACKNOWLEDGEMENTS

I would like to express my deepest gratitude to my research supervisor Prof. *Rene Mayer* for extensive support, excellent guidance and warm encouragement during my research as well as for the trust he placed in me to work in my own way the lessons I learned from each of you which will remain useful for a lifetime. In addition to his help in writing the articles, he has always given very generously his time to discuss various aspects of this project. Special thanks to my co-director Prof. *Luc Baron* who has given very precious advices during this project.

I would like to thank NSERC for financial support of this project. I would also like to thank my friends, my colleagues and other members of CRIAQ 412 research team from bombardier who helped me during this study. Special thanks to Jean-François Lalonde and Benjamin Larregain from Bombardier Aerospace.

Technical guidance and instrumental help from Mathieu Côté and Christian Piette on behalf of Olympus NDT Canada Inc was tremendous.

I wish to express my gratitude to all secretaries of Department de Génie Mécanique and laboratory technician Vincent Mayer and Guy Genome at laboratoire de recherche en fabrication virtuelle (LRFV) in Ecole Polytechnique de Montreal. I would also like to convey my gratitude to all my committee members for accepting to be members of the jury.

Words cannot express how much I am thankful to my dearest parents for their unconditional love, support and dedication and my wife continuous support and inspiration.

RÉSUMÉ

Ce projet de recherche a pour principal objectif l'usinage par fraisage mécanique de poches dans des panneaux minces d'avion. Cette opération sera effectuée en utilisant un robot manipulateur. L'une des exigences clés de cette recherche est de maintenir l'épaisseur restante du panneau à $\pm 0,002$ pouces ($\pm 0,050$ mm). Compte tenu d'une variation de 5% de l'épaisseur initiale accompagnée d'une forme à double courbure et d'une faible rigidité, cette tolérance est assez difficile à atteindre. Un mécanisme d'appui en continu de l'autre côté du panneau peut résoudre le problème de la flexion et de la déformation du panneau flexible. Un capteur d'épaisseur, capable d'actualiser régulièrement la valeur de l'épaisseur, permet à une boucle de rétroaction de contrôler la profondeur de coupe. Un mandrin magnétique et un capteur d'épaisseur à ultrasons sont largement étudiés pour leur potentialité à résoudre ce problème d'usinage.

La maquette numérique du prototype a été développée sous CATIA V5. Certaines composantes comme le moteur de la broche et quelques parties du capteur magnétique ont été intégrés en interne lors du montage du module maître/esclave. Le prototype a été testé sur une machine à commande numérique pour un panneau plat. Le banc de la machine était suffisant pour tester la validité de la boucle de rétroaction, mais ne pouvait tester l'usinage du panneau à double courbure. Après quelques essais avec rétroaction, on a observé que le capteur à ultrasons n'a pas été en mesure de détecter une valeur d'épaisseur stable en raison de l'approvisionnement interrompu en liquide de couplage (eau). Ceci a entraîné une variation d'épaisseur visible sur la surface usinée du panneau. Le problème identifié a été confirmé suite à quelques essais sans rétroaction qui ont induit une épaisseur plus constante avec une surface usinée plus lisse. Cette série d'expériences vise à répondre à la question de recherche principale qui est de savoir s'il est possible d'usiner un panneau mince avec un niveau de tolérance suffisant.

Quelques expériences ont été effectuées afin de connaître les forces nécessaires à l'appui et à l'usinage de l'effecteur. Le calcul des forces avec l'outil de coupe torique, en considérant l'inclinaison de l'outil, aide à établir une procédure pour déterminer la force de serrage minimale. Pour ce, on a supposé que la force minimale est équivalente à la force de poussée maximale (force perpendiculaire au panneau) en opération de fraisage.

Le module esclave qui suit le module maître en restant au centre de la surface de l'outil a été confronté à la force de frottement. Il était donc nécessaire de modéliser le mouvement de

réponse du module esclave résultant du mouvement du module maître. Un modèle de mouvement sous forme de fonction de transfert a été établi pour relier le mouvement de l'esclave à celui du maître. Il a été observé que la masse du module esclave et la rigidité latérale magnétique jouent un rôle crucial contre la force de frottement.

En analysant la rigidité latérale magnétique, il était nécessaire de définir les propriétés magnétiques latérales des aimants cylindriques permanents qui attirent le module esclave vers le module maître. Des expériences de mesure des forces magnétiques latérales ont permis de proposer une équation mathématique pouvant prédire les forces magnétiques latérales en considérant le déplacement latéral entre la paire magnétique à l'intérieur des groupes.

Mots-clés: usinage robotisé, effecteur préhenseur-usineur, capteurs d'épaisseur, poches, panneau mince.

ABSTRACT

This research considers mechanical milling of thin aircraft panel as its prime objective. Mechanical milling will be conducted using a robot manipulator. One of the key requirements of this research is to maintain the remaining panel thickness within ± 0.002 inch (± 0.050 mm). Given the initial panel thickness variation of 5% along with its double curvature shape and low stiffness, this tolerance is quite challenging. A continuous support mechanism from the opposite side of the panel may solve the problem of deflection and deformation of the flexible panel. A highly sensitive thickness sensor that can regularly update the thickness value could be adapted to a feedback loop to get a precise dynamic depth of cut. A magnetic chuck and ultrasonic thickness sensor will be investigated for their ability to solve this problem of thin panel mechanical machining.

Considering the required specification a prototype model has been developed in CATIA V5. The model has been implemented collecting all required components mentioned in the design. Other than those purchased components like spindle motor, magnets and sensor a few parts have been in-house built while assembling the master and slave module. The prototype has been tested inside a CNC machine tool for a flat skin panel. The CNC machine bed was sufficient to test the feedback loop validity but could not test the end effector capability for double curvature panel machinability. After a few tests with feedback it has been observed that the ultrasonic sensor was not able to get a stable thickness value due to interrupted supply of coupling liquid (water) which resulted in a variation in the skin panel floor bed thickness. The identified problem has been confirmed with a few more tests without feedback which resulted in smoother floor bed thickness. This series of experiment answer the prime research question of whether it is possible to mill skin panel with such level of tolerance.

A few experiments have been conducted to determine how much force is needed to accomplish the grasping and machining functions. Torus cutter based milling force calculation considering the tilting angle helped to establish a procedure for determining the minimum clamping force. To determine the required minimum clamping force it has been assumed that minimum clamping force is equivalent to the maximum thrust force (perpendicular force on the skin panel) in milling operation.

The slave module is required to closely follow the master module despite frictional forces. So it was necessary to model the slave response motion resulting from the master motion. A transfer function based motion model has been established to relate the slave motion in response to master motion. It was observed that slave mass and lateral magnetic stiffness play vital roles while moving against the frictional constraint.

While analyzing lateral magnetic stiffness it was necessary to define the lateral magnetic properties of cylindrical permanent magnet which were included in the grasping and machining end effector. Experimental measurements of the lateral magnetic forces allowed concluding a mathematical equation which can predict the lateral magnetic forces considering the lateral displacement among the magnetic pair within groups.

Keywords: robotic milling, grasping end effector, thickness sensor, pockets, skin pocket, thin panel.

TABLE OF CONTENTS

DEDICATION	III
ACKNOWLEDGEMENTS	IV
RÉSUMÉ.....	V
ABSTRACT	VII
TABLES OF CONTENTS	IX
LIST OF TABLES	XII
LIST OF FIGURES.....	XIII
LIST OF SYMBOLS AND ABBREVIATIONS.....	XVIII
CHAPTER 1 INTRODUCTION.....	1
CHAPTER 2 LITERATURE REVIEW	3
2.1 Skin panel milling	3
2.1.1 First machine by Martinez.....	3
2.1.2 Second solution by Hamann.....	4
2.1.3 Panczuk-Foissac mirror milling system	6
2.2 Minimum clamping force determination.....	7
2.3 Lateral sliding motion modeling	8
2.4 Lateral magnetic force modeling.....	8
CHAPTER 3 OBJECTIVES	10
3.1 Problem formulation	10
3.1.1 Research questions	11
3.1.2 General objectives	11
3.1.3 Specific objectives.....	11

3.1.4 Hypothesis.....	11
3.1.5 Design specification	12
3.1.6 Organization of the articles	12
CHAPTER 4 ARTICLE 1: MAGNETIC ATTRACTION FORCES BETWEEN PERMANENT MAGNET GROUP ARRAYS IN A MOBILE MAGNETIC CLAMP FOR POCKET MACHINING	15
4.1 Introduction	15
4.2 Theoretical framework	17
4.3 Experimental setup.....	26
4.4 Results and verification.....	30
4.5 Conclusion.....	40
REFERENCES.....	41
CHAPTER 5 ARTICLE 2: MECHANICAL POCKET MILLING OF THIN ALUMINIUM PANEL WITH A GRASPING AND MACHINING END EFFECTOR	43
5.1 Introduction	43
5.2 Literature review	44
5.3 Concept development	47
5.4 Mechanical design.....	48
5.5 Prototype development.....	50
Magnet selection and orientation	51
Sensor selection criteria	53
Servo motor selection.....	54
Spindle motor selection.....	55
Part assembly.....	57
5.6 Feedback control system	57

5.7	Experiments and results	60
5.8	Conclusion.....	66
REFERENCES.....		67
CHAPTER 6 ARTICLE 3: DETERMINING THE MINIMUM CLAMPING FORCE BY CUTTING FORCE SIMULATION IN AEROSPACE FUSELAGE POCKET MACHINING..		69
6.1	Introduction	69
6.2	Thrust force model	71
6.3	Experimental setup.....	76
6.4	Simulated thrust force	78
6.5	Results and verification.....	86
6.6	Conclusion.....	87
REFERENCES.....		87
CHAPTER 7 ARTICLE 4: MODELING OF LATERALLY SLIDING MOTION OF A MAGNETIC CLAM		89
7.1	Introduction	89
7.2	Transfer function modeling.....	91
7.3	System parameter identification.....	96
7.4	Experiments and results	106
7.5	Conclusion.....	108
REFERENCES.....		109
CHAPTER 8 GENERAL DISCUSSION.....		114
CHAPTER 9 CONCLUSION AND RECOMMENDATION		116
9.1	Conclusion.....	116
9.2	Recommendation.....	117
CHAPTER 10 BIBLIOGRAPHY		118

LIST OF TABLES

Table 1: Magnetic performance comparison for common permanent magnet(Wikipedia 2014) ..	51
Table 2: Lists the results for all three spindle power selection equation.	56
Table 3: System identification experiments results summary	101
Table 4: Friction force at different plate thickness	105

LIST OF FIGURES

Figure 1: First machine for machining large and complicated shape panel (Martinez 1992).....	3
Figure 2: Hamann (2007) device for machining aircraft panel	5
Figure 3: Mirror milling systems for machining of panels. (Panczuk and Foissac 2010)	6
Figure 4: Axial and lateral magnetic force direction in the mobile magnetic clamp	16
Figure 5: Three magnet group (each group comprised of three individual magnets) located in the master array and slave array	18
Figure 6: Ball transfer unit are placed at the centroid of the equilateral triangle with magnets at its vertices	19
Figure 7: A magnet group (M1, M2 and M3) in the master array coaxial to another magnet group (S1, S2 and S3) in the slave array in static (nominal) condition.....	20
Figure 8: A magnet group (M1, M2 and M3) in the master array moves a distance r in the Y-axis direction with respect to the nominally coaxial magnet group (S1, S2 and S3) in the slave array.....	22
Figure 9: A magnet group (M1, M2 and M3) in master array moves a distance r in the X-axis direction with respect to coaxial magnet group (S1, S2 and S3) in slave array	23
Figure 10: Master module (left of panel) and slave module (right of panel) magnet array in a magnetic grasping milling prototype setup	27
Figure 11: Master module attached to the CNC spindle and slave module fixed to the top of the dynamometer itself attached to the machine tool table	28
Figure 12: Master magnet array with lateral displacement along Y-axis with respect to the slave magnet array	29
Figure 13: Master magnet array is lateral displacement along X-axis with respect to the slave magnet array	29
Figure 14: Axial force and lateral force one coaxial magnet pair with axial gaps x of 5.5 and 6.5 mm.....	31

Figure 15: Calculated vs measured axial force for one pair of magnets with axial gaps x of 5.5 and 6.5 mm.....	32
Figure 16: Calculated vs measured lateral force for one pair of magnets with axial gaps x of 5.5 and 6.5 mm.....	33
Figure 17: Axial force and lateral force with respect to lateral displacement in Y axis direction between magnet array at 5.5 and 6.5 mm axial gaps, x	34
Figure 18: Calculated vs measured axial force with respect to lateral displacement in Y axis direction between magnet array at 5.5 and 6.5 mm axial gaps, x	35
Figure 19: Calculated vs measured lateral force with respect to lateral displacement in Y axis direction between magnet array at 5.5 and 6.5 axial gaps, x	36
Figure 20: Axial force and lateral force with respect to lateral displacement in X axis direction between magnet array at 5.5 and 6.5 axial gaps, x	37
Figure 21: Calculated vs measured axial force with respect to lateral displacement in X -axis direction between magnet array at 5.5 and 6.5 axial gaps x	38
Figure 22: Calculated vs measured lateral force with respect to lateral displacement in X -axis direction between magnet array at 5.5 and 6.5 axial gaps x	39
Figure 23: First machine for machining large and complicated shape panel (Martinez 1992).....	44
Figure 24: Hamann (2007) device for machining aircraft panel (Hamann 2007).....	45
Figure 25: Mirror milling systems for machining of panels. (Panczuk and Foissac 2010)	46
Figure 26: Conceptual design of the grasping and machining end effector.....	47
Figure 27: Feedback control loop.....	48
Figure 28: CATIA V5 model for the end effector	49
Figure 29: Double gimbal mechanism internal setup.....	50
Figure 30: Typical magnet to magnet pull (K&J magnetics 2014).....	52
Figure 31: Ball transfer unit can take up form pocket area to uncut area over the skin panel.	53

Figure 32: Bubbler type transducer ensures liquid in place by continuous supply (Olympus 2014)	54
Figure 33: Spring supported bubbler transducer assembly pushes against the panel surface.....	54
Figure 34: Complete end effector assembly.....	57
Figure 35: Stepper motor control box	58
Figure 36: Lab View program flow chart for depth of cut (DOC) control.	59
Figure 37: Experimental setup viewed from the master side	60
Figure 38: Experimental setup from slave side.....	61
Figure 39: Interrupted feedback caused uneven remaining thickness.....	62
Figure 40: Random floor thickness in close loop pocket milling showing high thickness variation.	63
Figure 41: Open loop milling results in smoother surface finish.....	64
Figure 42: Random floor thickness in open loop pocket milling showing lower thickness variation.....	65
Figure 43: Concept of a grasping end effector fixed on KUKA 500 KR-2 MT industrial robot for double curved skin panel pocket milling.....	66
Figure 44: Average chip thickness $emoy(\theta)$ and axial engagement da	72
Figure 45: Axial engagement da for constant depth of cut p	73
Figure 46: Kistler dynamometer fixed on the CNC machine bed (model-HURON KX8).....	76
Figure 47: LabView based data acquisition system with Kistler Dynamometer	77
Figure 48: Measured forces F_x , F_y and F_z in fixed workpiece reference frame.....	78
Figure 49: Fixed workpiece reference system to local reference system force components conversion	79
Figure 50: Experimental force data (A: fixed workpiece reference) calculated force data (B: local reference system) at $\alpha = 0 \text{ deg}$	80

Figure 51: A: axial engagement, da B: average chip thickness, emoy at different tilting angle ($\alpha = 0, 5, 10, 15 \text{ deg}$).....	81
Figure 52: Simulated verses measured cutting forces with no tilting angle ($\alpha = 0 \text{ deg}$) in fixed framework	82
Figure 53: Thrust force at 5 degree tilting angle ($\alpha = 5 \text{ deg}$).....	83
Figure 54: Thrust force at 10 degree tilting angle ($\alpha = 10 \text{ deg}$)	84
Figure 55: Thrust force at 15 degree titling angle ($\alpha = 15 \text{ deg}$)	85
Figure 56: 0 to 90 degree tilt angle and corresponding thrust force	86
Figure 57: General schematic diagram of the grasping machining end effector concept.....	90
Figure 58: Master with three extended leg (left). Slave with three sets of permanent magnets (right) (Chouinard 2011)	90
Figure 59: Master-slave magnetic forces in a simplified 2D view	92
Figure 60: Free body diagram for panel-master-slave	93
Figure 61: Modified free body diagram for master and slave.....	94
Figure 62: Master-slave equivalent mechanical system without the panel and associated friction and milling force	94
Figure 63: Lateral stiffness measurement by manual lateral force measurement with spring balance.....	97
Figure 64: Test setup for system parameter identification.....	98
Figure 65: Displacement graph for a 5 mm gap between the master and slave.....	99
Figure 66: A 5 mm gap between the master and slave is maintained by a string arrangement ...	100
Figure 67: Stiffness reduces as the master-slave gap increases (thicker plate)	102
Figure 68: Plate between master and slave placed where accelerometer is positioned on the slave	103
Figure 69: Slave displacement result for the impact hammer test of Figure 68	104
Figure 70: Test setup for axial force measurement by a spring balance	105

Figure 71: Simultaneous acceleration data acquisition for both master and slave	106
Figure 72: Comparison of transfer function based simulated motion to the actual slave motion (master slave gap 5.04 mm)	107
Figure 73: Comparison of transfer function based simulated motion to the actual slave motion (master slave gap 7.55mm)	108

LIST OF SYMBOLS AND ABBREVIATIONS

CNC	Computer Numerical Control
HP	Horse Power
T	Torque
DOC	Depth of Cut
Al-Li	Aluminum lithium Alloy
MMS	Mirror Milling System
f_t	Feed per tooth
$K_t(\theta)$	Cutting force coefficient
K_r	Radial to tangential force ratio
K_a	Axial to tangential force ratio
d_a	Axial engagement
$emoy(\theta)$	Average chip thickness
F_r	Radial magnetic force
K_r	Magnetic lateral stiffness
C_{eq}	Equivalent viscous damping coefficient
δ	Logarithmic decrement
ω_d	Damped natural frequency
ω_n	Undamped natural frequency
K_d	Magnetostatic energy constant
J_0	Bessel function of first kind of order 0
J_1	Bessel function of first kind of order 1
x	Axial gap
r	Lateral displacement.

CHAPTER 1 INTRODUCTION

Aircraft weight and manufacturing cost are two important concerns for aircraft manufacturers. Less weight means less fuel consumption which drives the aircraft technologist to be more directed towards weight reducing innovation. Nowadays, like all other product manufacturing, aircraft manufactures are considering the air transport impact on the environment. An aircraft starts to impact the environment from its manufacturing to its ultimate decommissioning while fuel consumption continues during the whole life cycle.

To construct a more environmentally friendly aircraft, manufacturers are putting more effort into research and development to increase fuel efficiency and are now setting new programs to achieve their high vision of fuel efficiency. Bombardier, one of the biggest North American aircraft manufacturer, announced substantial reductions in fuel consumption of around 20% in 2009 (Scott, Boehm et al. 2009). The production of the aircraft is also considered for the use of cleaner processes. Chemical milling impacts the environment by releasing waste to the environment. The replacement of the existing chemical milling with mechanical milling is getting more focused in this regard.

In some recent invention it has been shown that mechanical milling can successfully replace current chemical milling. Advanced Green Panels(Langdon 1996) project which has been completed by European Union and Airbus is the latest advancement towards mechanical milling. This system uses two independent five axis machines on opposite sides of the same skin panel moving in a coordinated manner.

The main aim of the grasping and machining end effector development research is to design a system that will do the same task with one single machine with a simple passive support system. The research will try to answer the research questions associated with the project of developing a grasping and machining end effector. The first research question “whether it is possible to mill such precision tolerance by magnetic clamping?” has been investigated by few machining operation inside the CNC machine in a laboratory setup.

The second question “how much force needs to be supported by the magnetic clamp so that the milling operation can be done without workpiece (skin panel) displacement or vibration?” It has been assumed that the clamping force much withstand the milling thrust force (force perpendicular to the skin panel coming from machining operation). So the minimum

clamping force should be at least the maximum milling thrust force. A torus cutter has been taken into consideration with different tilting angle and corresponding milling thrust force has been simulated to determine the maximum force. This maximum force has been declared as the minimum clamping force.

The third question is “how the slave module design could be optimized so that slave can follow the master smoothly without stick slip motion?” a master to slave motion transfer function has been established which focuses on magnetic stiffness damping constant and mass requirement of the slave design.

The fourth question aroused while answering the first question. The first question focuses on what is the required force for grasping and machining end effector. The fourth question “what axial and lateral forces are generated by a particular assembly pattern of magnets?” The slave module needs to support the milling thrust force so axial force play the vital role. But the slave module also has to overcome the friction force to remain close to the center point of the master, so the lateral magnetic force is also very important.

CHAPTER 2 LITERATURE REVIEW

2.1 Skin panel milling

Machining of shallow pockets in thin panel is a relatively new field of study. Mechanical milling method that can replace the chemical milling has already been developed by the European Aerospace Industry. Three distinctive ways of thin panel mechanical milling have been invented over the last two decades. The invented processes have a few drawbacks.

2.1.1 First machine by Martinez

In the aerospace and shipping industries, large parts are difficult to handle and fasten during the machining process. A machine was patented to support and machine these type of parts by Martinez (Martinez 1992).

The machine is a bridge type which moves along a track. The workpiece support includes multiple modules which transversely align and move independently along the tracks. All of the modules are equipped with multiple columns which can move vertically to fix the workpieces at their upper end. A computer ensures the necessary movement in all three perpendicular directions to allow the automatic positioning of the fixing members. Fixing members are manipulated to place them at the perfect positions for supporting and gripping the workpieces.

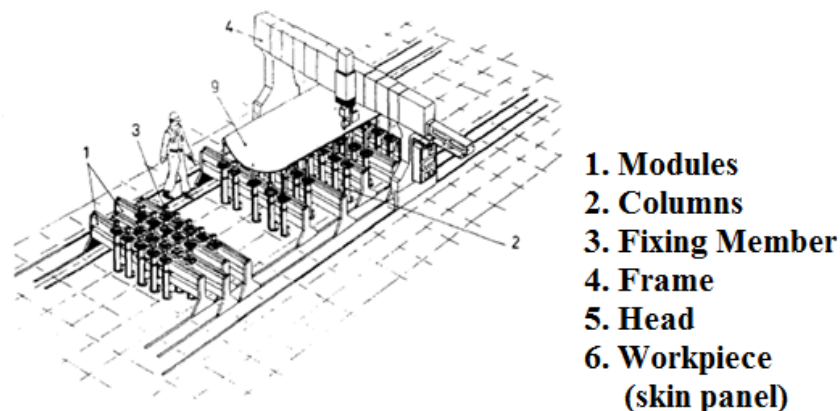


Figure 1: First machine for machining large and complicated shape panel (Martinez 1992)

The machine can adapt to a variety of panel shapes without any specific template requirement and a multi-axis machining head allows machining of double curvature panels. A large number of motion controlling motors for frame, modules and even for each column which

needs to be independently controlled makes the system complicated to operate. Due to this vertical machining process chip evacuation is also a concern. The machine was not highly precise due to panel deflection between two neighboring columns. The thin aluminum panel is not rigid enough to counter the machining force.

2.1.2 Second solution by Hamann

Hamann patented one specialized process and device for machining large thin panels (Hamann 2007). The machine ensures isostatic positioning to one of the surfaces of a panel avoiding hyperstatism. Two registration holes located on the panel periphery at two opposite side and three reference contact points on the panel secures the isostatic positioning. At least two positioning stops, multiple mobile and prehensile suction cup and suction cup locking system holds the complex shape panel without introducing fastening stresses. Suction cups are uniformly distributed where stops are spaced less than 150 mm.

In addition to this positioning system there is a mean for measuring the actual shape of the surface of the panel. Each of the suction cups has sensors which measure the distance of panel surface from base. Sensor signals are interpolated to calculate the shape of the panel surface. A milling trajectory is calculated considering the interpolated surface as a reference plane. A multi-axis machining head follows the trajectory keeping perpendicular to the machining window. Every machining window needs to adjust the holding stops and suction cups at successive displacement and location.

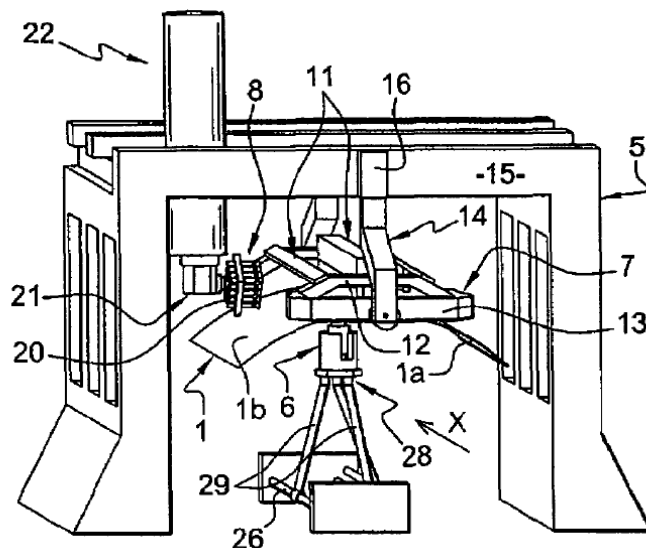


Figure 2: Hamann (2007) device for machining aircraft panel

Figure 2 shows the structure of the machine (Hamann 2007). “Panel 1 is machined on the geometrically known surface 1a which is the concave internal surface and 1b is the reference surface. The multi-axis machining head 6 is under the panel 1. Means 7 supports and position the panel carried by the gantry 5. Means 8 holds upper convex surface 1b of the panel 1. The panel 1 is supported perpendicular by the three horizontal beams assembly 11. Assembly 11 is attached to the two swing bars 12. Beams and swings bars are perpendicular. Swings bars end are held by clamps 13. The clamps 13 are in turn taken up by arms 14. Arms 14 can slide along vertical axis on cross piece 15 with the help of sliding coupling 16. The head 21 can be moved manipulator 22. Suction cup 20 installed on head 21. The machining head 6 can slides on guides 26 and can also swivel by the ball and socket joint 28 located between head 6 and support feet 29.”

The process calculates the machining trajectory referencing to the external surface (opposite side of machining surface). The stretching or drawing processing does not generate a uniform thickness on the whole surface of the panel. This device takes into account the instantaneous shape variation, where thickness variation is also needed to consider for a precise control of depth precision.

Hamann mentions a precision accuracy of less than 0.2 mm whereas the current project aims to attain a tolerance of ± 0.050 mm. This machine is bulky with at least 50 different machine components and complex controls for positioning, fitting of window and trajectory correction.

2.1.3 Panczuk-Foissac mirror milling system

The latest solutions developed for thin aircraft panel machining of co-ordinated motion. These solutions are more known as Mirror Milling Systems (MMS). Hamann (Hamann, 2009) and Panczuk-Foissac (Panczuk and Foissac, 2010) both solved the problem on behalf of Airbus France.

In Hamann solution (Hamann 2009), a tool is applied on the first surface of the panel and the numerically controlled machine positions this tool. The machining force exerted to the thin panel is counter-balanced by a multi-axial mobile support which is usually a metallic sphere. The mobile support moves along the Cartesian axes as well as rotates along two rotational axes to mirror the machining head.

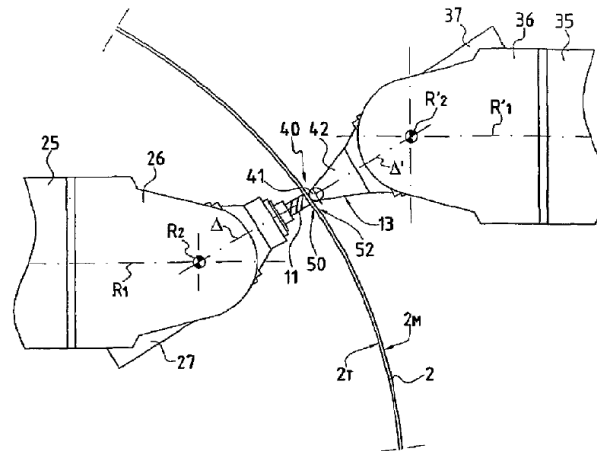


Figure 3: Mirror milling systems for machining of panels. (Panczuk and Foissac 2010)

Figure 3 describes the main feature of the mirror milling system (Panczuk and Foissac 2010). “The machining operation is favoured by the kinetics of the end of arms 25 and 26 and of the support 26 around axes R_1 , R_2 and $R'1$ and $R'2$. The tool bearing head 27 fits on to the head support 26 which is moved by a telescopic arm 25. On the other side head support 36 is mounted on the telescopic arm 35. A retention-element-carrying head 37 is connected to retention element 13. The body 42 has a tapered shape containing sphere 41 at the end 40. Panel 2 has a retention face 2M and machining face 2T. Working area is 50 where 52 is retention area. Tool bearing head 27 has the tool 11 doing the machining job.”

In Panczuk-Foissac solution (Panczuk and Foissac 2010), one machining tool on the machining face and one retention element on the retention face each are having at least five axes of motion to follow a coordinated movement. The panel is oriented more or less vertical allowing gravitational chip removal.

Scanning is performed by an optical sensor mounted on the machining head to determine the actual shape and form of the panel. This allows the machine to work with a wide range of panel forms where the real and nominal forms are different caused by uneven loss of thickness during the drawing process.

However, these solutions and the machines involved are very expensive since in both cases large and complex machines are necessary. Both sides require a multi axis mechanical system and a complex synchronization of the motion of the systems on opposite sides.

2.2 Minimum clamping force determination

While designing the end effector the first consideration was how much force should be supported against the skin panel by the clamp. Finite-element (FE) modeling approach is very common in clamping force optimization. Due to large model size and greater computational cost they are not efficient. Genetic algorithm based fixture layout and clamping force optimization method (Liu, Wang et al. 2012) was proposed with a reduced matrix size for FEM balance equation.

Both rigid body and elastic contacts method has been developed for clamping force optimization. Considering the workpiece and the fixture as perfectly rigid body Wang et al. (Wang and Pelinescu 2003) solved clamping force optimization model. Representing the fixture-workpiece contact as elastic contacts, Li et al (Li and Melkote 2001) estimated optimum clamping force in the case of multiple clamp fixture.

Contact forces for known clamping forces have been predicted by Xiong et al. (Xiongand, Xiong et al. 2003) using nonlinear programming. Wang and Pelinescu et al. (Wang and Pelinescu 2003) used constrained quadratic optimization programming. Computational intelligence Particle Swarm Optimization (PSO) techniques featuring computational intelligence has been used for clamping force optimization by Deng and Melkote (Deng and Melkote 2006). Balancing force-moment method and the coulomb static friction law were used to determine

minimum clamping force to hold the workpiece without deformation by S. Selvakumar et al. (Selvakumar, Arulshri et al. 2010)

The prime drawbacks of these aforementioned methods are that they are developed assuming that the workpiece and clamp contact is static. The magnetic grasping and machining end effector is different, here the clamp slides over the workpiece (skin panel).

2.3 Lateral sliding motion modeling

The slave module follows the master module motion by lateral sliding motion. Lateral sliding occurs due to lateral magnetic forces between two sets of magnetic unit such as magnetic couplings. In case of magnetic coupling torque is transmitted from inner rotor to outer rotor without any radial displacement. P. Elies (Elies and Lemarquand 1999) analyzed this radial stability characteristics in transmitting torque through air gap.

In a permanent magnet bearing there are two different magnetic attraction forces, axial and radial. J.P. Yonnet (Yonnet 1981) defined lateral magnetic stiffness while discussing radial magnetic properties in magnetic bearing and couplings. D. Vokoun et al. (Vokoun, Beleggia et al. 2009) calculated the attraction force between two cylindrical permanent magnets with a common axis. The calculation also estimated the axial attraction force when there is a lateral gap between the couple magnets. This static model is not able to predict whether the slave module is lagging behind by stick-slip motion or perfectly following the master.

Lateral sliding motion has been modeled based on a motion transfer function from master to slave using the concept of magnetic stiffness as defined by J.P. Yonnet (Yonnet 1981). His transfer function has been evaluated against real experimental results obtained from inside laboratory test.

2.4 Lateral magnetic force modeling

According to the proposed design of the grasping and machining end effector, there are three closely located pairs of cylindrical magnets providing the support force to keep the panel in position and the drag force to the slave module for sliding. Support force results from axial magnetic attraction force and drag forces comes from lateral magnetic attraction force.

Fictitious magnetization charges and the discretization technique were used by Vučković et al. (Vučković, Ilić et al. 2013) whom developed a semi-analytical approach to estimate magnetic levitation force between two laterally displaced cylindrical permanent magnet.

Mutual inductance (axial force) between two axially magnetized cylindrical magnet has been studied and expressed analytically by Ravaud et al. (Ravaud, Lemarquand et al. 2010). Robertson et al. (Robertson, Cazzolato et al. 2011) proposed a simplified expression which reduce computational time.

Agashe and Arnold (Agashe and Arnold 2008) exploited Kelvin formula to analyze the attraction forces between two uniformly magnetized cylindrical magnet. Vokoun et al. (Vokoun, Beleggia et al. 2009) used a Bessel function based attraction force equation to elaborate axial force for more than two cylindrical magnets with the special case of two groups magnet set each comprising four magnets. Later Vokoun et al. (Vokoun, Tomassetti et al. 2011) generalized the attraction force equation for two infinite arrays of cylindrical magnet.

Frictional forces hinder the slave motion to perfectly follow the master motion which results in a lateral displacement between the master and slave module. Vokoun's Bessel function based equations are satisfactory to explain the axial magnetic forces while a lateral gap is introduced. But lateral magnetic forces which impart the drag force yet need to be modeled.

CHAPTER 3 OBJECTIVES

3.1 Problem formulation

Aircraft weight reduction is an important issue for aerospace industry. So the aluminum or Al-Li skin panels need to be as thin as possible. Currently, the thinning tasks are accomplished by creating pockets in the skin panel by chemical machining. Unfortunately, this chemical machining process ends with chemical pollutants to the environment. Most of the chemicals such as cleaning solutions, etchants, strippers etc. are very hazardous liquids. Specially, etchants are very dangerous for workers (Cakir, Yardimeden et al. 2007). With the growth of the aerospace industry this issue of health, safety and environmental pollution is getting more and more attention since a decade or so. So, replacing this industrial chemical milling process with a lower emission and more environment friendly process is sought. Mechanical milling is promising in this case because this process finishes with recyclable metal chips and eliminates the requirement for costly etchant disposal and metal recovery from waste etchants.

Chemical milling also uses more electricity compared to mechanical milling and produces much carbon dioxide whereas mechanical milling is carbon dioxide free (Langdon 1996). Due to the previous stage of stretching most of the panel gets high variation of initial thickness. Chemical machining process has a constant material removal rate (MRR). Since the panel has initial thickness variation and a constant thickness is removed, the remaining pocket floor thickness is irregular and imprecise. Applying mechanical milling is also critical due to the initial thickness variation because a single depth of cut cannot assure a fixed remaining thickness of the panel.

Chemical milling process is not capable of attaining different depth of cut in a single operation. One single operation provides one specific depth of cut depending on the exposure time to an etchant. So there is a long process cycle of aircraft thinning operation composed of several steps for different depth of cut.

One of the characteristic of aircraft panels is double curvature. Though five axis CNC milling or six degree freedom robotic milling can easily machine a double curvature plane, here the scenario is complicated due to thinness. Low stiffness of thin panel creates problem by unpredictable deformation during cutting operation. The greatest challenge is to maintain high precision in the pocket floor remaining thickness.

3.1.1 Research questions

- How can the remaining panel thickness be maintained according to the specified level of accuracy while maintaining higher cutting efficiency?
- It is possible to machine a double curvature skin panel with a grasping and machining end effector?
- How much clamping force must be supported by the grasping and machining end effector for a milling operation?
- How can the slave module design be optimized so that the slave can follow the master smoothly without stick slip motion?
- Can a model be established between the magnet properties and the required axial and lateral forces between the master and slave modules?

3.1.2 General objectives

Develop an automated mechanical milling system assisted by an industrial manipulator that is able to mill pockets in a thin Al-Li skin of double curvature form.

3.1.3 Specific objectives

- Develop a grasping mechanism that will hold the thin skin panel to counteract milling force and integratable to a manipulator;
- Develop a simplified passive mechanism to allow the milling spindle tilting relative to the skin panel leading to higher cutting efficiency;
- Integrate a feedback control loop with sensors to ensure the precise tolerance (± 0.002 inch / ± 0.050 mm) of the cut.
- Model the lateral sliding motion of a magnetic clamp.

3.1.4 Hypothesis

A grasping and machining end effector will be implemented to accomplish the purpose of mechanical milling of pockets in aluminum or Al-Li skin panel. A well-equipped clamping technique can restrict the thin skin deformation and make it more resistant to lateral friction forces. The end effector will start material removal by a milling cutter. Sensory feedback of the

remaining thickness will ensure the high precision tolerance allowance. The robotic manipulator will move on the skin surface according the pre-specified pocket dimension and the self-feed spindle motion of the milling cutter will provide depth of the cut for making shallow pockets in the skin panel.

3.1.5 Design specification

- The design must use magnetic forces as a medium of grasping mechanism following the earlier version developed by Abel Chouinard (Chouinard 2011).
- The end effector must be able to mill thin (0.063 inch to 0.250 inch) skin panel which is highly flexible.
- The end effector must be able to maintain the same floor bed thickness all-over the pocket in spite of the initial thickness variation of 5 % from the stretching process.
- The end effector must be able to follow the double curvature for milling operation where the minimum radius of curvature is 24 inch and maximum 70 inch.
- The work envelope (work area) of the end effector must be big enough to mill large skin panel of which typical dimension is 2 ft. x 3ft. to 9 ft. x 19 ft.
- The minimum remaining skin panel floor bed thickness can be as small as 0.016 inch with a tolerance limit of +/- 0.002 inch.
- The end effector design should provide higher productivity with respect to material removal rate in machining pockets (dimensions - width (2 inch to 6 inch tolerance +/- 0.060 inch x L (2 inch to 24 inch tolerance +/- 0.060 inch) x depth (0.200 inch)).
- The total weight of the end effector should not exceed the weight tolerance level of the commercial robot manipulator to maintain accuracy.
- The design should consider the work environment condition (dust, debris, chips cutting fluid etc.) while selecting the building components.
- The design should include as much non-magnetic material as possible to reduce interaction with magnets in the grasping mechanism.
- Considering the prototype development is just an academic test procedure rather than an industrial application the cost of the components needs to be optimized.

3.1.6 Organization of the articles

The following four chapters are four articles which result from the research conducted.

The first article in Chapter 4 is entitled “Magnetic attraction forces between permanent magnet groups in magnetic clamp for pocket machining”. This paper answers the research question “What types of magnetic properties need to be investigated for the magnet selection in case of designing a magnetic clamp?” The paper states that axial magnetic force provides the required support for milling operation against the milling thrust force. Since drag force is required to surpass the slave to skin panel friction forces, the paper analyze the lateral magnetic force among the magnets of a pair in a group. This paper describes an analytical force measurement between two permanent magnet groups arranged in triangular array fashion to verify if the forces are sufficient to support against milling forces and frictional forces for a mobile magnetic clamp. This article has been submitted to the CIRP Journal of Manufacturing Science and Technology on 27th April 2015

The second article, presented in Chapter 5 is entitled “Mechanical pocket milling of thin aluminum panel with a grasping and machining end effector”. This work proposes a process for thin skin plate milling with a magnetic grasping end effector. The three main impediments to mechanical milling is skin panel’s thinness causing low stiffness, double curvature and tight pocket floor thickness tolerance. The novel idea of a magnetic grasping end effector theoretically overcomes these problems. An end effector prototype has been assembled and a few tests have been completed inside a CNC machine with satisfactory results establishing a base for future development. The research question is how the remaining panel thickness could be maintained according to the specified level of accuracy while maintaining higher cutting efficiency? To answer this question a dynamic depth of cut strategy which works with continuous feedback of instantaneous thickness based milling system has been proposed. The proposal has been evaluated by developing a prototype end effector and completing laboratory tests. Another research question “It is possible machining a double curvature skin panel with grasping and machining end effector?” has been addressed by the double gimbal mechanism. It is a passive mechanism which adopts the inclination of the panel curvature without any prior guidance. The double gimbal mechanism also helps for higher cutting efficiency. This article has been submitted to the Journal of Cleaner Production on 26th January 2015.

The third article, presented in Chapter 6, is entitled “Determining the minimum clamping force by cutting force simulation in aerospace fuselage pocket machining”. This article mainly answers the research question “How much clamping force must be provided by the grasping and

machining end effector for milling operation?” The paper helps to determine the required minimum clamping force for designing a grasping and machining end effector. In this work, a specific model for torus cutter milling force and a general milling force model have been simulated to predict the cutting forces. In order to get higher cutting efficiency the torus cutter need to adopt different tilt angle relative to the workpiece which changes the thrust force. An equation has been developed to predict the resulting thrust force on the skin panel at different tilting angle. Simulated thrust force results have been validated against dynamometer readings acquired during milling operation. This article has been published in the Journal of Advanced manufacturing Technology on 29 Apr 2015, Digital Object Identifier (DOI) -10.1007/s00170-015-7104-4 <http://link.springer.com/article/10.1007/s00170-015-7104-4>.

The article in Chapter 7 is entitled “Modeling of laterally sliding motion of a magnetic clamp”. This paper mainly targets the research question “How the slave module design could be optimized so that slave can follow the master smoothly without stick slip motion?” This paper proposes a model for the lateral sliding motion of the master to slave module by magnetic attraction forces. The lateral sliding motion of the slave module in response to the master module motion is studied using a transfer function based motion model established considering the lateral magnetic stiffness. The transfer function shows that the slave mass and lateral magnetic stiffness play vital roles in the slave response motion resulting from the imparted master’s motion. Friction coefficient of the pad material with respect to the skin material has been taken into consideration while developing the transfer function. The transfer function shows that slave mass, friction coefficient and lateral magnetic stiffness could be analyzed to ensure a smooth slave motion avoiding stick-slip. This article has been submitted to the Journal of Vibration and Control on 12th April 2015.

CHAPTER 4 ARTICLE 1: MAGNETIC ATTRACTION FORCES BETWEEN PERMANENT MAGNET GROUP ARRAYS IN A MOBILE MAGNETIC CLAMP FOR POCKET MACHINING

A. Mahmud, J.R.R Mayer, L. Baron (2015)

Submitted to CIRP Journal of Manufacturing Science and Technology

Abstract—A mobile magnetic clamp was recently tested for pocket milling on a fuselage panel. The magnetic clamps need to provide sufficient support force against the milling thrust force and sufficient drag force to overcome the frictional force. Triangular arrays of cylindrical permanent magnets are used. Axial magnetic attraction forces between magnet groups are calculated based on recently published formula at various axial heights and lateral displacements. A model is here proposed to estimate lateral magnetic attraction forces as a function of lateral displacement between two cylindrical permanent magnets. Experiments conducted using a dynamometer table to validate the measured axial and lateral magnetic forces strongly support the analytically predicted magnetic forces.

Index Terms — Magnet array, cylindrical permanent magnet, magnetic axial force, Lateral magnetic force, Pocket machining

4.1 Introduction

This paper describes an analytical force model between two permanent magnet groups arranged in a triangular array fashion. The model is then used to assess whether the forces generated are sufficient to counteract both the milling forces and frictional forces affecting the mobile magnetic clamp. The magnetic clamp (Chouinard 2011) main function is to hold a panel while pockets are machined on its surface. At the same time since it must slide over the panel, friction forces are generated. Axial magnetic attraction force between three closely located pairs of cylindrical magnets provides the support force to keep the panel in position. Lateral attraction force between the cylindrical permanent magnet pulls the slave part of the clamp over the panel to keep it close to the master part of the clamp. Axial and lateral magnetic force directions are shown in Figure 4.

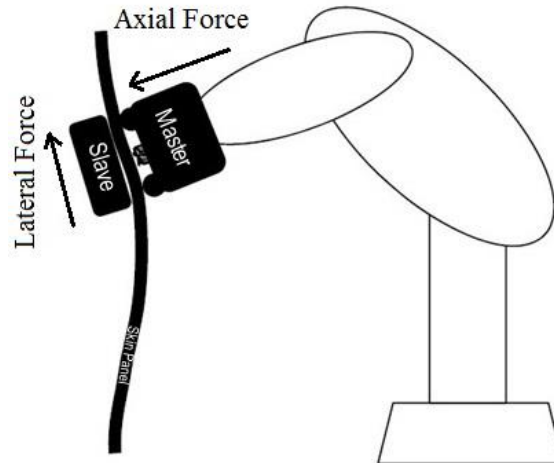


Figure 4: Axial and lateral magnetic force direction in the mobile magnetic clamp

Vučković et al. (Vučković, Ilić et al. 2013) presented a semi-analytical approach for the determination of the magnetic levitation force between two laterally displaced cylindrical permanent magnets. Fictitious magnetization charges and the discretization technique were adopted for cylindrical magnets assuming similar magnetic material and uniform magnetization along their axes of symmetry (opposite direction).

Ravaud et al. (Ravaud, Lemarquand et al. 2010) published an analytical expression to calculate the mutual inductance (axial force) between two axially magnetized cylindrical permanent magnets in air. Due to high computation time and complex valued results a simplified equation was later proposed by Robertson et al. (Robertson, Cazzolato et al. 2011).

Formulas have also been proposed by Agashe and Arnold (Agashe and Arnold 2008) for the attraction forces between two uniformly magnetized cylindrical permanent magnets. Kelvin formula was employed to derive explicit analytical solutions for axial and lateral forces. Long and elaborated equations result for practical application based calculation.

All aforementioned paper considered face to face (aligned with no lateral displacement) interaction of a single pair of permanent cylindrical magnet but Vokoun et al. (Vokoun, Beleggia et al. 2009) used a Bessel function based attraction force equation to elaborate axial force for more than two cylindrical magnets with the special case of two groups magnet set each comprising four magnets. Later Vokoun (Vokoun, Tomassetti et al. 2011) generalized the attraction force equation for two infinite arrays of cylindrical magnet.

In the case of a mobile magnetic clamp the corresponding magnets of each group do not remain coaxial. Due to frictional forces the slave module lags behind the master module introducing a lateral displacement. It is necessary to estimate the axial force between master and slave triangular magnets groups considering this lateral displacement. In this paper Vokoun's Bessel function based equation are used for determining the axial magnetic force between triangular magnetic groups for different lateral and axial displacement. Additionally, a formulation is proposed, and experimentally validated, to explain the lateral magnetic force using Bessel function of the first kind.

4.2 Theoretical framework

The mobile magnetic clamp has three gripping sets forming, with the contact mechanisms, a kinematic contact system to avoid redundancy and contact ambiguity in planar gripping. Three permanent cylindrical magnets are used at each group to support the axial force generated by the milling operation. Each group has three magnets at the vertices of an equilateral triangle. These three groups of permanent magnets are located on a circumference 120 degrees apart completing the array (Figure 5). Similar arrangements are adopted both in the master and slave array. A magnet in the master module array has an opposite magnet in the slave module array, forming a pair. The magnets of each pair are nominally coaxial.

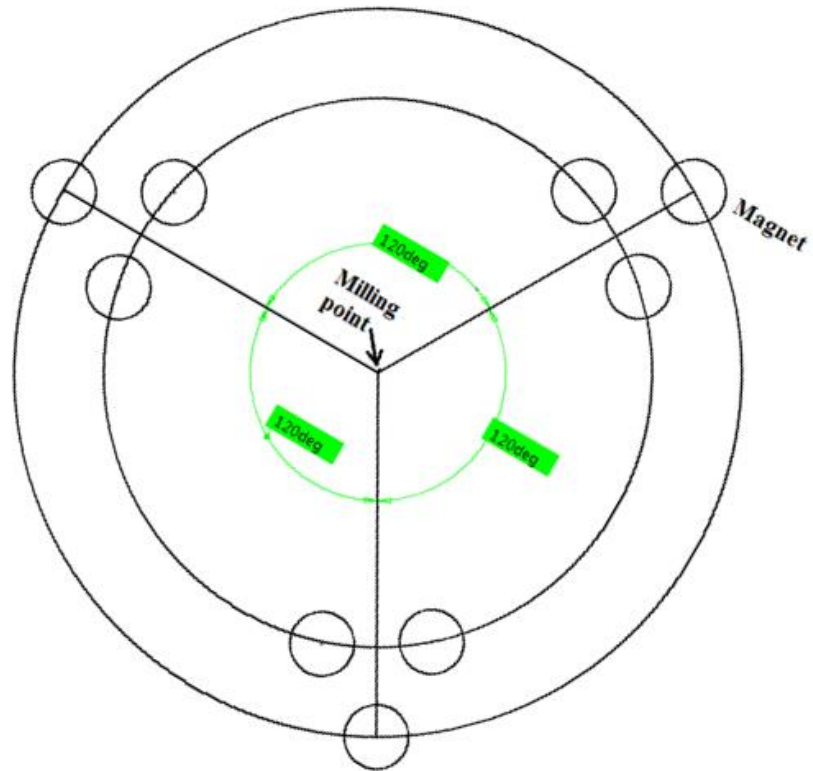


Figure 5: Three magnet group (each group comprised of three individual magnets) located in the master array and slave array

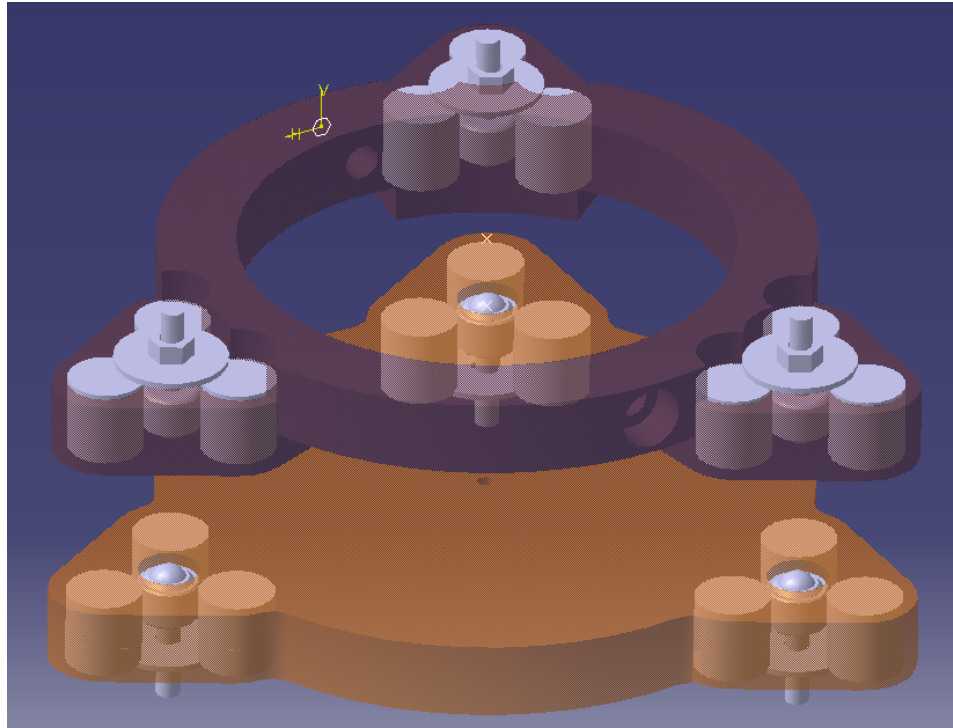


Figure 6: Ball transfer unit are placed at the centroid of the equilateral triangle with magnets at its vertices

The clamping contact point is at the centroid of each group where a ball transfer unit is attached (Figure 6). A magnet attracts the opposite pole and repels the similar pole. Since these permanent magnets are axially magnetized the N-S-N-S orientation is used to get the highest possible attraction force as shown in Figure 7

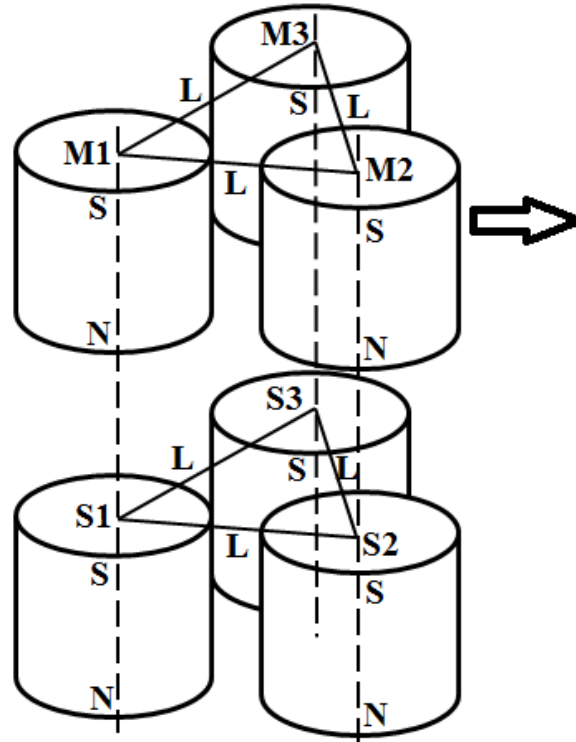


Figure 7: A magnet group (M1, M2 and M3) in the master array coaxial to another magnet group (S1, S2 and S3) in the slave array in static (nominal) condition

Coaxial magnets located in the master and slave array have their own magnetic attraction forces between them (Figure 7). However, the other two magnets of the same group have an influence on that force as they are closely located. This was accounted for with the introduction of a force ratio representing the array contact force enhancement by Vokoun et al (Vokoun and Beleggia 2014). Furthermore, the member magnets of the other groups present in the array have influence on each other. However, as will be shown in the results section, such effects are negligible, due to the significant distance between the groups, and so will be ignored in the calculation. Only the influence of the magnets of the same group will be considered.

Vokoun et al. (Vokoun, Beleggia et al. 2009) expressed the axial attraction force F_z for two coaxial cylindrical permanent magnet of magnetization M , radius R , thickness t , axial gap x and lateral displacement r in equation 4.1 using aspect ratio $\tau_i = t_i/(2R)$, $i = 1, 2$, and $\zeta = (t_1 + t_2)/(2R) + x/R$.

$$F_z = -8 \pi K_d R^2 \int_0^{+\infty} J_0\left(\frac{rq}{R}\right) \frac{J_1^2(q)}{q} \sinh(q\tau_1) \sinh(q\tau_2) e^{-q\zeta} dq \quad (4.1)$$

where the magnetostatic energy constant $K_d = \mu_0 M^2 / 2$.

In case of a group magnet instead of a magnet pair this Bessel function based equation was modified to include multiple magnets influence to the base pair attraction force. Vokoun (Vokoun, Beleggia et al. 2009) modified the equation with indexation 1, 2, ..., n (first group) to n+1, n+2, ..., m (second group).

$$F_z = -8 \pi K_d R^2 \sum_{i=1}^n \sum_{j=n+1}^m \int_0^{+\infty} J_0\left(\frac{r_{ij}q}{R}\right) \frac{J_1^2(q)}{q} \sinh(q\tau_1) \sinh(q\tau_2) e^{-q\zeta} dq \quad (4.2)$$

In the mobile magnetic clamp each magnet group forms an equilateral triangle of side length L . So the magnet axis to axis distance is equal to L . Therefore equation 4.2 can be rewritten in term of lateral displacements L .

$$F_z = -24 \pi K_d R^2 \int_0^{+\infty} \left[1 + 2J_0\left(\frac{Lq}{R}\right)\right] \frac{J_1^2(q)}{q} \sinh(q\tau)^2 e^{-q\zeta} dq \quad (4.3)$$

with $\tau = t/2R$, $t = t_1 = t_2$ and $\zeta = (t + x)/R$.

During milling the master magnet array pulls the slave magnet array by the lateral magnetic force. Friction force hinders the slave magnet array to be coaxial with the master magnet array introducing a lateral displacement. The lateral displacement L between magnets of opposing groups may vary. For example if the master moves a distance r in the Y-axis direction the relative magnet positions are as shown in Figure 8.

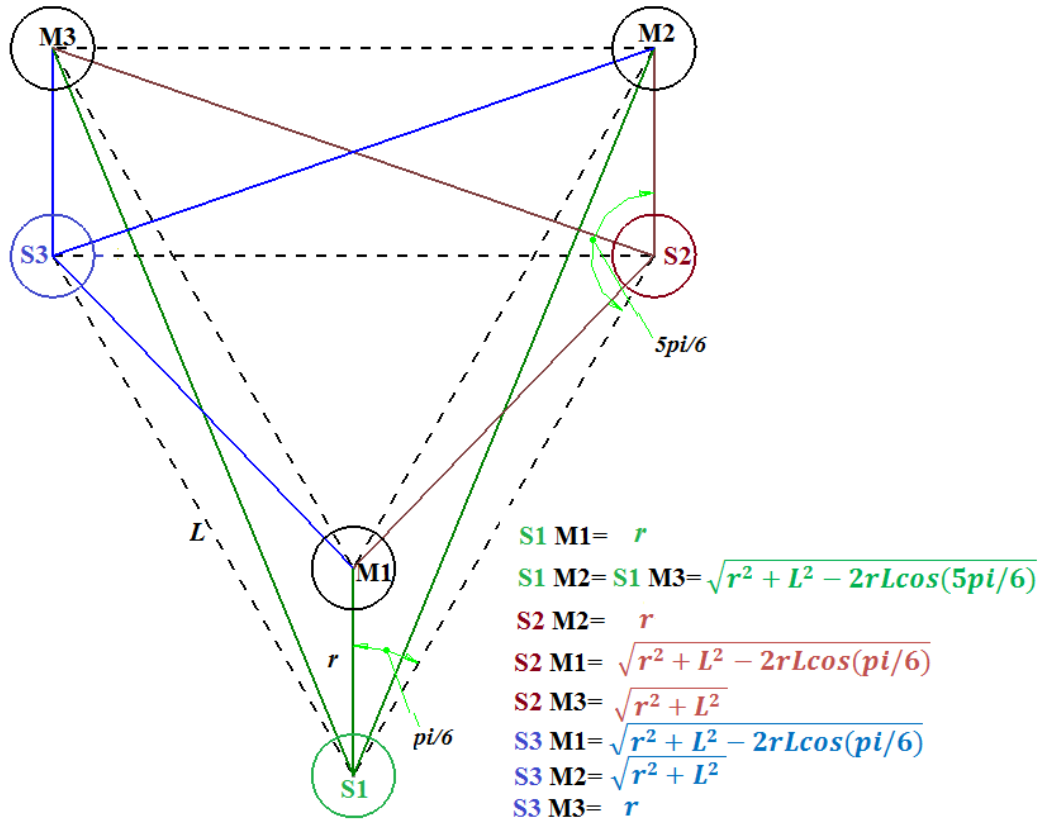


Figure 8: A magnet group (M1, M2 and M3) in the master array moves a distance r in the Y-axis direction with respect to the nominally coaxial magnet group (S1, S2 and S3) in the slave array

Equation 4.3 can be rearranged to calculate the axial magnetic forces between a magnet group in the master array and a magnet group in the slave array.

$$\begin{aligned}
F_z = & -8 \pi K_d R^2 \int_0^{+\infty} \left[J_0 \left(\frac{rq}{R} \right) \right. \\
& + 2J_0 \left(\frac{\sqrt{r^2 + L^2 - 2rL \cos \left(\frac{5\pi i}{6} \right)} q}{R} \right) \left. \right] \frac{J_1^2(q)}{q} \sinh(q\tau)^2 e^{-q\zeta} dq \\
& - 16 \pi K_d R^2 \int_0^{+\infty} \left[J_0 \left(\frac{rq}{R} \right) + J_0 \left(\frac{\sqrt{r^2 + L^2 - 2rL \cos \left(\frac{\pi i}{3} \right)} q}{R} \right) \right. \\
& \left. + J_0 \left(\frac{\sqrt{r^2 + L^2} q}{R} \right) \right] \frac{J_1^2(q)}{q} \sinh(q\tau)^2 e^{-q\zeta} dq
\end{aligned} \tag{4.4}$$

The same distance shift but in the X direction causes a different positional geometry. The mutual internal relative distances among each magnet of a group while moving in the X direction are given in Figure 9. The corresponding magnetic axial forces between the master magnet group and the slave magnet group is expressed by Equation 4.5 .

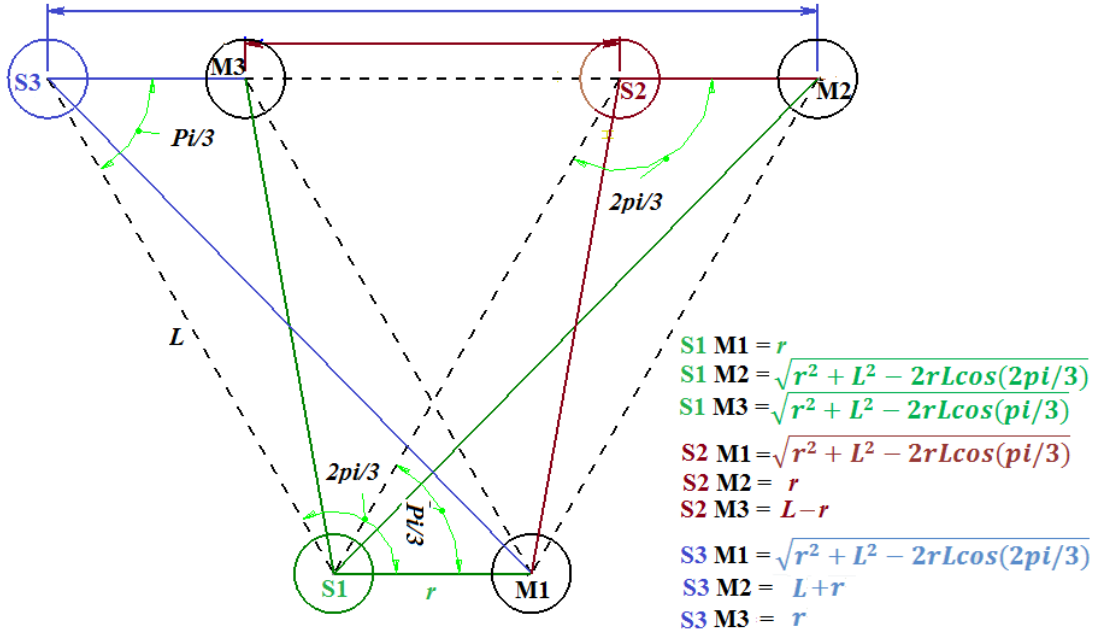


Figure 9: A magnet group (M1, M2 and M3) in master array moves a distance r in the X-axis direction with respect to coaxial magnet group (S1, S2 and S3) in slave array

$$\begin{aligned}
F_z = & -8\pi K_d R^2 \int_0^{+\infty} \left[J_0\left(\frac{rq}{R}\right) + J_0\left(\frac{\sqrt{r^2 + L^2 - 2rL\cos\left(\frac{\pi i}{3}\right)q}}{R}\right) \right. \\
& \left. + J_0\left(\frac{\sqrt{r^2 + L^2 - 2rL\cos\left(\frac{2\pi i}{3}\right)q}}{R}\right) \right] \frac{J_1^2(q)}{q} \sinh(q\tau)^2 e^{-q\zeta} dq \\
& - 8\pi K_d R^2 \int_0^{+\infty} \left[J_0\left(\frac{rq}{R}\right) + J_0\left(\frac{\sqrt{r^2 + L^2 - 2rL\cos\left(\frac{2\pi i}{3}\right)q}}{R}\right) \right. \\
& \left. + J_0\left(\frac{(L+r)q}{R}\right) \right] \frac{J_1^2(q)}{q} \sinh(q\tau)^2 e^{-q\zeta} dq \\
& - 8\pi K_d R^2 \int_0^{+\infty} \left[J_0\left(\frac{rq}{R}\right) + J_0\left(\frac{\sqrt{r^2 + L^2 - 2rL\cos\left(\frac{\pi i}{3}\right)q}}{R}\right) \right. \\
& \left. + J_0\left(\frac{(L-r)q}{R}\right) \right] \frac{J_1^2(q)}{q} \sinh(q\tau)^2 e^{-q\zeta} dq
\end{aligned} \tag{4.5}$$

In the case of a cylindrical permanent magnet the radial (lateral) stiffness is half the axial stiffness (Elies and Lemarquand 1999). The same relation has also been admitted by Yonnet (Yonnet 1981). Following their equation the lateral magnetic force is expressed by Equation 4.6 if only a pure X or Y displacement occurs

$$F_x = F_y = \frac{1}{2} F_z \tag{4.6}$$

Although Equation 4.6 provides a general idea of maximum lateral magnetic force as a ratio to maximum axial magnetic force, it does not specify exactly the amount of lateral force at each single point based on the lateral displacement of a magnet from the other magnet of a pair.

Lateral magnetic attraction force F_x or F_y for two coaxial cylindrical permanent magnet of magnetization M , radius R , thickness t , axial gap x and lateral displacement r could be modeled as Equation 4.7 using aspect ratio $\tau_i = t_i/(2R)$, $i = 1, 2$, and $\zeta = (t_1 + t_2)/(2R) + x/R$.

$$F_x = F_y = -8 \pi K_d R^2 \int_0^{+\infty} J_1\left(\frac{rq}{R}\right) \frac{J_1^2(q)}{q} \sinh(q\tau_1) \sinh(q\tau_2) e^{-q\zeta} dq \quad (4.7)$$

where the magnetostatic energy constant $K_d = \mu_0 M^2 / 2$.

Equation 4.7 establishes the lateral magnetic force between two coaxial magnet of a pair. This relation could be used for explain the interaction forces among the groups of a magnet array. When a magnet group in master magnet array moves in Y axis direction as described in Figure 8, the lateral magnetic force is expressed as equation 4.8.

$$\begin{aligned} F_y = & -8 \pi K_d R^2 \int_0^{+\infty} \left[J_1\left(\frac{rq}{R}\right) \right. \\ & \left. + 2J_1\left(\frac{\sqrt{r^2 + L^2 - 2rL\cos\left(\frac{5\pi i}{6}\right)} q}{R}\right) \right] \frac{J_1^2(q)}{q} \sinh(q\tau)^2 e^{-q\zeta} dq \\ & - 16 \pi K_d R^2 \int_0^{+\infty} \left[J_1\left(\frac{rq}{R}\right) + J_1\left(\frac{\sqrt{r^2 + L^2 - 2rL\cos\left(\frac{\pi i}{3}\right)} q}{R}\right) \right. \\ & \left. + J_1\left(\frac{\sqrt{r^2 + L^2} q}{R}\right) \right] \frac{J_1^2(q)}{q} \sinh(q\tau)^2 e^{-q\zeta} dq \end{aligned} \quad (4.8)$$

Similarly when the magnet group in master magnet array moves in the X-axis direction relative to the other magnet group in slave array as described in Figure 9, the lateral magnetic force between these two groups is expressed as in Equation 4.9.

$$\begin{aligned}
F_x = & -8\pi K_d R^2 \int_0^{+\infty} \left[J_1\left(\frac{rq}{R}\right) + J_1\left(\frac{\sqrt{r^2 + L^2 - 2rL\cos\left(\frac{\pi}{3}\right)}q}{R}\right) \right. \\
& \left. + J_1\left(\frac{\sqrt{r^2 + L^2 - 2rL\cos\left(\frac{2\pi}{3}\right)}q}{R}\right) \right] \frac{J_1^2(q)}{q} \sinh(q\tau)^2 e^{-q\zeta} dq \\
& - 8\pi K_d R^2 \int_0^{+\infty} \left[J_1\left(\frac{rq}{R}\right) + J_1\left(\frac{\sqrt{r^2 + L^2 - 2rL\cos\left(\frac{2\pi}{3}\right)}q}{R}\right) \right. \\
& \left. + J_1\left(\frac{(L+r)q}{R}\right) \right] \frac{J_1^2(q)}{q} \sinh(q\tau)^2 e^{-q\zeta} dq \\
& - 8\pi K_d R^2 \int_0^{+\infty} \left[J_1\left(\frac{rq}{R}\right) + J_1\left(\frac{\sqrt{r^2 + L^2 - 2rL\cos\left(\frac{\pi}{3}\right)}q}{R}\right) \right. \\
& \left. + J_1\left(\frac{(L-r)q}{R}\right) \right] \frac{J_1^2(q)}{q} \sinh(q\tau)^2 e^{-q\zeta} dq
\end{aligned} \tag{4.9}$$

4.3 Experimental setup

The prototype developed based on the magnetic grasping principle works with the master attached to the moving spindle and sliding over the panel while machining with the slave being pulled along magnetically on the other side of the skin panel. Figure shows the regular operation pattern of the prototype. Force measurement by a force dynamometer is difficult in such environment.

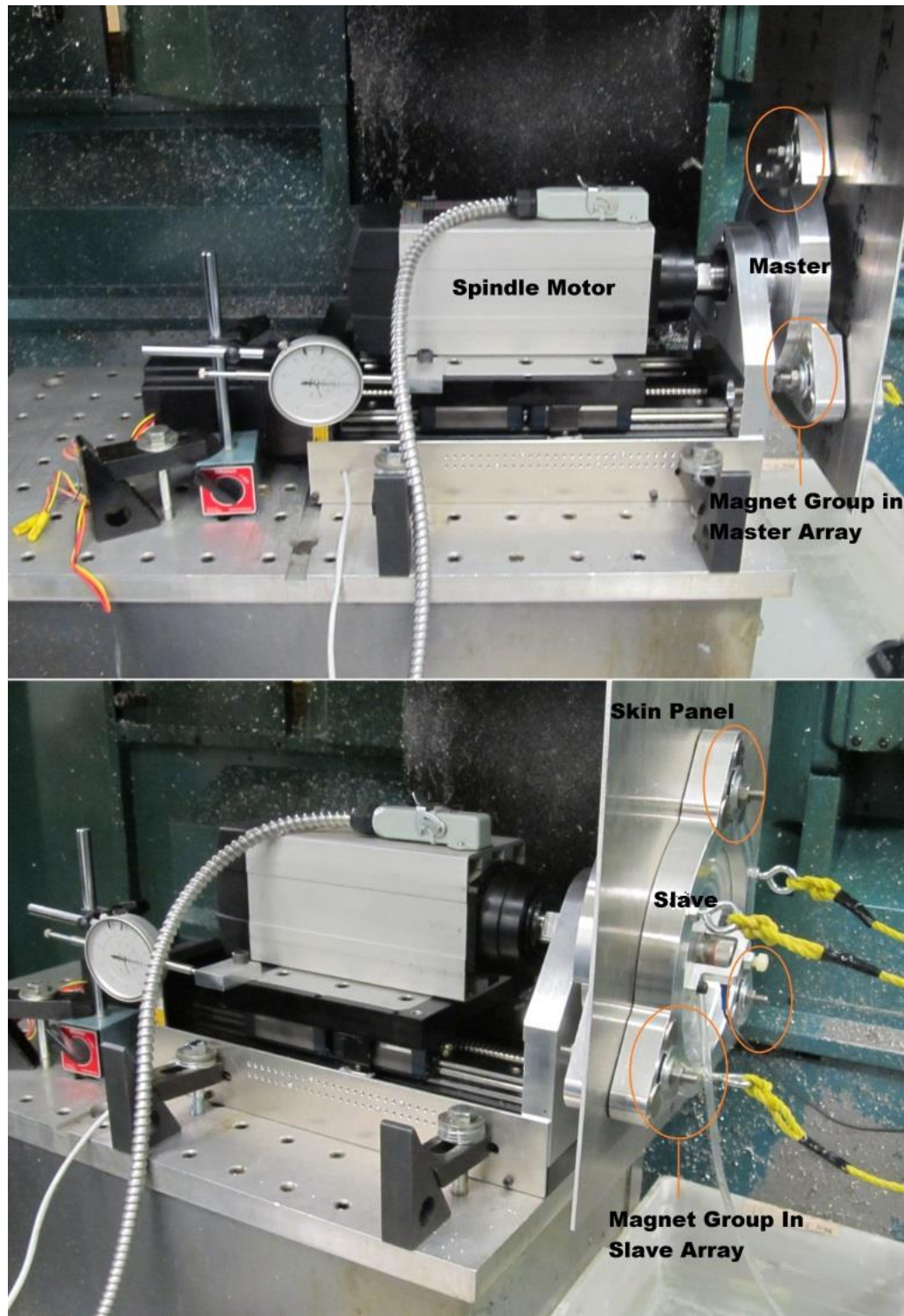


Figure 10: Master module (left of panel) and slave module (right of panel) magnet array in a magnetic grasping milling prototype setup

For the experimental setup both the master and slave modules are removed from the prototype and firmly secured inside a CNC milling machine as shown in Figure .



Figure 11: Master module attached to the CNC spindle and slave module fixed to the top of the dynamometer itself attached to the machine tool table

The master module was attached to the machine spindle with some additional fixture so the spindle does not rotate. The slave module was firmly attached to the Kistler dynamometer. For a relative displacement in the Y-axis or X-axis directions the spindle position is controlled by the CNC as shown in Figure 12 and Figure 13. The same setup also helps to change the axial gap between the master and slave magnet arrays in the Z-axis direction.

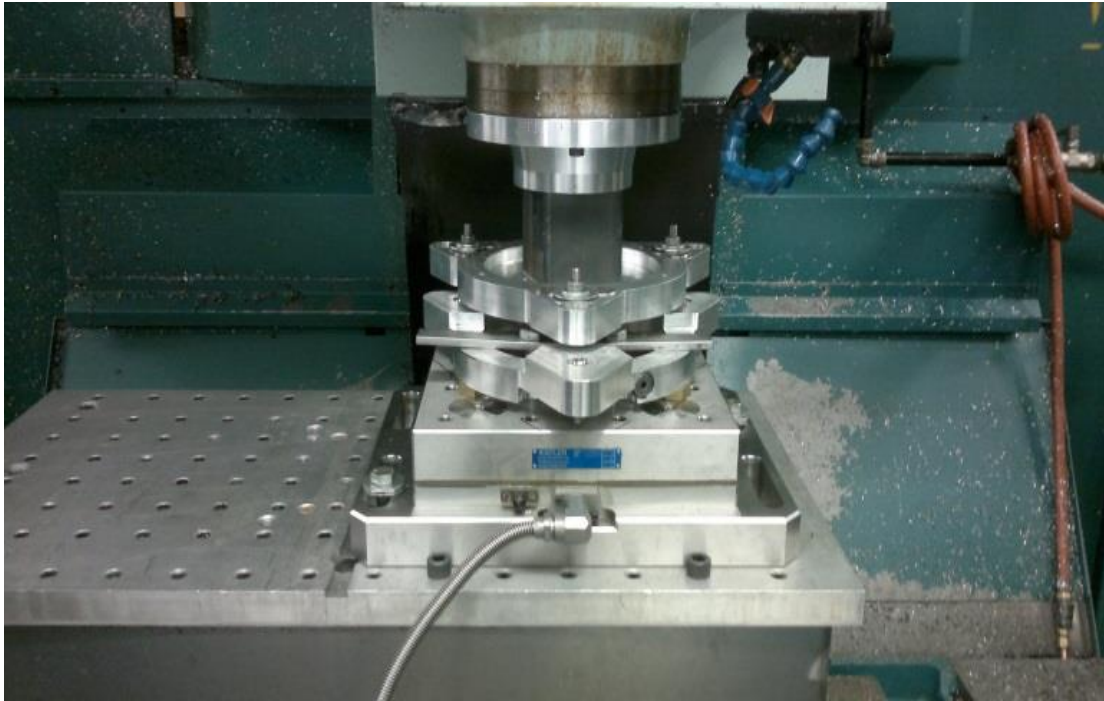


Figure 12: Master magnet array with lateral displacement along Y-axis with respect to the slave magnet array



Figure 13: Master magnet array is lateral displacement along X-axis with respect to the slave magnet array

The dynamometer is connected to a data acquisition system, PXI 1006B chassis including

two 8 channel cards PXI 4472 via the amplifier.

4.4 Results and verification

Using the basic magnet properties 1 inch diameter and 1 inch thick magnet with magnetization value of 1 MA/m) Equation 4.1 was simulated for a range of lateral distances for one single pair of cylindrical permanent magnet. From the simulated results it is observed that beyond 100 mm of lateral distance the axial forces tend to zero.

The first experiment was conducted with one single magnet in each group (removing the other two) for both the master and slave modules. The kept magnets in the master array were nominally coaxial with the magnets in the slave array. This experiment helped to verify Equation 4.1 where only a single magnet pair is considered for force estimation.

Both the axial and lateral forces between magnets of a pair of magnet are plotted in one single graph in Figure 14. It has been found that the maximum lateral forces is almost equal to half the maximum axial forces as predicted in Equation 4.6. For an axial gap of 6.5 mm between magnets of a pair the maximum lateral force is 150 N which is close to the half of axial force of 330 N.

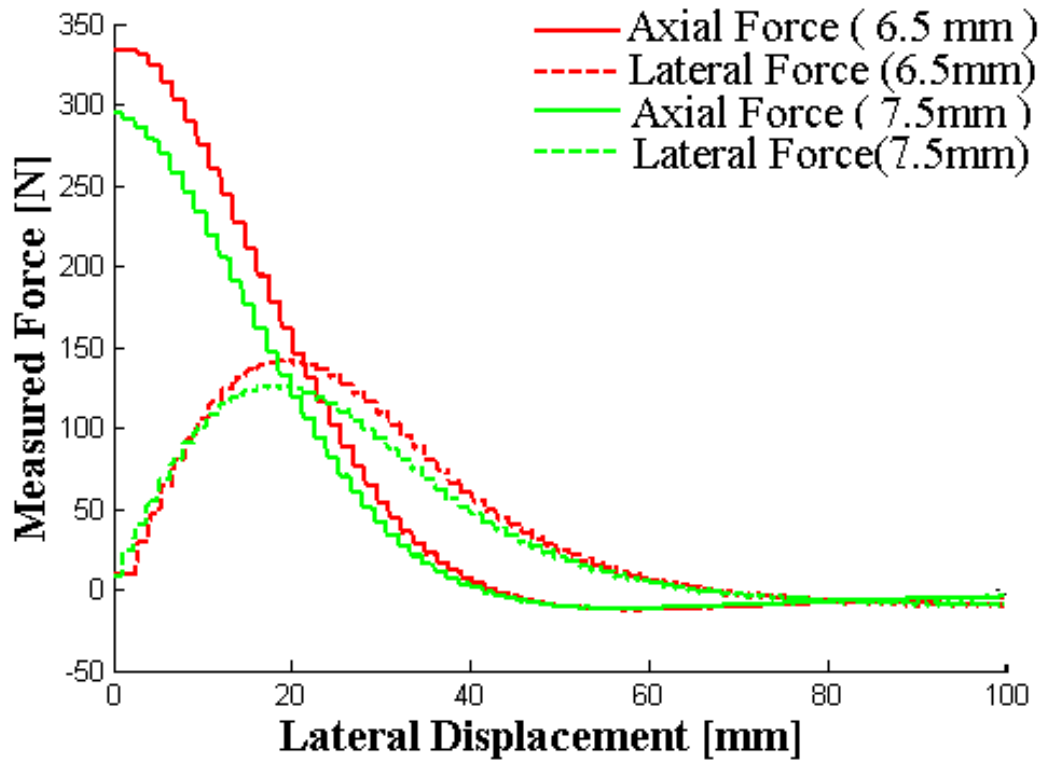


Figure 14: Axial force and lateral force one coaxial magnet pair with axial gaps x of 5.5 and 6.5 mm

Axial forces are calculated by Equation 4.1 for a range of lateral distances which is then compared with the measured ones as shown in Figure 15. Two values of the axial gap x were used. A larger axial gap results in lower axial force. Increasing lateral displacement also results in lower axial force and the tends towards zero at large lateral displacement.

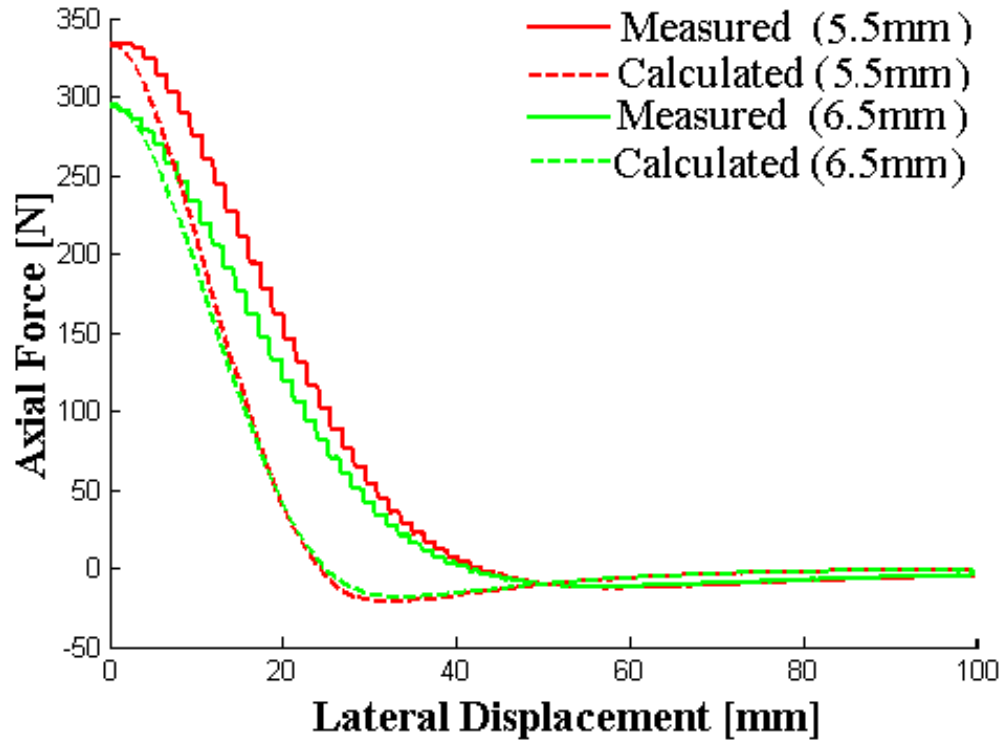


Figure 15: Calculated vs measured axial force for one pair of magnets with axial gaps x of 5.5 and 6.5 mm

The proposed lateral force model as described in Equation 4.7 has been tested against the experimental value obtained with one coaxial magnet pair located in master and slave array. Figure 16 show the comparison between the proposed model based calculated force and experimental measured. It is observed that the calculated force tends to increase and then fall quickly as the lateral displacement increases. Measured force follows a slow decrease compared to the calculation based on the proposed lateral force model.

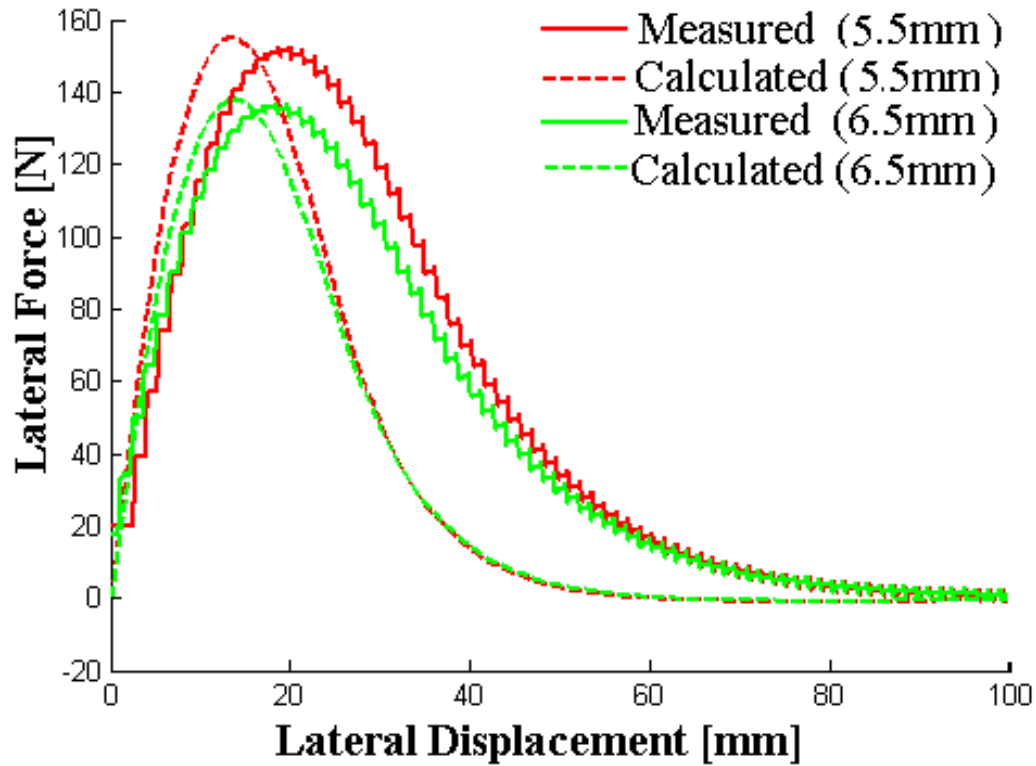


Figure 16: Calculated vs measured lateral force for one pair of magnets with axial gaps x of 5.5 and 6.5 mm

For the following experiment all three magnets were present in each of the magnet group at the vertices of an equilateral triangle of nominal side length $L = 43.37$ mm. For this test, first the master magnet array was moved incrementally along the Y-axis direction. Both the axial and the lateral force have been recorded in the force dynamometer plotted in Figure 17.

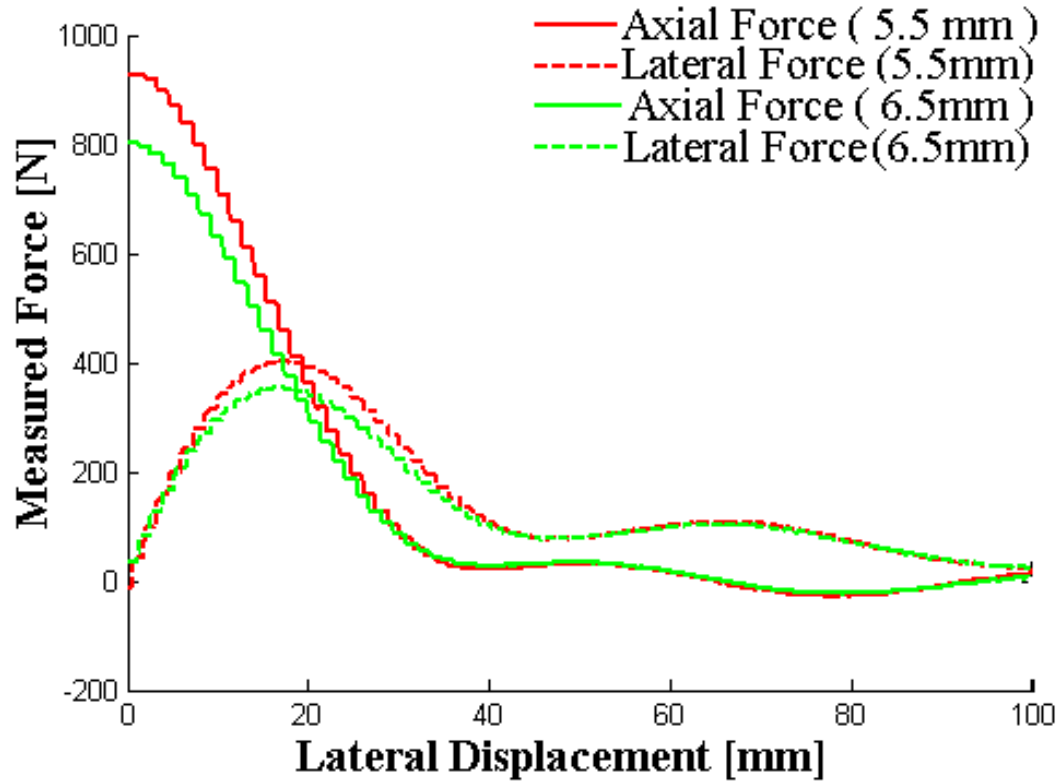


Figure 17: Axial force and lateral force with respect to lateral displacement in Y axis direction between magnet array at 5.5 and 6.5 mm axial gaps, x

Equation 4.4 which considers the relative displacement among the magnets of the same group located in opposite magnet array was used to calculate axial forces based on lateral displacement. Two axial gap x values were used (5.5 and 6.5 mm) to compare the calculated value against the experimental value as shown in Figure 18.

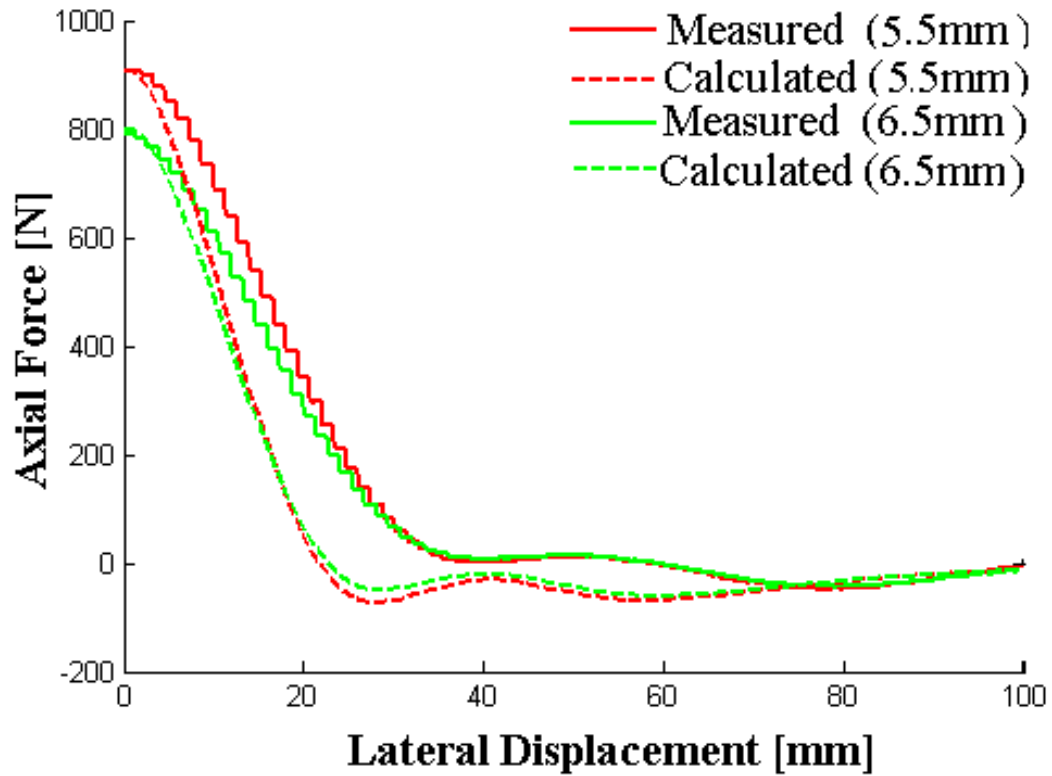


Figure 18: Calculated vs measured axial force with respect to lateral displacement in Y axis direction between magnet array at 5.5 and 6.5 mm axial gaps, x

Similarly, the lateral force has been also calculated based on the proposed Equation 4.8 and plotted with the experimental data in Figure 19. The measured and predicted forces follow similar patterns but there are significant variations in the maximum amount of force at a displacement of 20 mm.

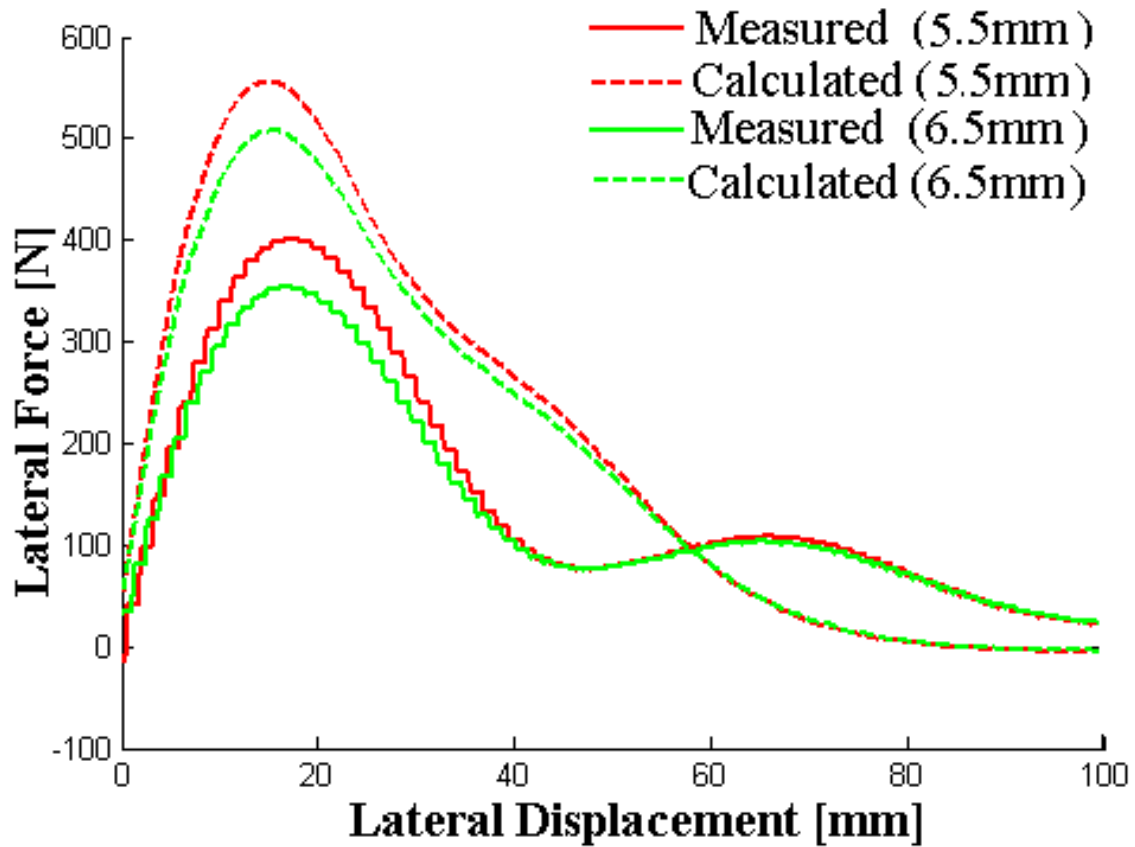


Figure 19: Calculated vs measured lateral force with respect to lateral displacement in Y axis direction between magnet array at 5.5 and 6.5 axial gaps, x

When the master array moves in the X-axis direction the relative positional distance are not the same as for the Y-axis direction. Both axial and lateral forces obtained from experiment for an X-axis lateral displacement are shown Figure 20.

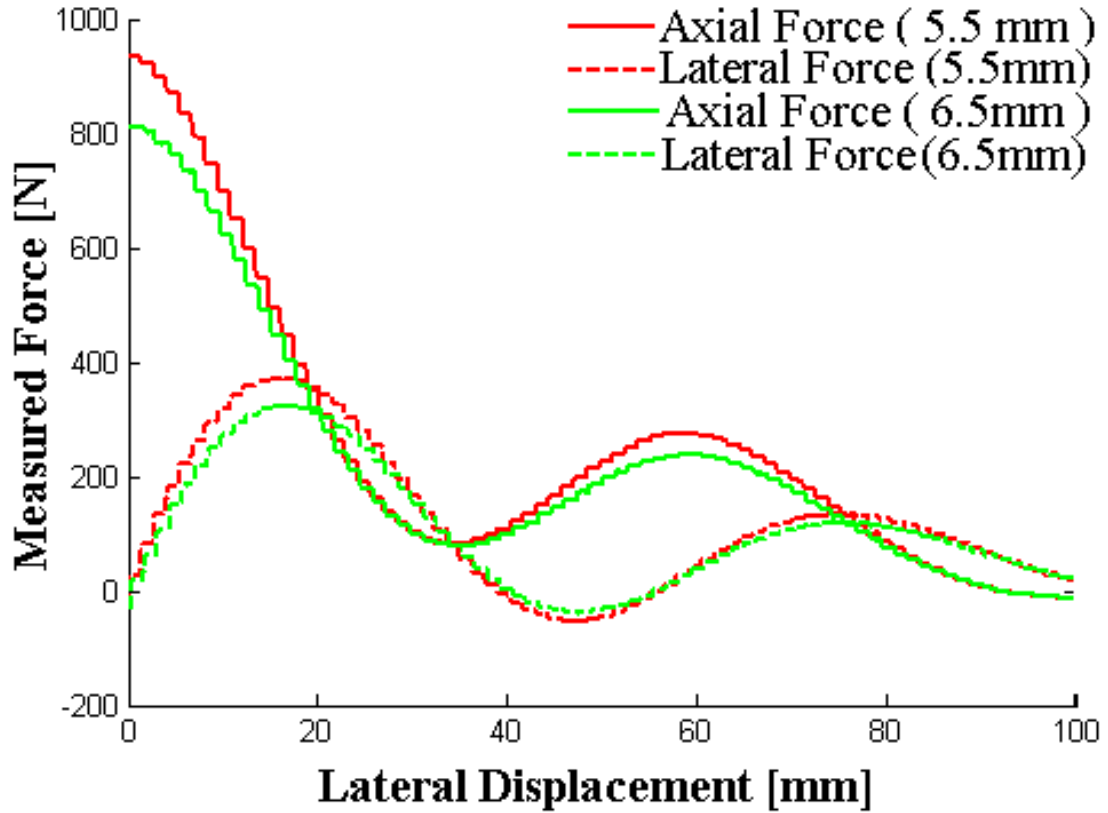


Figure 20: Axial force and lateral force with respect to lateral displacement in X axis direction between magnet array at 5.5 and 6.5 axial gaps, x

Experimental and predicted (using Equation 4.5) axial forces are shown in Figure 21. The Bessel function based axial force calculation follows a faster drop.

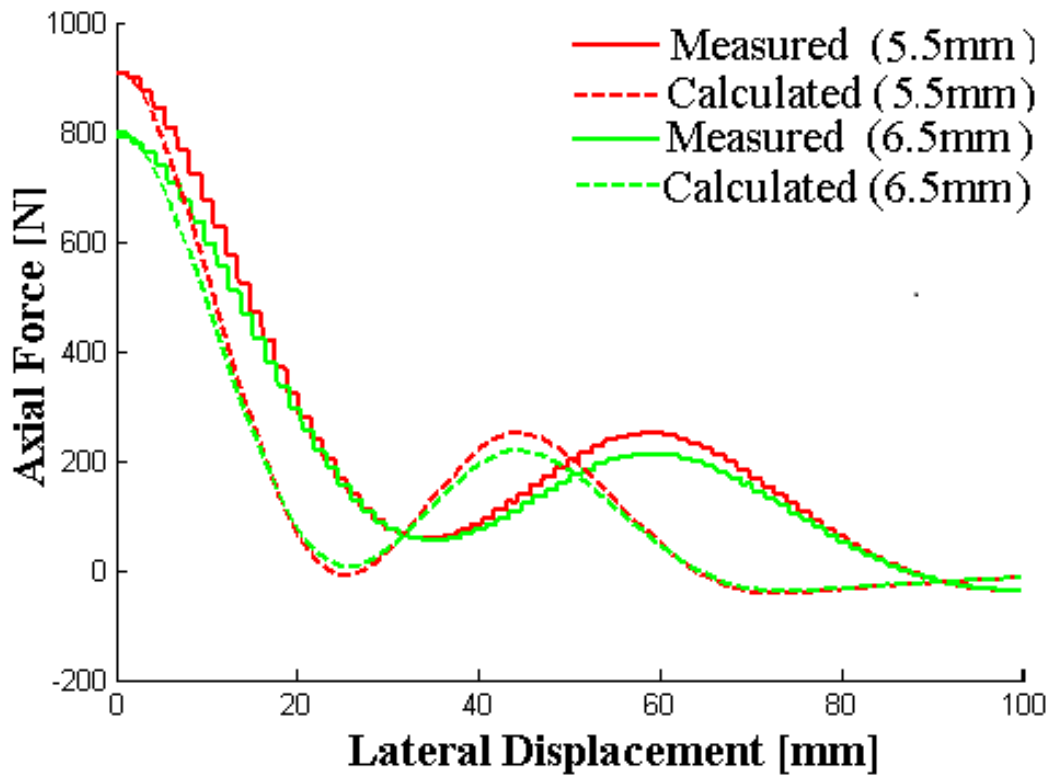


Figure 21: Calculated vs measured axial force with respect to lateral displacement in X-axis direction between magnet array at 5.5 and 6.5 axial gaps x

Lateral forces with respect to X-axis displacement are compared with the calculated force from Equation 4.9 in Figure 22. Like the lateral force estimation in Y-axis direction, the X-axis displacement lateral force also show substantial variation in the maximum amount of forces though the increasing and decreasing pattern are similar.

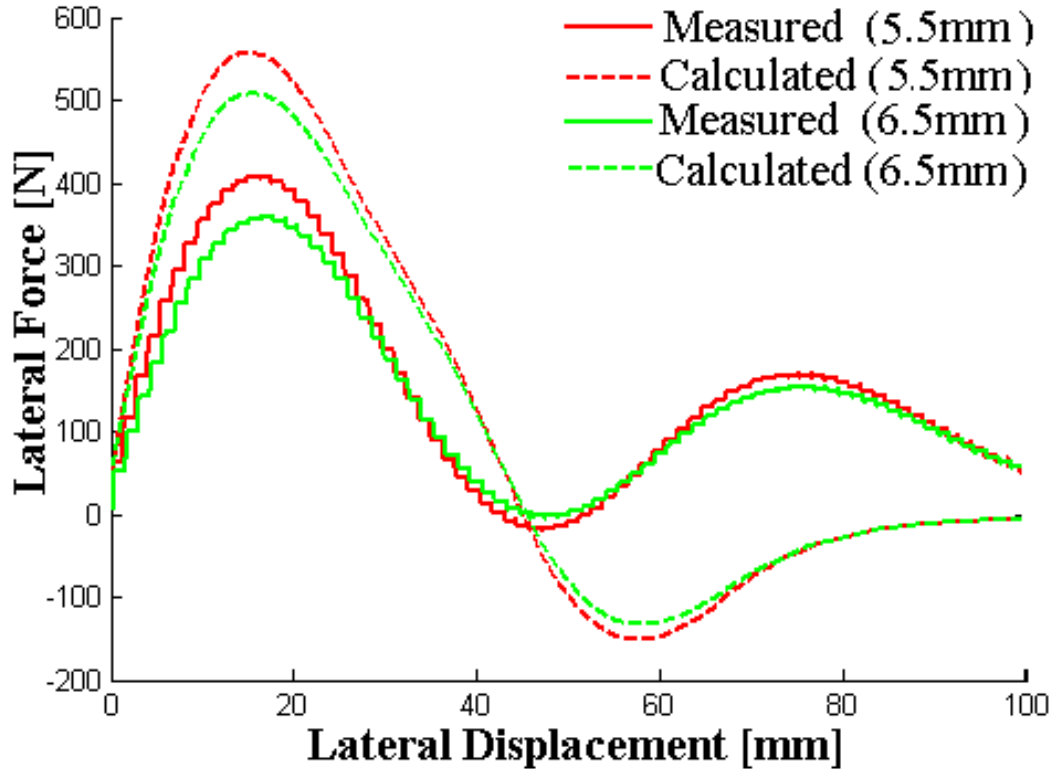


Figure 22: Calculated vs measured lateral force with respect to lateral displacement in X-axis direction between magnet array at 5.5 and 6.5 axial gaps x

The prime interest of the master and slave magnet array construction is to provide sufficient axial force against the milling thrust force to function as a mobile magnetic clamp. In a separate experiment it was determined that the maximum thrust force from milling operation could be 66 N in the case of a torus milling cutter (model- ER D038A075-2-MIO-0.38, 0.5 mm depth of cut and feed per tooth $f_t=0.08$ mm) while milling thin aluminum (AL2024-T3) skin panel. So the magnetic force between the master and slave magnet array of around 800~900 N is quite sufficient to perform the clamping task.

Another concern is the mobility of the slave module which depends on the lateral magnetic force. The frictional force between skin panel and slave is determined by the friction coefficient of the ball transfer unit attached to the slave unit. Ball transfer unit (model *OmniTrack* 9101SS, friction coefficient, μ_c of 0.005) was used for this specific test. An axial load of 800 N should cause a frictional force of 4 N ($\mu_c * axial\ load$) which will be supported by lateral force between master and slave magnet array causing a predicted maximum lateral displacement of 0.35 mm based on Figure 22. This in turn causes negligible axial force change

Overall, the measured axial forces followed the prediction calculated by Bessel function of first kind of order 0, the measured and predicted curve are almost collinear when the lateral displacement is less than the magnet radius. Lateral forces which have been predicted based on the Bessel function of first kind of order 1 also showed harmony with the measured force when the lateral displacement remains within magnet radius. In case of a single pair of magnet the estimated forces were more adjoining to the measured forces. For a complete set (all three groups present in the master and slave array) the maximum amount of axial magnetic forces matches both the calculation and measured value which was differing in case of lateral forces. Both the axial and lateral forces were diminished to zero at higher lateral displacement both in theoretical calculation and experiments results.

4.5 Conclusion

Sufficient force must be provided by a mobile magnetic clamp to hold the skin panel during a pocket milling operation. The axial attraction force between the master magnet array and the slave magnet array is the prime source of support against the milling thrust force. The lateral attraction force between master and slave array ensures smooth following of the slave magnet array while the master magnet array moves with the milling spindle.

In this paper a Bessel function based magnet to magnet axial attraction force has been extended and exploited to estimate magnetic force between two different magnet arrays (master and slave) considering their relative position. Each array has three groups and each group includes three identical cylindrical permanent magnets. In the milling application requirement the master magnet array advances with a certain velocity depending on the required machining feedrate and as a result the slave magnet array lags behind by a few millimeters due to frictional forces. The Bessel function based estimated axial forces has been validated by a dynamometer to ensure that the array provides enough forces for clamping and sliding action of the mobile magnetic clamp.

The proposed lateral force model has been validated for the case of a single pair of cylindrical permanent magnet located in master and slave array. However in case of magnet group in master and slave array the results were not that much adjoining. It was also observed that both for axial and lateral forces, the measured forces have faster drop compared to the Bessel function based calculated force prediction Future investigation of other mathematical functions which can

represent axial and lateral forces with more accurate slope and trying different geometric positional criteria varying the array and group size could be helpful.

REFERENCES

- Agashe, J. S. and D. P. Arnold (2008). "A study of scaling and geometry effects on the forces between cuboidal and cylindrical magnets using analytical force solutions." Journal of Physics D: Applied Physics **41**(10): 105001.
- Chouinard, A. (2011). Remplacement de l'usinage chimique des tooles aeronautiques minces en aluminium par de l'usinage mecanique. Departement de genie mecanique, Ecole Polytechnique de Montreal. **M Sc**.
- Elies, P. and G. Lemarquand (1999). "Analytical study of radial stability of permanent-magnet synchronous couplings." Magnetics, IEEE Transactions on **35**(4): 2133-2136.
- Ravaud, R., G. Lemarquand, et al. (2010). "Cylindrical magnets and coils: Fields, forces, and inductances." Magnetics, IEEE Transactions on **46**(9): 3585-3590.
- Robertson, W., B. Cazzolato, et al. (2011). "A simplified force equation for coaxial cylindrical magnets and thin coils." Magnetics, IEEE Transactions on **47**(8): 2045-2049.
- Vokoun, D. and M. Beleggia (2014). "Forces between arrays of permanent magnets of basic geometric shapes." Journal of magnetism and Magnetic Materials **350**: 174-178.
- Vokoun, D., M. Beleggia, et al. (2009). "Magnetostatic interactions and forces between cylindrical permanent magnets." Journal of magnetism and Magnetic Materials **321**(22): 3758-3763.
- Vokoun, D., G. Tomassetti, et al. (2011). "Magnetic forces between arrays of cylindrical permanent magnets." Journal of magnetism and Magnetic Materials **323**(1): 55-60.
- Vučković, A. N., S. S. Ilić, et al. (2013). "Interaction Magnetic Force Calculation of Permanent Magnets Using Magnetization Charges and Discretization Technique." Electromagnetics **33**(6): 421-436.

Yonnet, J.-P. (1981). "Permanent magnet bearings and couplings." Magnetics, IEEE Transactions on **17**(1): 1169-1173.

CHAPTER 5 ARTICLE 2: MECHANICAL POCKET MILLING OF THIN ALUMINIUM PANEL WITH A GRASPING AND MACHINING END EFFECTOR

A. Mahmud, J.R.R Mayer, L. Baron (2015)

Submitted to Journal of Cleaner Production

Abstract—Thin and large aircraft skin panels are chemically milled to create pockets for weight reduction purpose. More environment friendly alternatives to chemical milling are sought. The three main impediments to mechanical milling is skin panel's thinness associated low stiffness, double curvature and tight final thickness tolerance. In this paper a novel idea of a magnetic grasping and machining end effector is presented to overcome these problems. An end effector prototype has been assembled and a few tests have been completed inside a CNC machine with satisfactory results establishing a basis for future development.

Index Terms— robotic milling, grasping end effector, thickness sensor, pockets, magnetic clamp, thin panel.

5.1 Introduction

This paper proposes a process for thin skin plate milling with a magnetic grasping and machining end effector. Aircraft weight reduction is an important issue for aerospace products. So, the skin panels need to be as thin as possible. Currently, the thinning tasks are accomplished by creating pockets in the skin panel by chemical machining.

Chemical machining process results in chemical pollutants. Most of the chemicals such as cleaning solutions, etchants, strippers etc. are hazardous liquids. In particular, etchants are dangerous for workers (Cakir, Yardimeden et al. 2007). So, replacing this industrial chemical milling process with a lower emission and more environment friendly process is sought. Mechanical milling is considered because this process results in recyclable metal chips and eliminates the requirement for costly etchant disposal and metal recovery from waste etchants.

One of the characteristic of aircraft panels is double curvature. Although five axis CNC milling or five axes robotic milling can easily machine a double curvature plane, here the scenario is complicated due to thinness. Low stiffness of the thin panel creates deformation during the cutting operation. Also, the previous stretching causes variation of the initial thickness. This combined with the fact that chemical machining process has a constant material removal rate (MRR) results in irregular pocket floor thickness. Mechanical milling is also affected by the

initial thickness variation. A single depth of cut cannot assure a fixed remaining thickness of the panel. So, maintaining high precision in the pocket floor thickness remains a challenge.

5.2 Literature review

In the aerospace and shipping industries, large parts are difficult to handle and fasten during the machining process. A machine was patented to support and machine these type of parts by Martinez (Martinez 1992). The bridge type machine moves along a track. The workpiece support includes multiple modules which transversely align and move independently along the tracks. All of the modules are equipped with multiple columns which can move vertically to fix the workpieces at their upper end. Computer control ensures the necessary movement in all three perpendicular directions to allow the automatic positioning of the fixing members (valve like vacuum suction cup for grasping the parts). Fixing members (number 3 shown in figure 1) are manipulated to place them at the required positions for supporting and gripping the workpiece.

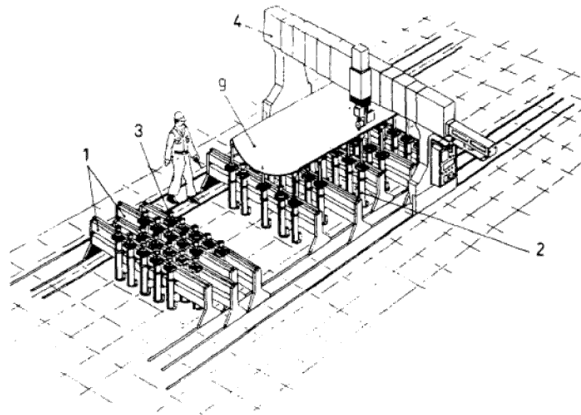


Figure 23: First machine for machining large and complicated shape panel (Martinez 1992)

The machine can adapt to a variety of panel shapes without any specific template requirement and a multi-axis machining head allows machining double curvature panels. A large number of motion controlling motors for frame, modules and even for each column which needs to be independently controlled makes the system complicated to operate. Due to this vertical machining process chip evacuation is also a concern. According to Hamann (Hamann 2007) this

type of suction cups bed introduces internal fastening stress when machining operations for recesses require a space between supports of less than 150 mm.

Hamann patented one specialized process and device for machining large thin panels (Hamann 2007). The machine (figure 2) ensures isostatic positioning to one of the surfaces of a panel avoiding hyperstatism. Two registration holes located on the panel periphery at two opposite side and three reference contact points on the panel secures the isostatic positioning. At least two positioning stops, multiple mobile & prehensile suction cup and suction cup locking system hold the complex shape panel without introducing fastening stresses. In addition to this positioning system there is a means for measuring the actual shape of the surface of the panel. Each of the suction cups has sensors which measure the distance of panel surface from base. Sensors signals are interpolated to calculate the shape of the panel surface. A milling trajectory is calculated considering the interpolated surface. A multi-axis machining head follows the trajectory keeping perpendicular to the machining window (one or more machining zones of predetermined dimensions on the panel in the sections that are to be machined).

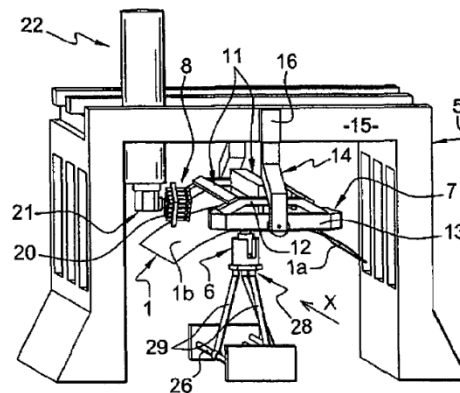


Figure 24: Hamann (2007) device for machining aircraft panel (Hamann 2007)

The process calculates the machining trajectory referencing to the external surface (opposite side of machining surface). The stretching or drawing processing does not generate one uniform thickness on the whole surface of the panel. A new referencing is required to ensure an “automatic” correction for the possible local variation in parallelism existing between the opposite surfaces of the panel. Hamann mentions a precision accuracy of less than 0.2 mm.

The latest solutions developed for thin aircraft panel machining is known as the Mirror Milling Systems (MMS). Two NC machines are used, one on each side of the panel. The first one performs the pocket machining while the other provide support on the opposite side.

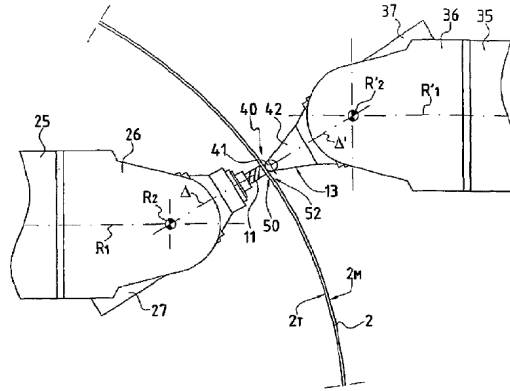


Figure 25: Mirror milling systems for machining of panels. (Panczuk and Foissac 2010)

In Panczuk-Foissac solution (Panczuk and Foissac 2010), the machining tool on the machining face and the holding element (item number 40 in Figure 25) on the holding face are displaced on the opposite sides of the panel in a coordinated manner. The panel is oriented more or less vertical allowing gravitational chip removal. Scanning is performed by an optical sensor mounted on the machining head to determine the actual shape and form of the panel. This allows the machine to work with a wide range of panel forms where the real and nominal forms are different.

All these solutions require complex multi axis CNC systems on both sides and the synchronization of the respective motion.

This paper describes an industrial robotic milling (Bres, Monsarrat et al. 2010) to accomplish the purpose of mechanical milling of aluminum or Al-Li skin panel. A clamping technique reduces the thin skin deformation and makes it more resistant to cutting force. Sensory feedback (Chapleau, Martin et al. 2006) of the remaining thickness is used. The robot will move over the skin surface according the pre-specified pocket dimension (in-plane motion) and the self-feed spindle motion of the milling cutter provides depth of cut control for making the pocket in the skin panel.(out-of-plane motion).

5.3 Concept development

The proposed system operates almost entirely from one side, the machined side, of the skin panel. The feedback for the in-plane tool motion operates entirely on the basis of the pocket floor thickness.

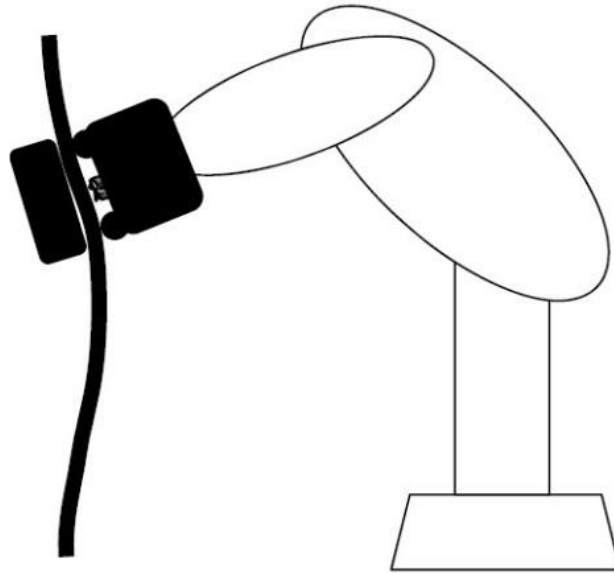


Figure 26: Conceptual design of the grasping and machining end effector.

The machining end effector will be moved by an industrial robot (Figure 26). The magnetic grasping and machining system holds the thin skin panel relative to the robot while allowing two axis tilting. The spindle is attached to the robot via a prismatic axis (an actuated linear motion). Aluminum being a nonmagnetic material the grasping system is constructed with two different magnet groups one on each sides of the panel.

A double gimbal passive mechanism allows the milling spindle to tilt relative to the skin panel leading to higher cutting efficiency. It consists of two rings which can rotate about two orthogonal axes. One ring surrounds the milling cutter to allow the rotation about an axis. The second ring connects to the first ring allowing a rotation about an axis perpendicular to the first ring axis. The second ring constitutes the base plate for the magnets. It follows the double curvature of the skin panel.

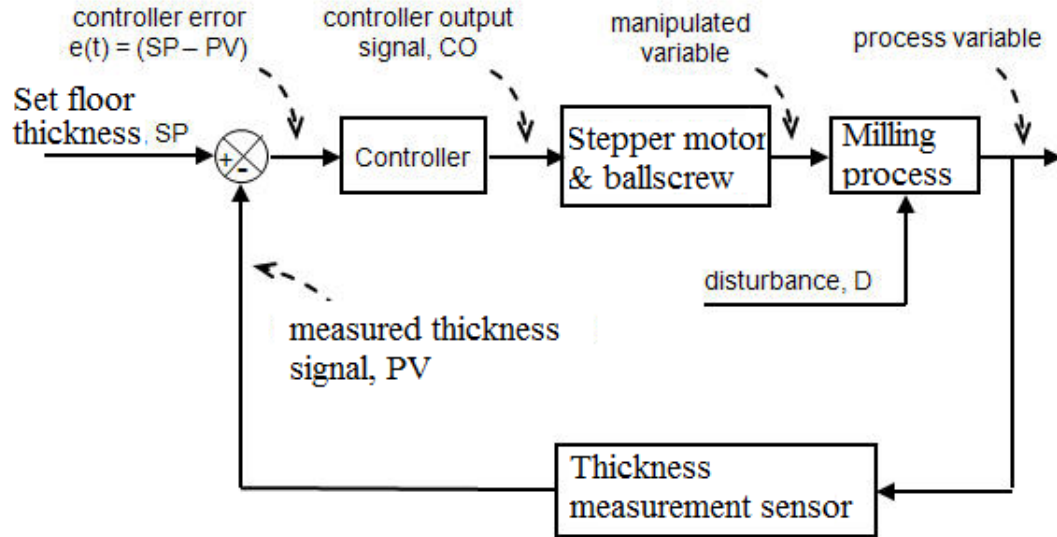


Figure 27: Feedback control loop.

A feedback control loop with an ultrasonic thickness sensor measures the floor thickness of the pocket. Due to the prior step in the manufacturing cycle (stretching) skins have a significant thickness variation. Sensor feedback continually updates the remaining thickness immediately after milling has been accomplished. Based on the remaining thickness the depth of cut is dynamically adjusted by the prismatic axis holding the spindle.

5.4 Mechanical design

The design includes a stepper motor driving a ball screw which moves the spindle housing itself supported by two linear guides on the basis of the real time thickness signal.

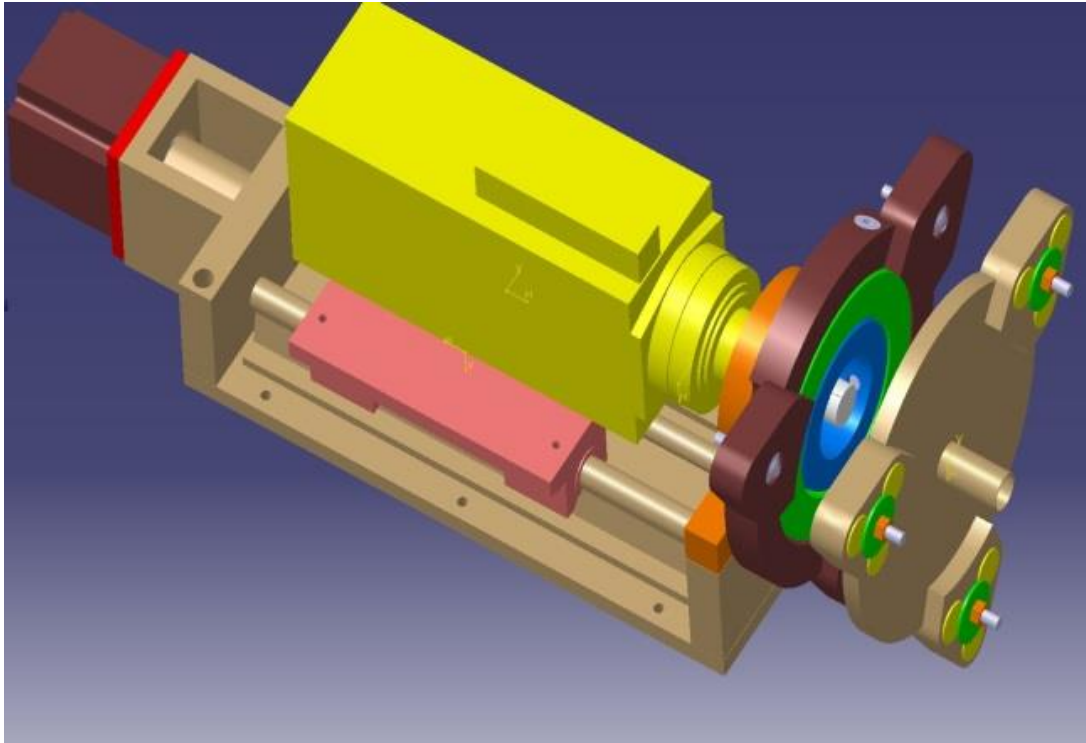


Figure 28: CATIA V5 model for the end effector

The design must be compact in order to keep the three magnetic supports as close to each other as possible to reduce the size of the panel within the three contact pairs to increase its stiffness.

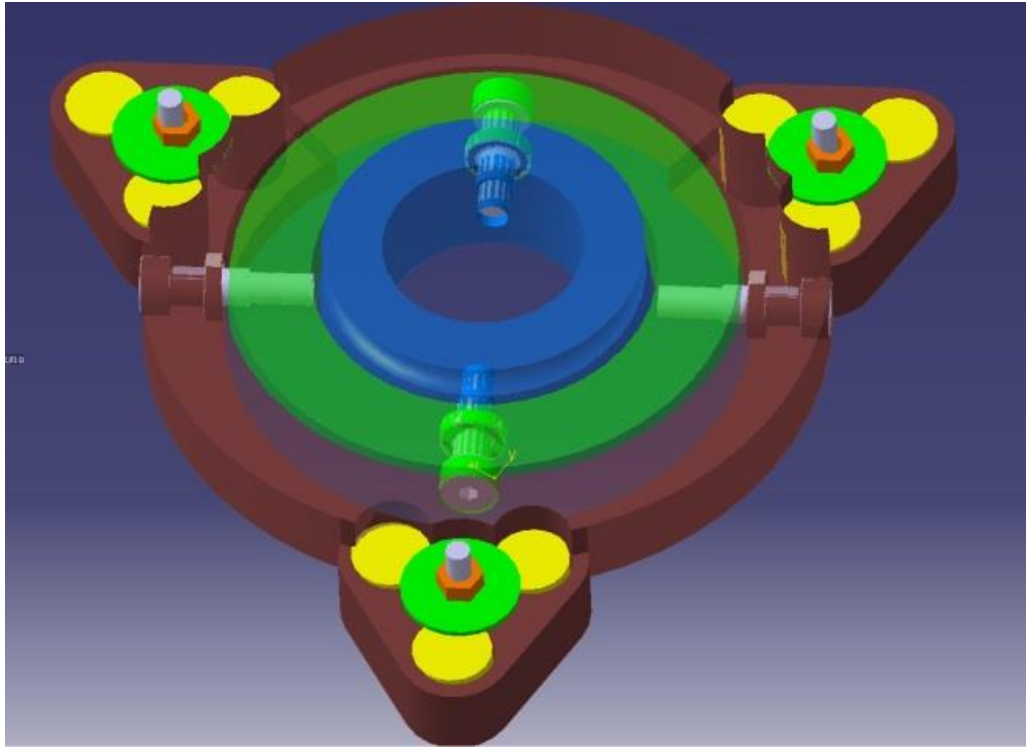


Figure 29: Double gimbal mechanism internal setup

5.5 Prototype development

Three point clamping system

For machining purposes the panel must be held in the out-of-panel direction by the end-effector. The in-plane stability is provided by external fixturing. The use of a triangular 3 point support fulfills this requirement. The added advantage of a three point support is that it can in principle accommodate changes in the surface structure.

The support mechanisms will be a circular plate that will follow the milling cutter and continuously provide sufficient force so that the thin panel does not deflect or deform. This mechanism will act as a slave mechanism. Since the slave mechanism will use magnetic force to counteract the machining force, it's important to maintain the minimum gap between the slave and the panel surface. A support plate of 10-15 inch diameter will ensure maximum contact between slave and surface.

Magnet selection and orientation

Neodymium-Iron-Boron Magnet is prioritized among the alternatives of Alnico, Ceramic, Rare-Earth, Iron-Chromium-Cobalt due to higher strength. Table 1 compares the force density among commercial magnets.

Table 1: Magnetic performance comparison for common permanent magnet(Wikipedia 2014)

Magnet	\underline{B}_r (T)	\underline{T}_C (°C)
Nd ₂ Fe ₁₄ B (sintered)	1.0–1.4	310–400
Nd ₂ Fe ₁₄ B (bonded)	0.6–0.7	310–400
SmCo ₅ (sintered)	0.8–1.1	720
Sm(Co, Fe, Cu, Zr) ₇ (sintered)	0.9–1.15	800
Alnico (sintered)	0.6–1.4	700–860
Sr-ferrite (sintered)	0.2–0.4	450

While selecting the magnet two issues are important. Remanence (B_r), which measures the strength of the magnetic field and Curie temperature (T_C), the temperature at which the material loses its magnetism. According to the basic law of magnetism, opposite poles attract each other and like poles repel. With the opposite pole orientation of N-S-N-S each pair of magnet attract each other. So two opposite pole magnet will be placed both side of the sheet metal to ensure the attraction force between master and slave.

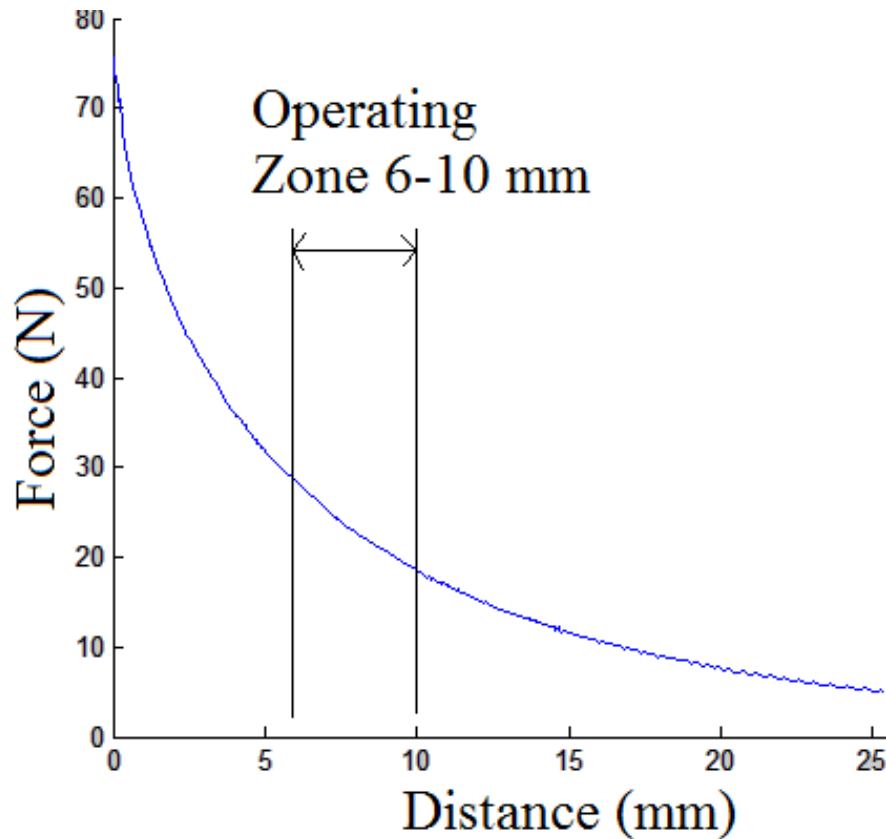


Figure 30: Typical magnet to magnet pull (K&J magnetics 2014)

According to the manufacturer specification at 10 mm distance axial magnetic force between to magnet is around 18 N. Three sets of magnet trio should produce 162 N attraction forces which is quite sufficient to resist the milling thrust force of 75-80 N (Chouinard 2011) with a factor of safety of 2.

Ball transfer unit selection

In-plane motion is subjected to friction force. Both the master and slave modules need to slide over the skin panel avoiding stick-slip motion. Ball transfer unit can roll over the skin panel with minimal friction. Instead of any pad material like Polyoxymethylene, steel ball on the head of ball transfer unit have negligible friction. Ball transfer unit also overcome the problem of overcoming a take up move from pocket area to uncut area.

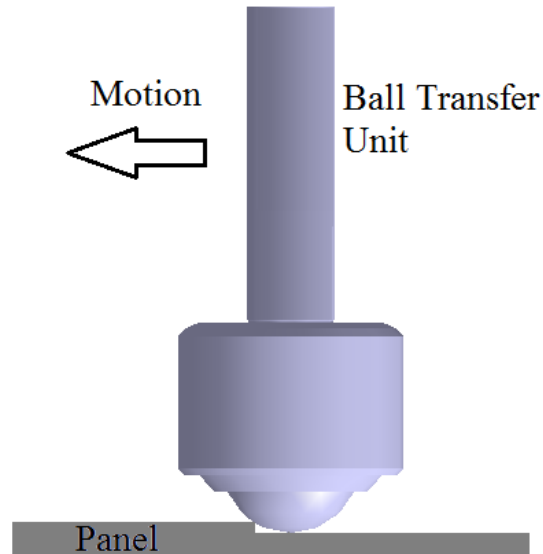


Figure 31: Ball transfer unit can take up form pocket area to uncut area over the skin panel.

Sensor selection criteria

The tolerance of remaining thickness of the panel is ± 0.002 inch (± 0.050 mm). Chips and cutting fluid along with dust on the skin surface make it difficult to measure the actual panel thickness by accessing both sides. Since the opposite side remains clean it is ideal for a thickness measurement. Therefore, one side (opposite side of the skin panel to be machined) thickness measurement is designed. Based on a market survey for one sided thickness measuring sensor, two options are there – eddy current sensor and ultrasonic sensor. As eddy current sensor (± 0.01 inch) was not able to provide the desired accuracy level, ultrasonic sensor got the approval decision. Usual accuracy for an ultrasonic sensor is ± 0.001 inch.



Figure 32: Bubbler type transducer ensures liquid in place by continuous supply (Olympus 2014)

This accuracy meets the requirement. Coupling liquids are necessary to transmit the ultrasonic waves from transmitter face to material face. The slave (support plate) provides support for a liquid delivery system. A bubbler style transducer (Figure 32) holder keeps in touch with the surface through a passive thrust generated by a spring/screw-nut assembly. A pump supplies the couplant liquid to the bubbler transducer.

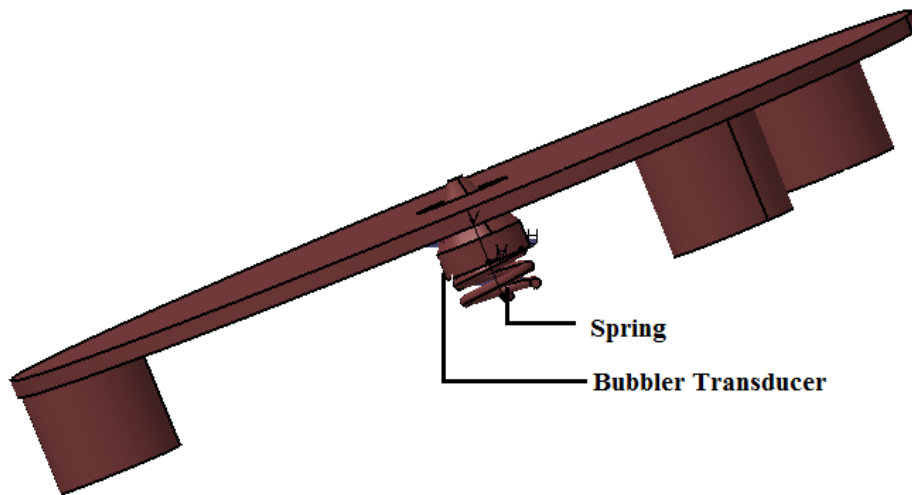


Figure 33: Spring supported bubbler transducer assembly pushes against the panel surface.

Servo motor selection

To advance the spindle motor the linear drive has to counteract the machining thrust force along the Z-axis. To apply the thrust force the servo motor must generate the following torque

$$T = \frac{F_a l}{2\pi\eta}$$

where F_a is the ball screw linear thrust force, l is the screw lead and η is the efficiency.

Due to a low depth of cut the thrust force is small. In the pilot project done by Abel Chouinard the Z-axis force was at most 75-80N (Chouinard 2011). In case of 0.2 inch lead and 90% efficient ball screw the calculated torque requirement is 0.07 Nm. Ball screws are more efficient, requiring less torque and experience lower friction compared to lead screw. Furthermore ball screws usually offer higher accuracy than lead screws which is the prime reason for selecting a ball screw for the design.

A stepper motor which supports 8 Nm is adopted. While making the selection between servo motor and stepper motor, stepper motor seems to be more appropriate based on the requirement. Servo system usually recommended for high-speed, high-volume, high-reliability applications. And stepper motor for low to moderate operation ensuring cost effectiveness. Servo requires a constant positional feedback making the system complicated. The design is based on the thickness feedback to decide the depth of cut. A stepper motor which works open loop could be good solution which would only consider the thickness feedback instead of a positional feedback. At the same time two feedbacks (positional feedback and thickness feedback) would make the process complicated by a servo motor setup. On the other side stepper motor would give higher torque in low speed operation. As the required change in the depth of cut would not exceed few mm, stepper motor is the right choice for the design.

Spindle motor selection

A light spindle motor is desired so that the manipulator arm can easily move it with limited deflection. Speed, torque and horse power requirement is important for selection of spindle motor. Cutting force are associated with depth of cut, width of cut, feed rate, number of cutter teeth and milling speed. While calculating horse power and torque requirement there are different formulas in different sources. Tool and Manufacturing Engineers Handbook (Cubberly and Bakerjian 1989) formula for spindle horsepower and torque is based on machinability factor.

HP = Machinability factor x peripheral speed of cutter, sfm x avg. cutter teeth no. x $0.00549(100A)^r$]

$$T = HP \times 5252/RPM$$

A formula obtained from an online milling horsepower calculator (CustomPartNet 2009) is

HP = Unit Power (Horsepower per cubic inches of mat. Remover/min) x Material removal rate (Cubic Inches per Minute)

$$T = HP \times 5252/RPM$$

The cutting tools manufacturing company Sandvik Coromant (Sandvik) uses different formulas for calculating spindle horsepower and torque requirement.

HP = Axial depth of cut x radial depth of cut x feed per tooth x spindle speed x number of teeth in tool x specific cutting force /396000

$T = 0.159 \times \text{cutting speed} \times \text{axial depth of cut} \times \text{feed per revolution} \times \text{specific cutting force/spindle speed}$

Each formula yield a different value for spindle horse power and torque requirement. A constraint speed of 12000 rpm and 1 mm depth of cut is taken in consideration for minimizing the spindle size.

Table 2: Lists the results for all three spindle power selection equation.

Formula Type →	Handbook	Web based	Sandvik
Spindle Power(kw)	5.50	4.73	4.11
Torque(N-m)	4.38	3.77	0.86
Spindle Power(HP)	7.38	6.35	5.52
Torque(lb-ft)	3.23	2.78	0.63

Based on the calculation results a spindle motor of 12000 RPM 3-5 KW and 2-5 Nm should be suitable for thin plate machining. There are some commercial spindle motor suppliers which meet the torque and power requirement.

Part assembly

A linear slide has been implemented which has a base 16" long x 8" wide. The sliding table part is 8" x 8" and has a travel of 6". The stepper motor and ball screw provide increments of 0.001 inch to meet the tolerance (± 0.002 inch / ± 0.050 mm) of the cut.

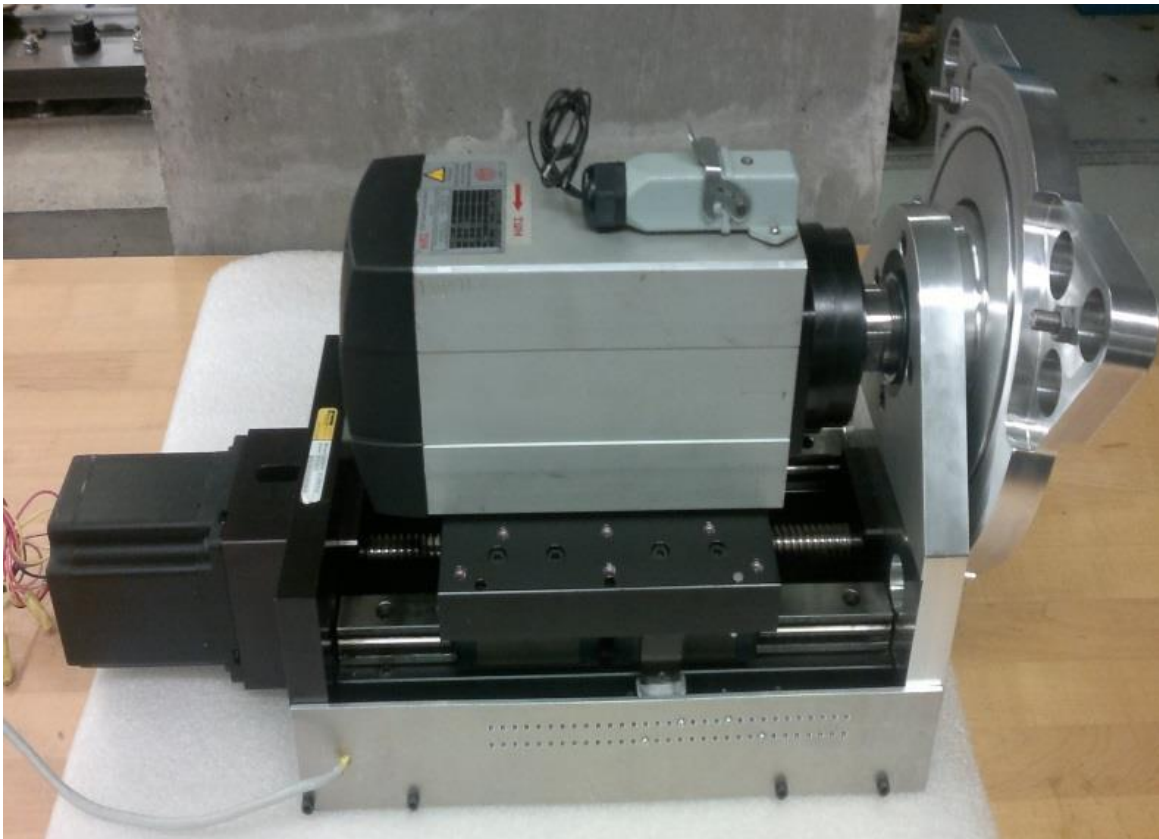


Figure 34: Complete end effector assembly.

5.6 Feedback control system

There are two options for a stepper motor control national instrument motion control card and Arduino based stepper driver. NI PCI-7352, NI UMI-7772 and SHC68-C68-S Cable (2m) combined cost 5000 CAD where the Arduino and stepper driver cost only 230 CAD. Being a student project Arduino got the priority in selection based on cost consideration.

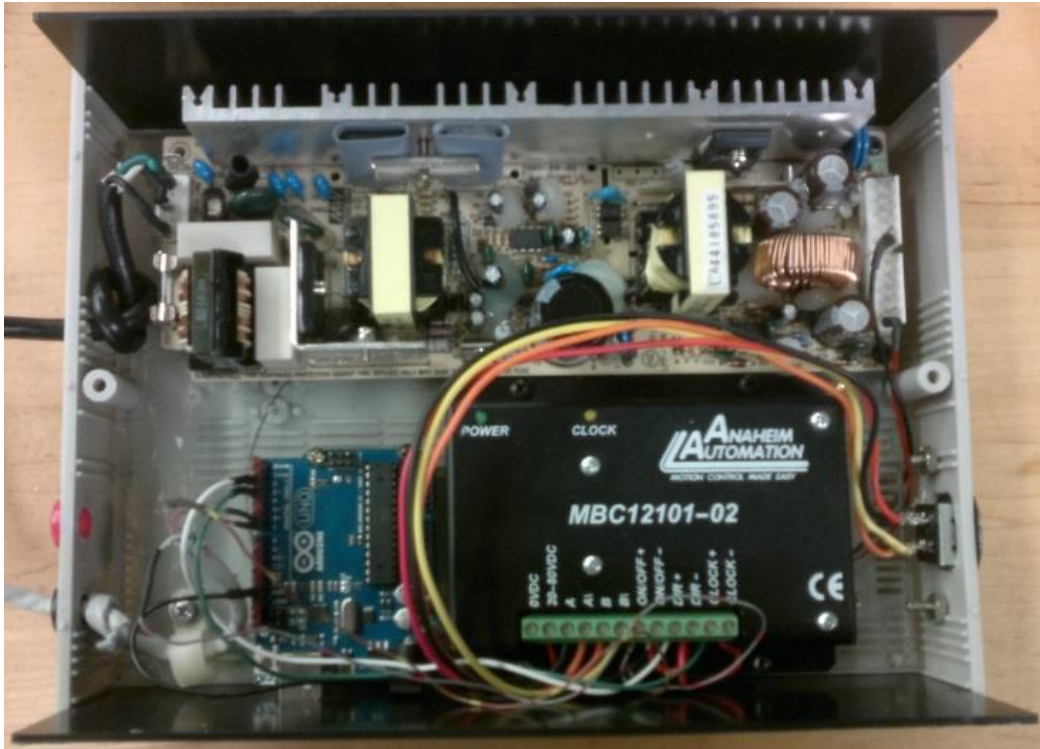


Figure 35: Stepper motor control box

An Arduino Uno microcontroller controls the stepper motor. Arduino is programmed with the Arduino Integrated developed environment (C language). Since the whole control loop uses the LabView platform, LabView-Arduino interfacing software (LVIFA_Base.pde – LabView interface for Arduino) has been utilized to establish the LabView Arduino communication.

A commercial thickness measurement device Olympus 38DL plus unit (Olympus 2014) processes the signal acquired from the sensor and sends the thickness data to the LabView program by a serial communication.

For ultrasonic sensor coupling liquid medium are necessary to transmit the ultrasonic waves from transmitter face to material face. A water circuit has to be establishing by a 125 GPH pond pump (28 inch height- 9.5 mm pipe output diameter) to maintain a constant water supply during milling operation. However, due to irregular coupling liquid water supply and other disturbances incoming thickness data fluctuates. A median filter has been included in the lab view program to remove spikes in the thickness indication.

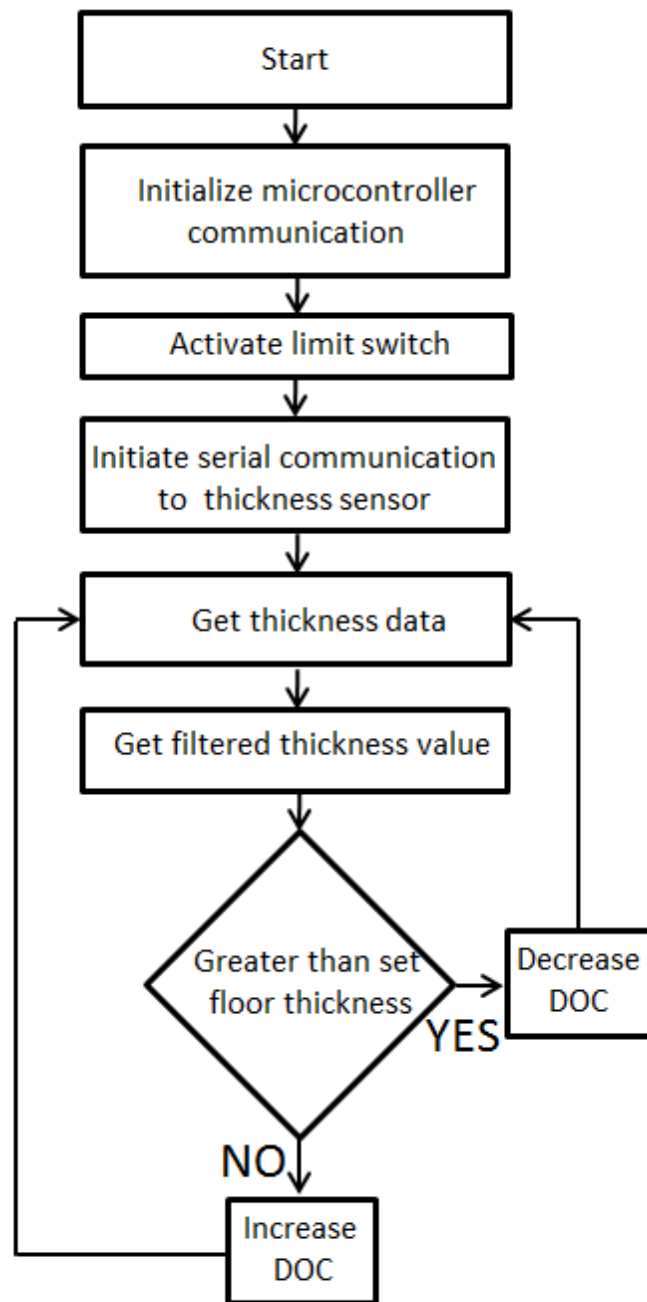


Figure 36: Lab View program flow chart for depth of cut (DOC) control.

5.7 Experiments and results

The prototype end effector has been tested inside a CNC machine tool (model Matsuura MC-760UX) for convenience prior to future control on robot manipulator to verify the capability. Y- and Z- axis are used to imitate the manipulator in-plane motion.



Figure 37: Experimental setup viewed from the master side

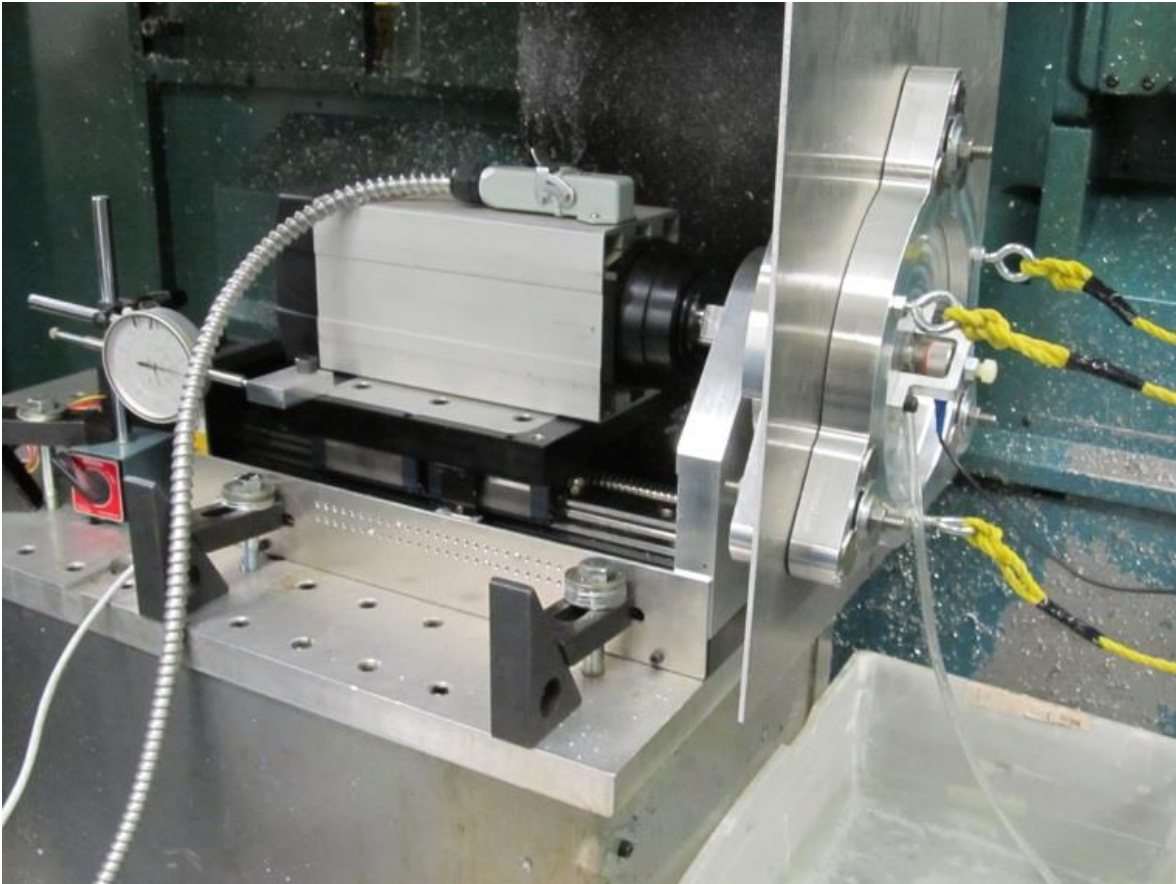


Figure 38: Experimental setup from slave side

Though the end effector design is capable of milling curved skin panel, the initial CNC setup did not permit to test curved panel. One square pocket (3.5 by 4.5 inch 2.75 mm floor bed thickness) has been milled with continuous remaining thickness feedback.



Figure 39: Interrupted feedback caused uneven remaining thickness.

A 5/8 inch diameter three flute milling tool was used at a feed rate of 1000 mm/min and 5000 rpm spindle speed. The pocket milling was performed in air cooling with 50 % step over. At the end of operation random position thickness measurements were gathered of the pocket floor thickness.

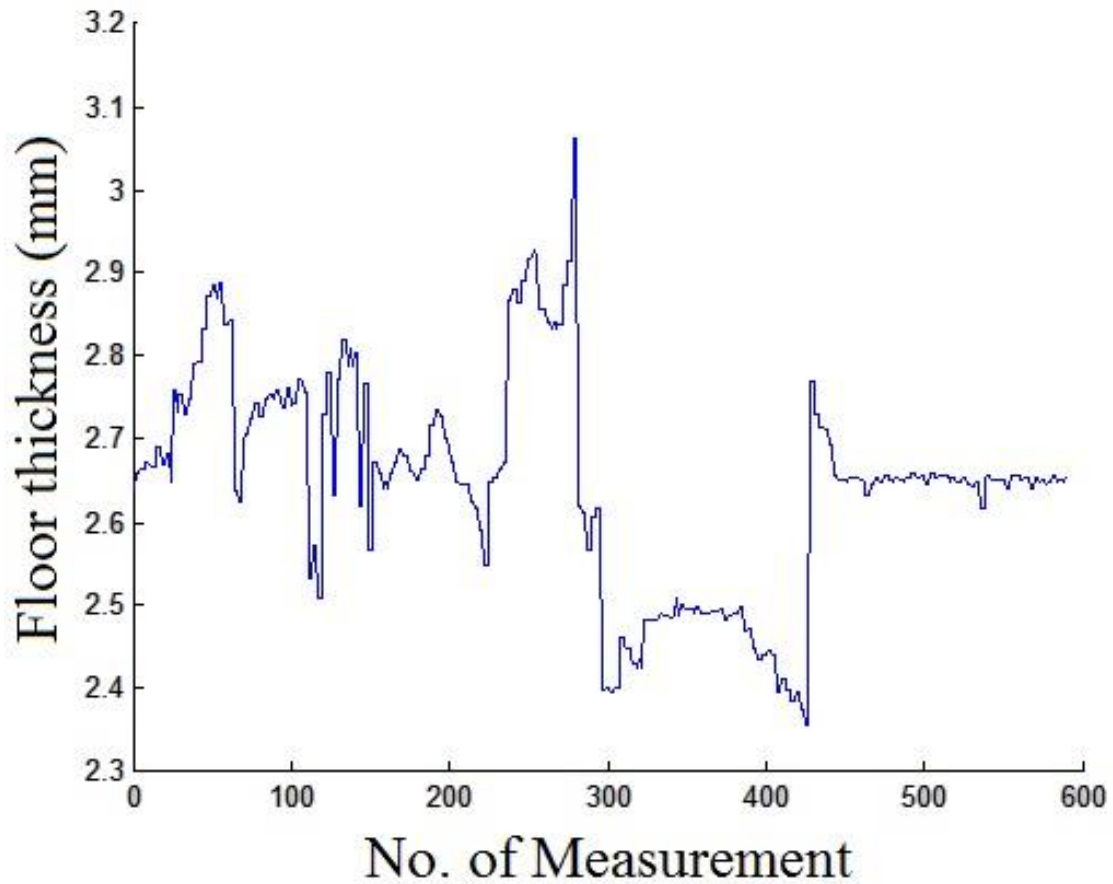


Figure 40: Random floor thickness in close loop pocket milling showing high thickness variation.

Due to interrupted reading from the ultrasonic sensor the thickness feedback was irregular. Another test was performed for the same pocket dimensions in open loop without the continuous thickness feedback with a pre-set depth of cut.



Figure 41: Open loop milling results in smoother surface finish.

Open loop operation resulted in a smoother surface finish compared the first test. Again random position floor thickness were measured by the ultrasonic thickness measurement device and plotted in Figure 42.

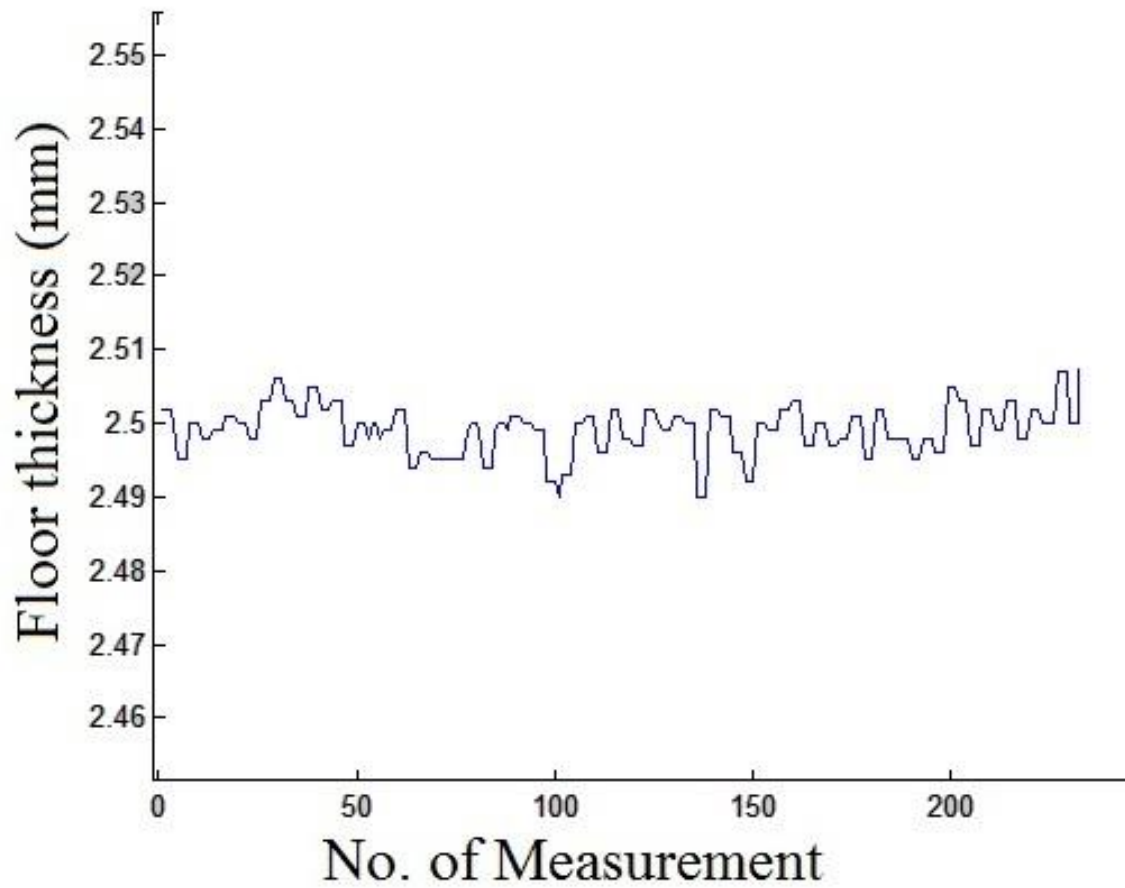


Figure 42: Random floor thickness in open loop pocket milling showing lower thickness variation.



Figure 43: Concept of a grasping end effector fixed on KUKA 500 KR-2 MT industrial robot for double curved skin panel pocket milling.

5.8 Conclusion

A grasping end effector design and implementation was accomplished based on the concept of a magnetic clamp. A mobile magnetic chuck (slave) follows the master module (the end effector) during the milling operation and continuously provides support from the opposite side against the milling thrust force. A double gimbal mechanism helps to follow the double curvature of the skin panel ensuring high milling efficiency. An ultrasonic sensor based feedback loop was integrated to cater for thickness variation. In this first version this features was not

successful.

The main problem encountered during the close loop operation is the high variation of the remaining floor thickness signal. The ultrasonic sensor could not provide a continuous thickness measurement due to interrupted coupling liquid flow. There were also issues with the panel peripheral fixturing allowing excessive panel twisting during the milling operation. Insufficient gripping also contributed to the resulting floor thickness variation.

REFERENCES

Anaheim , A. (2011). "MBC12101 - Stepper Drivers with DC Input (wiring diagram)." Retrieved 14th October, 2014, from <http://www.anaheimautomation.com/products/stepper/stepper-driver-item.php?sID=58&serID=15&pt=i&tID=86&cID=20>.

Bres, A., B. Monsarrat, et al. (2010). "Simulation of friction stir welding using industrial robots." Industrial Robot: An International Journal **37**(1): 36-50.

Cakir, O., A. Yardimeden, et al. (2007). "Chemical machining." Archives of Materials Science and Engineering **28**(8): 499-502.

Chapleau, S., É. Martin, et al. (2006). Results and Verification of Spacecraft Docking Emulation using Hardware-in-the-Loop Simulation. Romansy 16. T. Zielińska and C. Zieliński, Springer Vienna. **487**: 397-404.

Chouinard, A. (2011). Remplacement de l'usinage chimique des tooles aeronautiques minces en aluminium par de l'usinage mecanique. Departement de genie mecanique, Ecole Polytechnique de Montreal. **M Sc**.

Cubberly, W. H. and R. Bakerjian (1989). Tool and Manufacturing Engineers Handbook Desk Edition, Society of Manufacturing Engineers.

CustomPartNet (2009). "Milling Horsepower Calculator." Retrieved 14th October, 2014, from <http://www.custompartnet.com/calculator/milling-horsepower>.

Hamann, J.-C. (2007). Process and device for machining by windowing of non-deformable thin panels, Google Patents.

K&J magnetics, I. (2014). "DX0X0-N52." Retrieved 14th October, 2014, from <https://www.kjmagnetics.com/proddetail.asp?prod=DX0X0-N52>.

Martinez, M. T. (1992). Machine tool installation for supporting and machining workpieces, Google Patents.

Olympus (2014). "Thickness Gages 38DL PLUS." Retrieved 14th October, 2014, from <http://www.olympus-ims.com/en/38dl-plus/>.

Panczuk, R. and P.-Y. Foissac (2010). Process and a device for the machining of panels, Google Patents.

SANDVIK, C. Rotating Tools and Inserts, Milling drilling Boring and Holding. Sandvik Canada INC. 5675 Royalmount Avenue, Montreal Quebec.

Wikipedia (2014). "Neodymium magnet." Retrieved 14th October, 2014, from http://en.wikipedia.org/wiki/Neodymium_magnet.

CHAPTER 6 ARTICLE 3: DETERMINING THE MINIMUM CLAMPING FORCE BY CUTTING FORCE SIMULATION IN AEROSPACE FUSELAGE POCKET MACHINING

A. Mahmud, J.R.R Mayer, L. Baron (2015)

Published on Journal of Advanced Manufacturing Technology

Digital Object Identifier (DOI) -10.1007/s00170-015-7104-4

<http://link.springer.com/article/10.1007/s00170-015-7104-4>.

Abstract— In large fuselage milling operation the panel may deflect and vibrate due to milling thrust force. A clamp is needed on the opposite side of the panel to limit such effects. The support must be able to withstand the thrust force generated by the milling process. In this paper, a specific model for torus cutter milling force and a general milling force model have been simulated to predict the cutting forces. In order to get higher cutting efficiency the torus cutter need to adopt different tilt angle relative to the workpiece which changes the thrust force. An equation has been developed to predict the resulting thrust force on the skin panel at different tilting angle. Simulated thrust force results have been validated against dynamometer readings acquired during milling operation.

Index Terms— machining, milling, clamping force, torus cutter, cutter orientation, cutting force

6.1 Introduction

This paper describes a model and experiments to determine the minimum clamping force for a mobile magnetic clamp. A magnetic clamp (Chouinard 2011) which must withstand the thrust force from the milling operation also needs to move smoothly with low frictional force. Excessive clamping force creates large friction forces which hinder the sliding of the clamp.

Clamping force need to be optimized so that the clamp can provide sufficient support force against the milling thrust force while allowing the clamp to move against the frictional force. Higher clamping force helps to stabilize the fixture in out-of-plane motion but reduces the in-plane mobility motion due to increased frictional forces and may damage the panel surface.

Several camping force optimization technique have been proposed. The finite-element (FE) modeling approach is very common in fixture design and clamping force optimization for

machining operation. Most of the work has the drawback of large model size requiring higher computation cost. A more computationally efficient method (Liu, Wang et al. 2012) where one genetic algorithm based fixture layout and clamping force optimization method has been speeded up by a matrix size reducing method for solving FEM balance equation.

Rigid-body modeling which considers both the workpiece and the fixture as perfectly rigid solids has been applied (Wang and Pelinescu 2003) to solve the problem of clamping force optimization. An elastic method has been used to model workpiece-fixture deformation. B. Li et al (Li and Melkote 2001) estimated optimum clamping forces for a multiple clamp fixture subjected to quasi-static machining forces by solving a multi-objective constrained optimization model. The algorithm for clamping force optimization represents the fixture-workpiece contact as elastic contacts.

An unconstrained nonlinear programming technique has been used to predict contact forces by Xiong et al (Xiongand, Xiong et al. 2003) and constrained quadratic optimization programming has been used by Wang and Pelinescu et al (Wang and Pelinescu 2003) to estimate the contact forces for known clamping force. Trappey et al (Trappey and Liu 1992) solved quadratic model of clamping forces including contact force by nonlinear programming whereas G Qin et al (Qin, Lu et al. 2009) feasibly slacked constrained quadratic optimization into constrained linear programming problem to determine required clamping force to stabilize the workpiece.

Particle Swarm Optimization (PSO) techniques featuring computational intelligence has been used for clamping force optimization by Deng and Melkote (Deng and Melkote 2006). The clamping force optimization problem was formulated as a bi-level constrained nonlinear programming problem to find the 'best' set of clamping forces swiftly.

Balancing force-moment method and the coulomb static friction law were used to determine minimum clamping force to hold the workpiece without deformation by S. Selvakumar et al.(Selvakumar, Arulshri et al. 2010) The optimum clamping force is selected as the maximum clamping forces calculated from five different tool positions with respect to the workpiece.

All the above mentioned clamping force optimization method assume the workpiece and clamping fixture are in static contact with no relative displacement. In case of a mobile magnetic clamp which slides over the workpiece (fuselage skin panel) also must provide sufficient

clamping force to withstand milling thrust force. So these solutions are not applicable for a mobile magnetic clamping fixture.

In milling operation cutter axis tilting is common which changes the axial thrust force by adding the projection of tangential and radial forces to the axial thrust force. The paper analyses the thrust force generated by the milling cutter at different tilt angles and takes the maximum thrust force as the minimum clamping force. For this purpose a torus milling cutter forces is simulated varying the inclination angle and the prediction verified experimentally.

6.2 Thrust force model

Using a toroidal tool and appropriate tilting and cutting tool displacement direction in relation to surface curvature improves the cutting efficiency (Balazinski, Gravelle et al. 1998). Since this tilted tool axis introduces different thrust force to the milling surface compared to the perpendicular situation, it is important to understand and quantify the forces in order to design the clamping device.

Altintas and Lee (Altintas and Lee 1998) expressed cutting forces as a function of cutting pressure exerted on the instantaneous uncut chip area.

$$\begin{aligned}
 F_t(\theta) &= K_t(\theta) * d_a * f_t \sin(\theta) \\
 F_r(\theta) &= K_r * F_t(\theta) \\
 F_a(\theta) &= K_a * F_t(\theta)
 \end{aligned}
 \tag{6.1}$$

Where f_t is the feed per tooth, d_a is the axial engagement and θ is the angular (around the tool axis) position of the torus cutter. The cutting force coefficient $K_t(\theta)$ depends on the material characteristics and cutter geometry. K_r and K_a coefficients are calculated from the ratios of maximum radial to tangential and axial to tangential forces respectively.

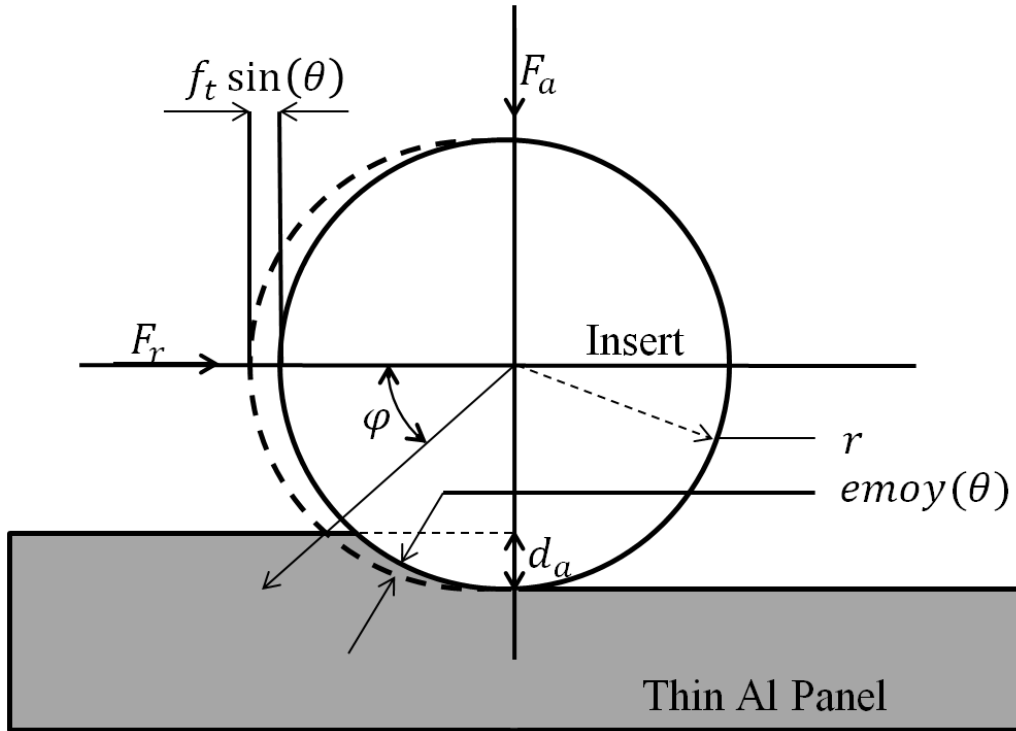


Figure 44: Average chip thickness $emoy(\theta)$ and axial engagement d_a

P. Gilles et al. (Gilles, Monies et al. 2006) expressed this cutting coefficient for torus milling cutter as a combination of two different coefficient K_{to} and β .

$$K_t(\theta) = K_{to}(emoy(\theta))^\beta \quad (6.2)$$

where the average chip thickness $emoy(\theta)$ is function of the cutting parameter and the cutter geometry (Figure 44).

$$emoy(\theta) = \frac{f_t \sin(\theta) * d_a}{r(\pi/2 - \varphi)} \quad (6.3)$$

with $\varphi = \sin^{-1}\left(\frac{r-d_a}{r}\right)$.

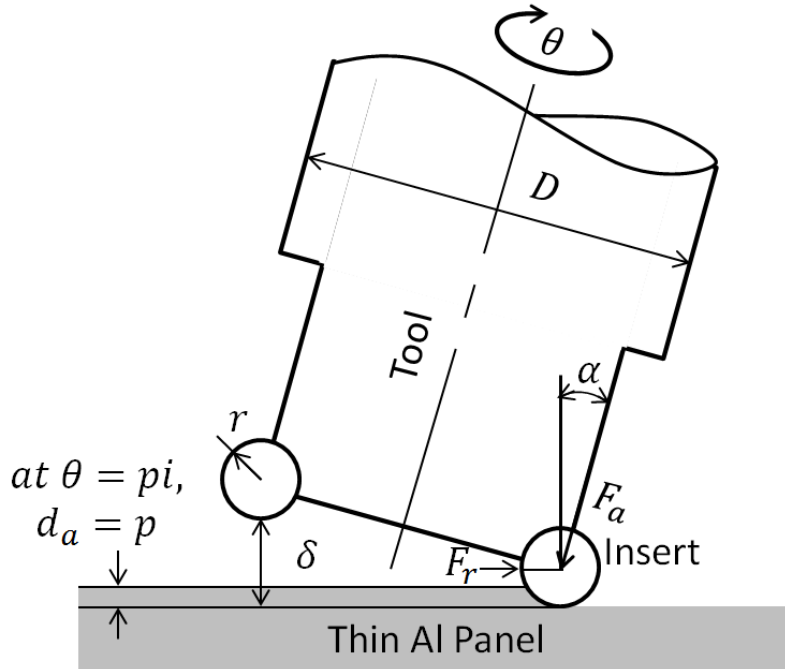


Figure 45: Axial engagement d_a for constant depth of cut p

The average chip thickness $emoy$ depends on the axial engagement d_a . If the cutter axis has a negative tool axis inclination (Gilles, Monies et al. 2007) axial engagement also changes. To maintain the constant depth of cut, p , the axial engagement changes (Figure 45).

$$d_a = \left(p - \frac{\delta}{2}\right) + \frac{\delta}{2} \sin(\theta), d_a(\leq 0) = 0 \quad (6.4)$$

$$\delta = (D - 2r) \sin(\alpha)$$

where D is the tool diameter, r is the round insert radius and α is the inclination angle. Any negative d_a value indicates no axial engagement.

A logarithmic residue matrix method has been established to calculate coefficient K_{to} and β of equation 6.2 by P. Gilles et al. (Gilles, Monies et al. 2006)

$$\begin{aligned}
& \begin{pmatrix} \text{Number of points} & \sum_i \log(\text{emoy}(\theta_i)) \\ \sum_i \log(\text{emoy}(\theta_i)) & \sum_i (\log(\text{emoy}(\theta_i)))^2 \end{pmatrix}_{2 \times 2} \times \begin{pmatrix} \log(K_{to}) \\ \beta \end{pmatrix}_{2 \times 1} \\
& = \begin{pmatrix} \sum_i \log(F_{t_i}) \\ \sum_i [\log(F_{t_i}) \log(\text{emoy}(\theta_i))] \end{pmatrix}_{2 \times 1} \\
& - \begin{pmatrix} \sum_i \log(d_{af_t} \sin(\theta_i)) \\ \sum_i [\log(d_{af_t} \sin(\theta_i)) \log(\text{emoy}(\theta_i))] \end{pmatrix}_{2 \times 1}
\end{aligned} \tag{6.5}$$

Assuming α is around an axis perpendicular to the feed direction and let's say this is the X-axis, then $R_x(\alpha)$ is the rotation matrix describing the tilt action on the tool body.

$$R_x(\alpha) = \begin{vmatrix} 1 & 0 & 0 \\ 0 & \cos(\alpha) & -\sin(\alpha) \\ 0 & \sin(\alpha) & \cos(\alpha) \end{vmatrix} \tag{6.6}$$

Then defining the tool axis as the Z-axis resulting from α the rotation matrix about the Z-axis is $R_z(\theta)$.

$$R_z(\theta) = \begin{vmatrix} \cos(\theta) & -\sin(\theta) & 0 \\ \sin(\theta) & \cos(\theta) & 0 \\ 0 & 0 & 1 \end{vmatrix} \tag{6.7}$$

Calculated cutting forces $F_t(\theta)$ $F_r(\theta)$ and $F_a(\theta)$ in the local (tool) reference frame are projected in the workpiece fixed reference. Considering the tool rotation about the Z axis and tilting angle about X axis cutting force components in workpiece frame are $F_x(\alpha)$ $F_y(\alpha)$ and $F_z(\alpha)$.

$$\begin{bmatrix} F_x(\alpha) \\ F_y(\alpha) \\ F_z(\alpha) \end{bmatrix} = \begin{vmatrix} 1 & 0 & 0 \\ 0 & \cos(\alpha) & -\sin(\alpha) \\ 0 & \sin(\alpha) & \cos(\alpha) \end{vmatrix} \times \begin{vmatrix} \cos(\theta) & -\sin(\theta) & 0 \\ \sin(\theta) & \cos(\theta) & 0 \\ 0 & 0 & 1 \end{vmatrix} \times \begin{bmatrix} F_r(\theta) \\ F_t(\theta) \\ F_a(\theta) \end{bmatrix} \quad (6.8)$$

$$= \begin{vmatrix} \cos(\theta) & -\sin(\theta) & 0 \\ \cos(\alpha) \sin(\theta) & \cos(\alpha) \cos(\theta) & 0 \\ \sin(\alpha) \sin(\theta) & \sin(\alpha) \cos(\theta) & \cos(\alpha) \end{vmatrix} \times \begin{bmatrix} F_r(\theta) \\ F_t(\theta) \\ F_a(\theta) \end{bmatrix} \quad (6.9)$$

Clamping forces in all three directions are important. However the magnetic chuck (Chouinard 2011) aims at counteracting the Z-axis force to support the thin panel from the rear side. So the Z-axis force only is considered from now on.

The thrust force $F_z(\alpha)$ is the force that the milling cutter applies to the milled object in the out-of-plane direction. The thrust force depends on the tool inclination angle. Tilting caused change in inclination angle. Tilting angle α theoretically could vary from 0 to 90 degrees.

$$F_z(\alpha) = \sin(\alpha) \sin(\theta) * F_r(\theta) + \sin(\alpha) \cos(\theta) * F_t(\theta) + \cos(\alpha) * F_a(\theta) \quad (6.10)$$

$F_z(\alpha)$ can be expressed including K_r and K_a coefficients using equation 6.1.

$$F_z(\alpha) = F_t(\theta)(\sin(\alpha) \sin(\theta) * K_r + \sin(\alpha) \cos(\theta) + \cos(\alpha) * K_a) \quad (6.11)$$

6.3 Experimental setup

A Kistler dynamometer has been installed on a 5 axis CNC machine (HURON KX8 – 5 axes). A torus cutter (model- ER D038A075-2-MIO-0.38) is fixed to the spindle which rotates at 5000 rpm. On the tool (diameter, $D = 19.05$ mm) one of the two inserts (radius, $r = 9.652$ mm) is removed to perform a single insert milling operation.

Milling is performed with a feed rate of 400 mm/min in air cooling. The single insert resulted in a feed per tooth $f_t=0.08$ mm. A thin aluminum (AL2024-T3) plate is placed on top of the dynamometer using a specially designed fixture.

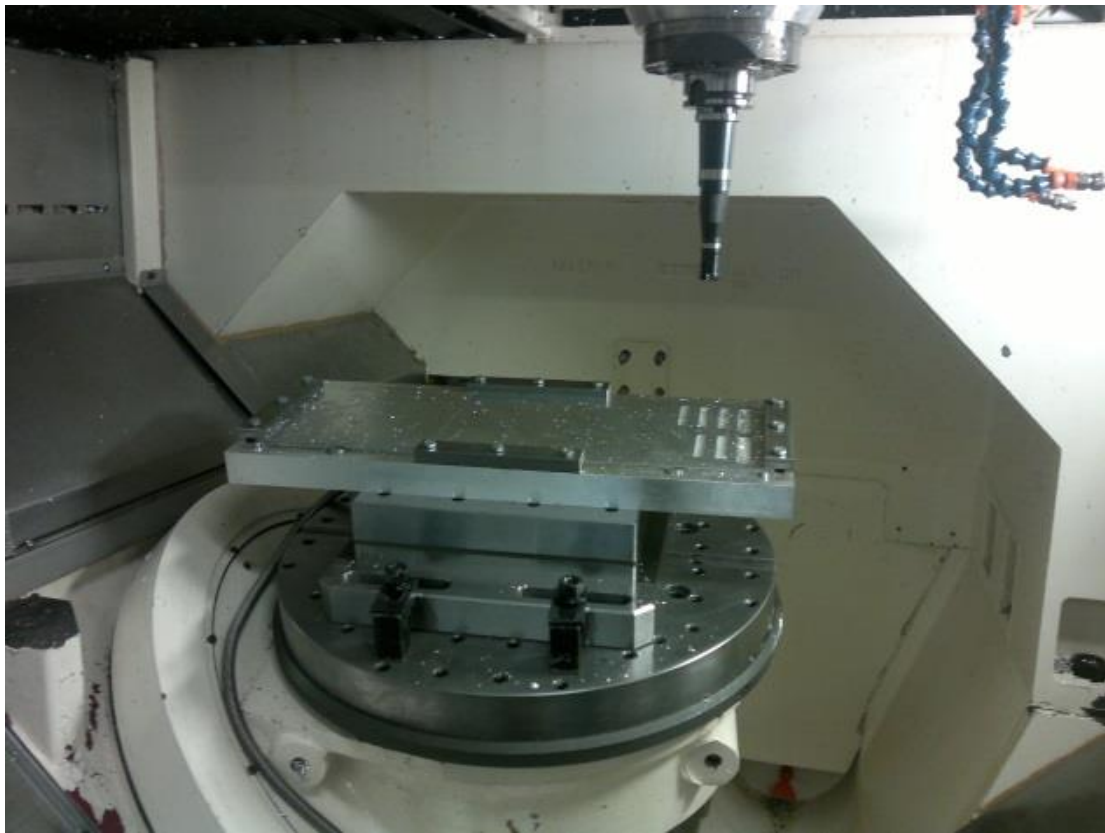


Figure 46: Kistler dynamometer fixed on the CNC machine bed (model-HURON KX8)

The dynamometer is connected to a data acquisition system, PXI 1006B chassis including two 8 channel cards PXI 4472 via the amplifier (Figure 4). The computer shows the measured force in a Lab View VI shown in Figure 5.



Figure 47: LabView based data acquisition system with Kistler Dynamometer

The dynamometer measures three forces in the fixed workpiece reference frame (X, Y and Z) in three 2D graphs. Data are also recorded as a .txt file for further analysis. The sampling frequency of the force data acquisition was 1000 Hz.

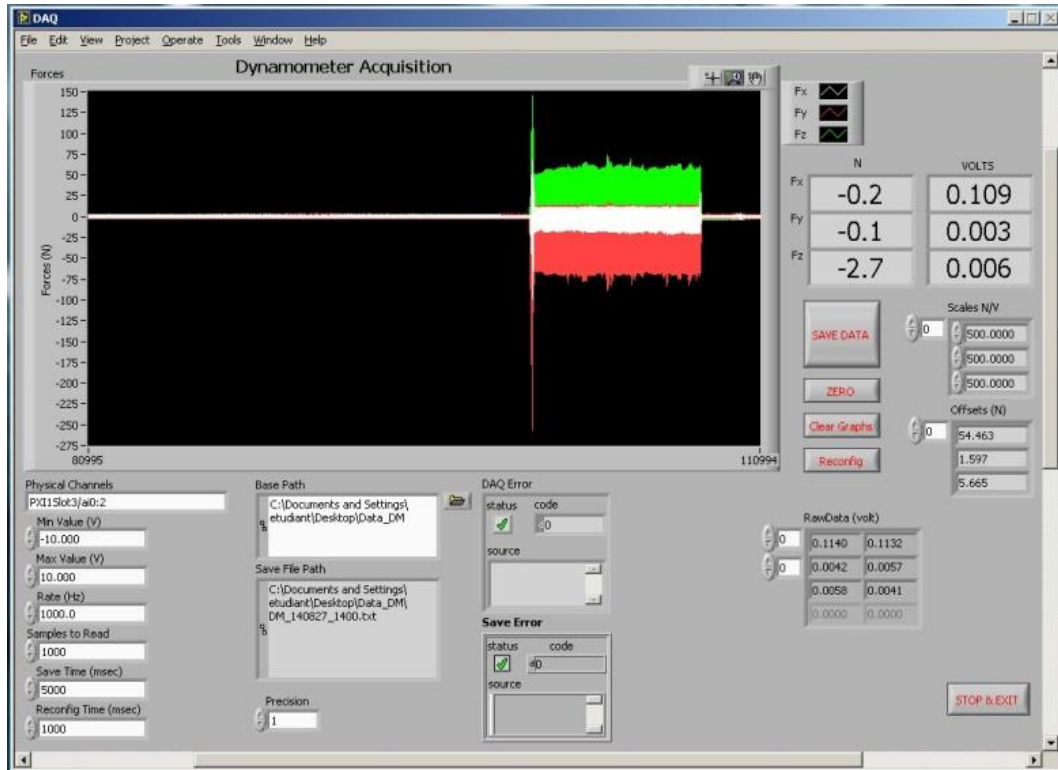


Figure 48: Measured forces F_x , F_y and F_z in fixed workpiece reference frame

6.4 Simulated thrust force

The cutting force data measured by the Kistler dynamo meter is in the fixed workpiece reference framework with three cutting force components F_x , F_y and F_z . Tangential, radial and axial forces on the local (tool) frame are $F_t(\theta)$, $F_r(\theta)$ and $F_a(\theta)$.

At zero degree inclination ($\alpha = 0$) equation 6.9 takes the form

$$\begin{bmatrix} F_x(\alpha) \\ F_y(\alpha) \\ F_z(\alpha) \end{bmatrix} = \begin{bmatrix} \cos(\theta) & -\sin(\theta) & 0 \\ \sin(\theta) & \cos(\theta) & 0 \\ 0 & 0 & 1 \end{bmatrix} \times \begin{bmatrix} F_r(\theta) \\ F_t(\theta) \\ F_a(\theta) \end{bmatrix} \quad (6.12)$$

The experimental setup measures forces in fixed reference system which needs to be converted to forces in local frame. Inverse matrix helps to switch from fixed reference frame to local frame.

$$\begin{bmatrix} F_r(\theta) \\ F_t(\theta) \\ F_a(\theta) \end{bmatrix} = \begin{bmatrix} \cos(\theta) & \sin(\theta) & 0 \\ -\sin(\theta) & \cos(\theta) & 0 \\ 0 & 0 & 1 \end{bmatrix} \times \begin{bmatrix} F_x(\alpha) \\ F_y(\alpha) \\ F_z(\alpha) \end{bmatrix} \quad (6.13)$$

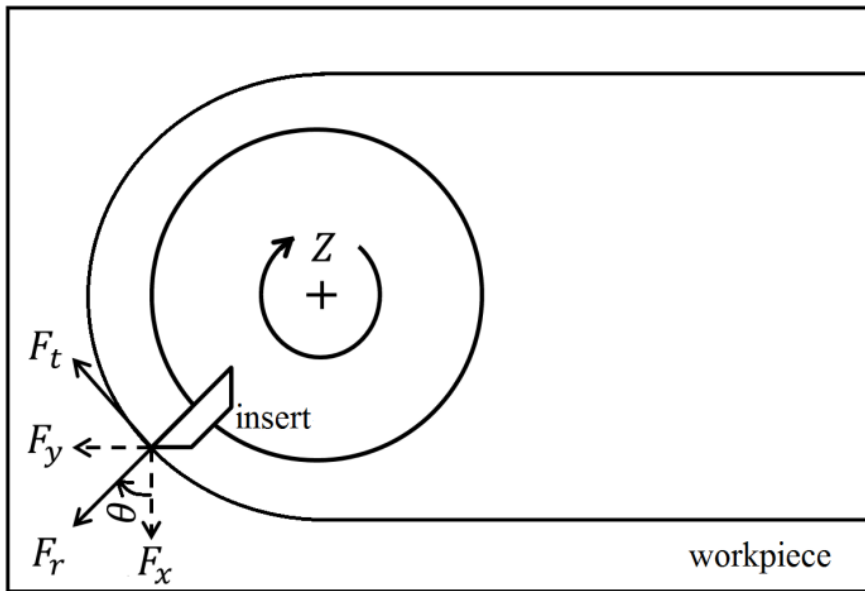


Figure 49: Fixed workpiece reference system to local reference system force components conversion

The experimentally measured forces $F_x(\theta)$, $F_y(\theta)$ and $F_z(\theta)$ are plotted using Matlab and then rotation matrix calculates the radial $F_r(\theta)$ tangential $F_t(\theta)$ and axial $F_a(\theta)$ forces on the local (tool) reference system.

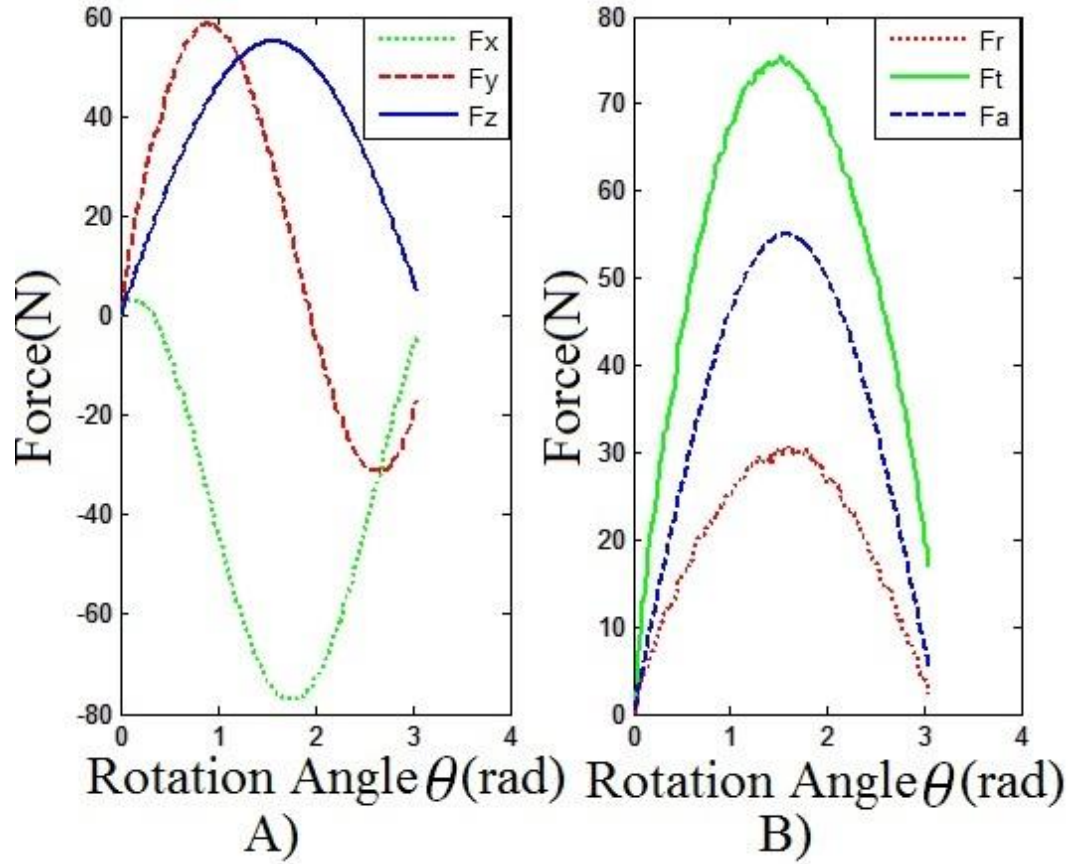


Figure 50: Experimental force data (A: fixed workpiece reference) and calculated force data (B: local reference system) at $\alpha = 0$ deg

Forces in local (tool) reference system could be effectively used to calculate the two model parameters K_{to} and β by equation 6.5. Calculated values for $K_{to} = 785.94$ MPA and $\beta = -0.2210$

Average chip thickness $emoy(\theta)$ is calculated from axial engagement d_a based on the tool axis inclination angle α and tool rotation angle, θ . Without any tilting (inclination angle, $\alpha = 0$) axial engagement d_a remains equal to the required depth of cut p . As soon as tilting increases, axial engagement changes with tool rotation.

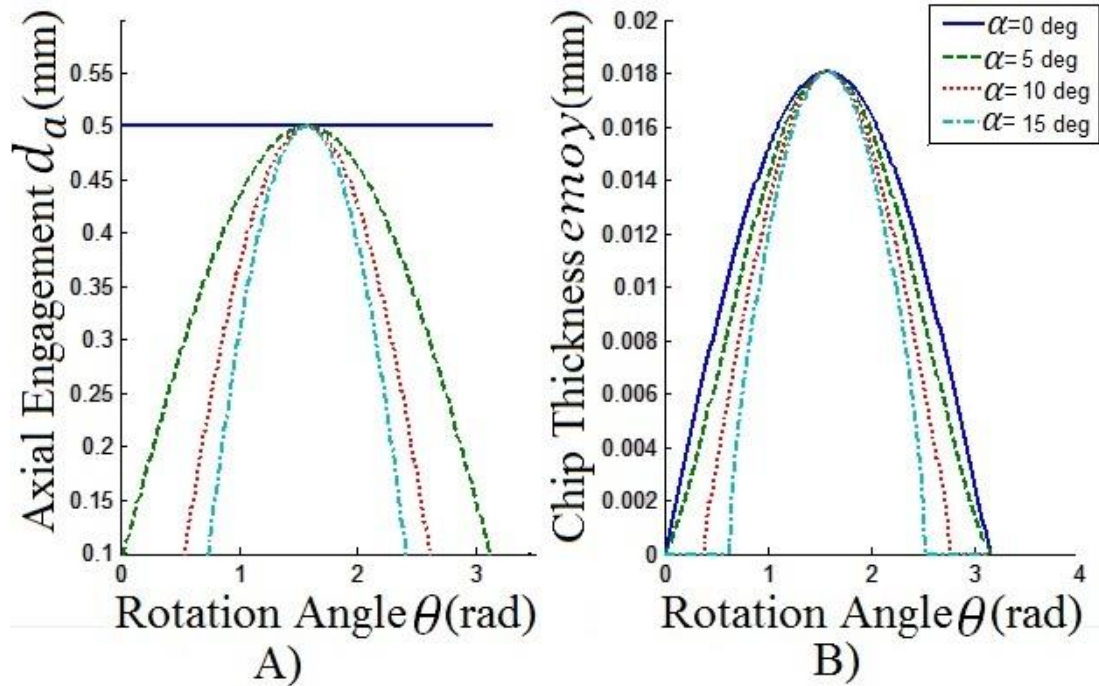


Figure 51: A: axial engagement, d_a B: average chip thickness, e_{moy} at different tilting angle ($\alpha = 0, 5, 10, 15$ deg)

Figure 51 shows that for a constant depth of cut of 0.5 mm axial engagement changes from 0 to 0.5 mm at different rotation angle. Based on equation 6.3 the corresponding e_{moy} (average chip thickness) has been calculated.

Finally equation 6.2 is used to calculate $K_t(\theta)$. Ratios of maximum radial to tangential and axial to tangential forces respectively determine K_r and K_a . These two ratios have been identified by equation 6.1

$$K_r = 0.4090 \quad K_a = 0.7308$$

With all the available data of cutting force coefficient, axial engagement, radial to tangential and axial to tangential ratios equation 6.1 can simulate all three radial tangential and axial forces without considering any tool inclination. These simulated cutting forces have been transformed to fixed reference frame for comparing to the force data acquired at zero degree tilting milling operation, $\alpha = 0$.

At zero degree inclination the measured average maximum axial forces for a 0.5 mm depth of cut is 55.60 N whereas the calculated axial force based on P. Gilles's formula is 55.73

N.

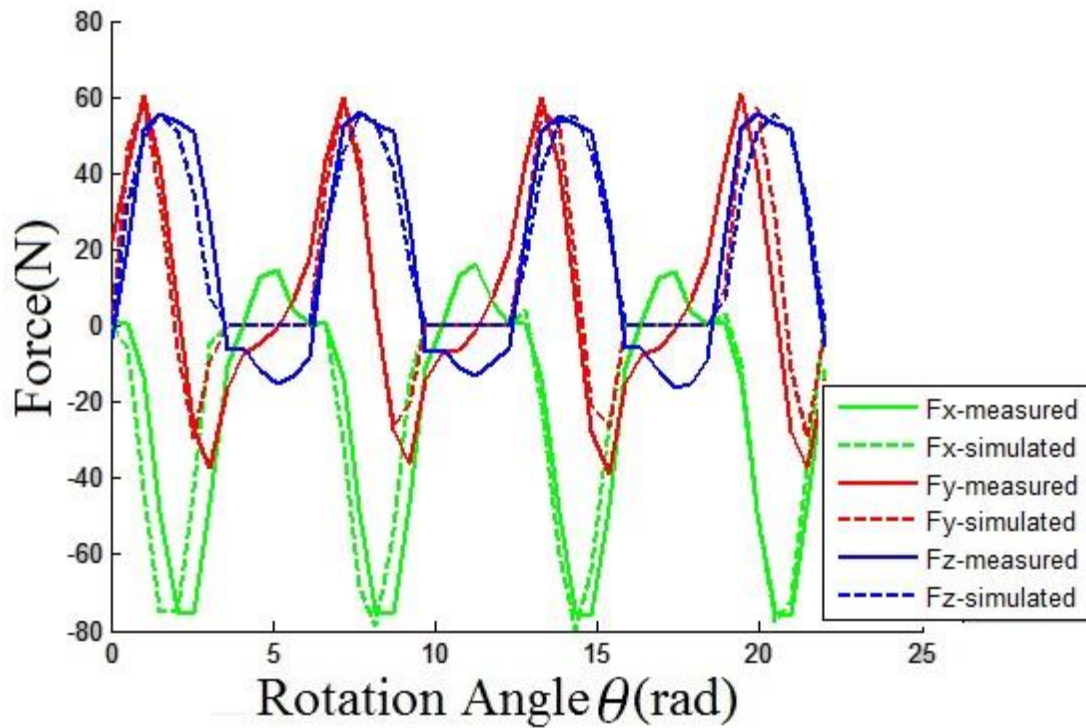


Figure 52: Simulated versus measured cutting forces with no tilting angle ($\alpha = 0$ deg) in fixed framework

The main interest of this work is to estimate the thrust force on the milling surface. Without any inclination the thrust force is straightforward and is calculated as the axial. As soon as the cutter axis is tilted, i. e. α is increased, both the tangential and radial forces influence the axial force by a factor of $\sin(\alpha)$. At the same time axial force itself gets reduced by a factor of $\cos(\alpha)$ as seen in equation 6.10.

To verify the combined effect these $\sin(\alpha)$ and $\cos(\alpha)$ factors on the thrust force three different test were accomplished at tilting angles 5, 10 and 15 degrees.

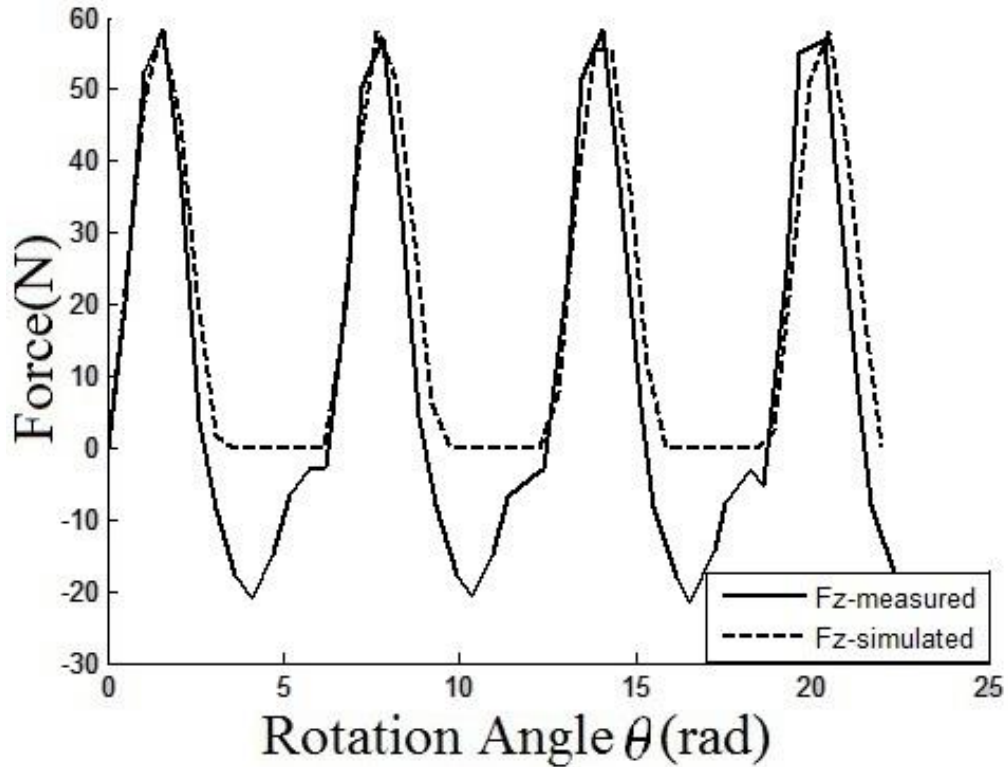


Figure 53: Thrust force at 5 degree tilting angle ($\alpha = 5$ deg)

Equation 6.11 predicts the thrust force. The average maximum thrust force was 55.60 N without any tilting angle, only a 5 degree tilting changes the amount to 57.77 N, which is close to the simulated maximum axial force of 58.53 N. A further tilting of 5 degree ($\alpha = 10$ deg) increases the thrust force to 60.10 N. Simulated thrust force at 10 degree tilting is 60.98 N.

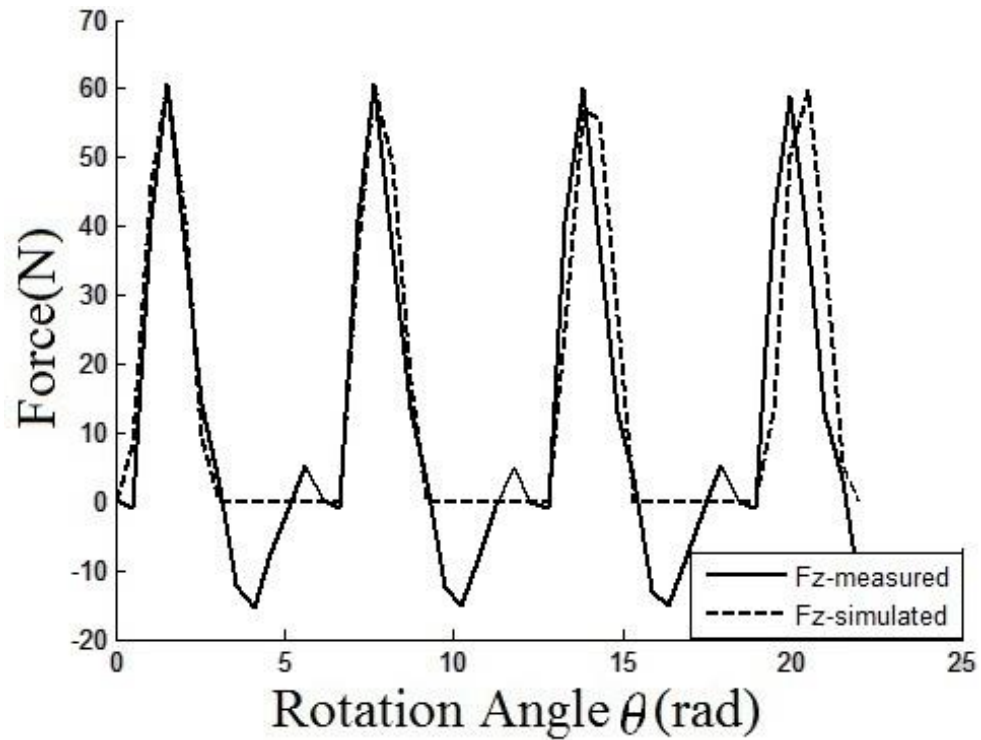


Figure 54: Thrust force at 10 degree tilting angle ($\alpha = 10$ deg)

In a five axis CNC milling operation 10 to 15 degree tilting angle is very common. An additional test has been performed at 15 degree inclination shows a further increased thrust force to 62.60 N matched by the simulated maximum force of 62.95 N.

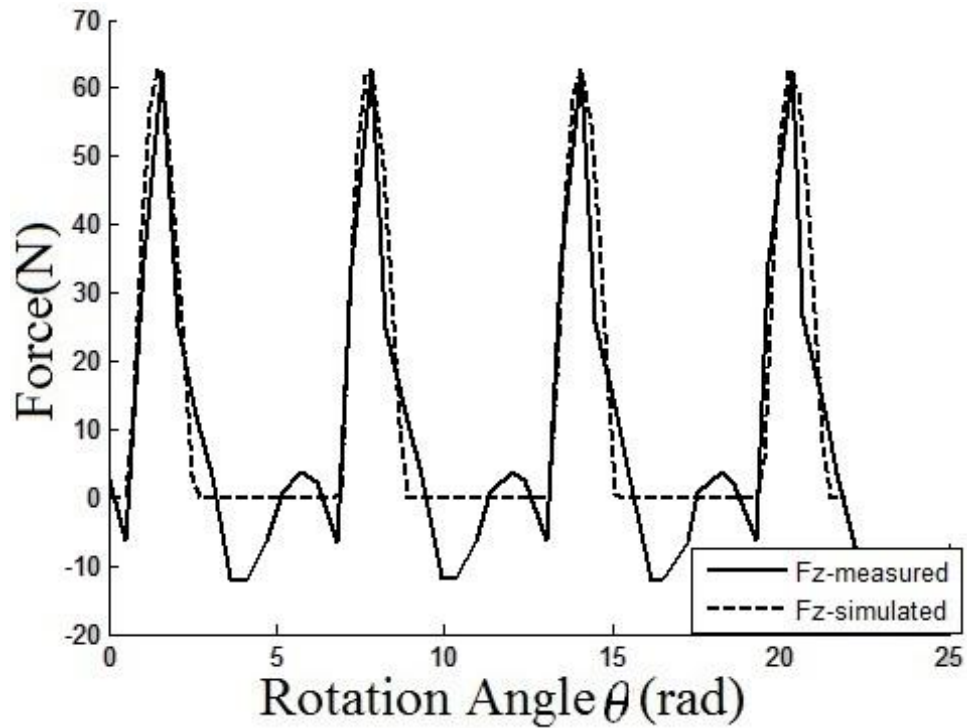


Figure 55: Thrust force at 15 degree tilting angle ($\alpha = 15$ deg)

After measuring 0 (without any tilting) to 15 degree tilting angle and their corresponding thrust forces, it is necessary to get the trend how tilting angle influences the thrust force and what is the maximum possible thrust force. All theoretically possible tilting angles have been simulated at 1 degree interval and the corresponding maximum thrust forces plotted in Figure13.

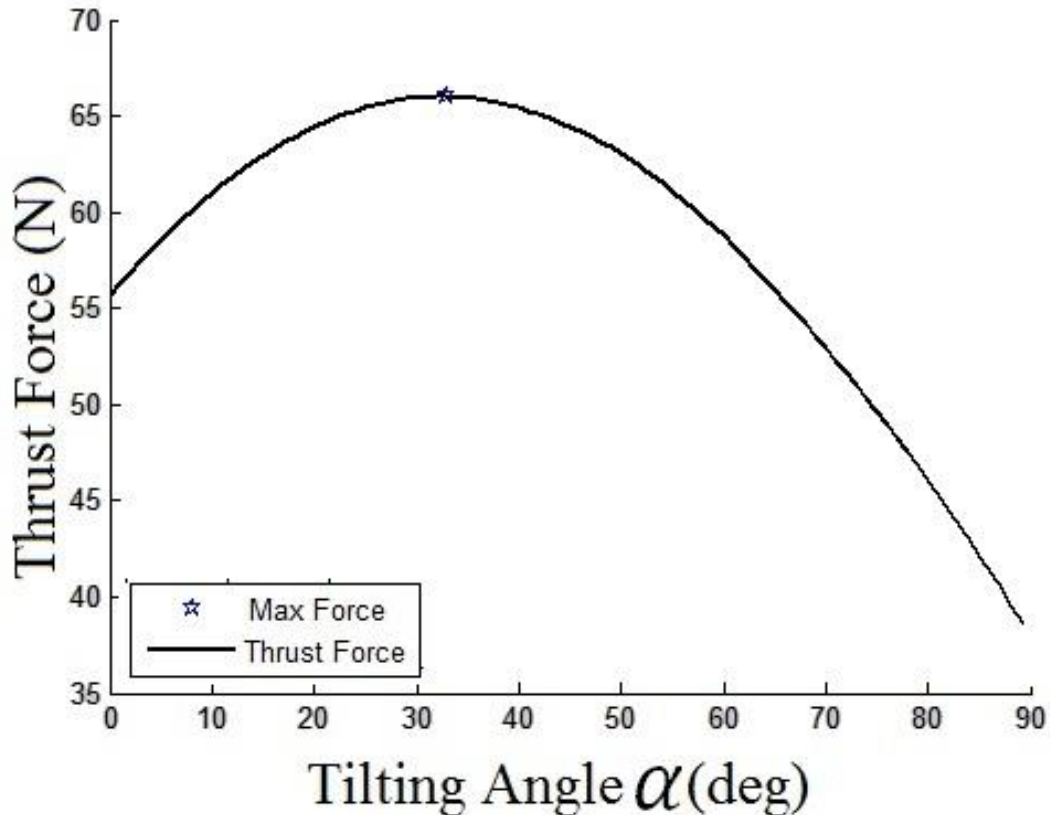


Figure 56: 0 to 90 degree tilt angle and corresponding thrust force

Simulations yield a maximum thrust force of 65.99 N at an inclination angle of 34 degree ($\alpha = 34$ deg). Theoretically this force needs to be supported by a clamping fixture so that the workpiece remains in position while milling.

6.5 Results and verification

Theoretically the tilting angle could be wide range from 0 to 90 degree. But in reality the tilting angle does not need to be so extreme. A moderate tilting angle could be 10 to 15 degrees. And specially the magnetic milling device for which this chuck is been designed can only attain a 10 to 15 degree tilting at its best. So experiments were also conducted up to 15 degree inclination

The same method could be applied for predicting maximum thrust force multiple teeth milling cutter by changing corresponding material characteristics and geometric data.

6.6 Conclusion

Whereas clamping on the panel periphery is imparted to support gravitational and inertial forces, the cutting force requires local support of the panel. A magnetic clamp for local support needs to provide sufficient force to keep the panel in position. If the magnetic clamp can support the maximum milling thrust force the fuselage skin panel will be correctly held.

Since torus cutter offer the probability of higher material removal rate by the tilting of the tool with respect to the panel surface in this paper a methodology has been established to predict the maximum thrust force produced from this cutting operation. First of all considering the cutter geometry and cutting operation variable (depth of cut, rpm, tool inclination or tilt) thrust forces have been simulated. Evaluating all the possible thrust force at different tilting angle, the maximum force is determined. The maximum thrust force for this specific milling case was 66 N which is the minimum clamping force for the magnetic clamp design.

REFERENCES

- Altintas, Y. and P. Lee (1998). "Mechanics and dynamics of ball end milling." Journal of manufacturing science and engineering **120**(4): 684-692.
- Balazinski, M., S. Gravelle, et al. (1998). Evaluation of the distance between the machining of assists for the tool tip-ring. 2nd International Conference on designing and manufacturing integrated mechanical IDMME`98. Compiegne, France: May 27-29 pp 569-575.
- Chouinard, A. (2011). Remplacement de l'usinage chimique des tooles aeronautiques minces en aluminium par de l'usinage mecanique. Departement de genie mecanique, Ecole Polytechnique de Montreal. **M Sc**.
- Deng, H. and S. N. Melkote (2006). "Determination of minimum clamping forces for dynamically stable fixturing." International Journal of Machine Tools and Manufacture **46**(7): 847-857.
- Gilles, P., F. Monies, et al. (2006). "Modelling cutting forces in milling on torus cutters." International Journal of Machining and Machinability of Materials **1**(2): 166-185.

Gilles, P., F. Monies, et al. (2007). "Optimum orientation of a torus milling cutter: method to balance the transversal cutting force." International Journal of Machine Tools and Manufacture **47**(15): 2263-2272.

Li, B. and S. Melkote (2001). "Fixture clamping force optimisation and its impact on workpiece location accuracy." The International Journal of Advanced Manufacturing Technology **17**(2): 104-113.

Liu, Z., M. Y. Wang, et al. (2012). One Fast Fixture Layout and Clamping Force Optimization Method Based on Finite Element Method. ASME/ISCIE 2012 International Symposium on Flexible Automation, American Society of Mechanical Engineers.

Qin, G., D. Lu, et al. (2009). A slack-based method to clamping force optimization for fixture design. Information and Automation, 2009. ICIA'09. International Conference on, IEEE.

S. Selvakumar, K. P. A., K.P. Padmanaban and K.S.K. Sasikumar (2010). "Clamping Force Optimization for Minimum Deformation of Workpiece by Dynamic Analysis of Workpiece-fixture System." World Applied Sciences Journal **11**(7): 840-846.

Trappey, A. and C. Liu (1992). "An automatic workholding verification system."

Wang, M. Y. and D. M. Pelinescu (2003). "Contact force prediction and force closure analysis of a fixtured rigid workpiece with friction." Journal of manufacturing science and engineering **125**(2): 325-332.

Xiongand, C.-H., Y.-L. Xiong, et al. (2003). On Prediction of Passive Contact Forces of Workpiece-Fixture Systems. ASME 2003 International Design Engineering Technical Conferences and Computers and Information in Engineering Conference, American Society of Mechanical Engineers.

CHAPTER 7 ARTICLE 4: MODELING OF LATERALLY SLIDING MOTION OF A MAGNETIC CLAMP

A. Mahmud, J.R.R Mayer, L. Baron (2015)

Submitted to Journal of Vibration and Control

Abstract—A sliding magnetic clamp is used to hold a thin aluminum panel during a milling operation. The design includes a permanent magnet group follower (slave module) which slides laterally over the panel attracted by another permanent magnet group (master module) attached to the industrial robot end effector from the machined side of the panel. The lateral sliding motion of the slave module in response to the master module motion is studied using a transfer function based motion model established considering the lateral magnetic stiffness. The model is validated experimentally.

Keywords — system identification, motion control, modeling of dynamic system, sensors, pocket machining

7.1 Introduction

This paper proposes a model for the lateral sliding motion of the master to slave module by magnetic attraction forces. The grasping end effector is intended to mill pockets in thin skin panel with the support of magnetic clamping. The system is developed for holding a panel during milling operation. The clamping system includes two magnetic modules which are placed either side of the panel. Figure 57 shows a general schematic of the grasping machining end effector (Chouinard 2011).

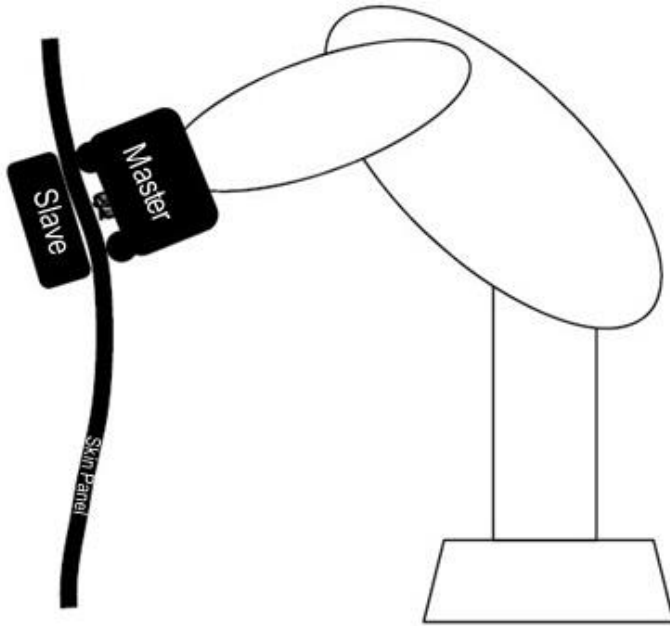


Figure 57: General schematic diagram of the grasping machining end effector concept

The master module has three cylindrical permanent magnets set, each set comprising three magnets (Figure 58). The milling cutter is at the center of the triangle formed by these three magnet sets. The slave module has a similar magnet arrangement. The master and slave work together as a clamp.

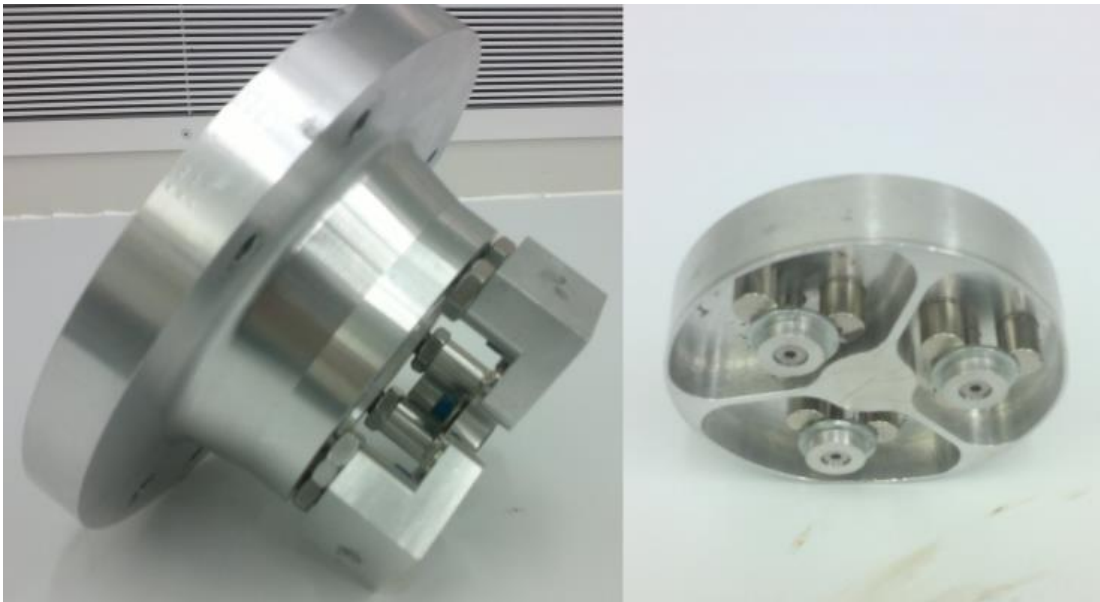


Figure 58: Master with three extended leg (left). Slave with three sets of permanent magnets (right) (Chouinard 2011)

P. Elies (Elies and Lemarquand 1999) describe radial stability characteristics in magnetic couplings transmitting a torque by an air gap separation wall in absence of any mechanical contact between the two coupling rotors. The paper proposes two cylindrical-airgap magnetic couplings structure that transmit a torque but no radial displacement or vibration from the inner rotor to the outer rotor.

A cylindrical permanent magnet can generate both axial and radial forces. Lateral sliding is the result of radial forces. J.P. Yonnet (Yonnet 1981) defined lateral magnetic stiffness while discussing different magnetic properties for permanent magnetic bearings and couplings.

The slave module laterally follows the master module motion during machining operation. This slave motion caused by the master-slave magnetic attraction force has not yet been modeled. D. Vokoun et al (Vokoun, Beleggia et al. 2009) calculated the attraction force between two cylindrical permanent magnets with a common axis considering the impact of lateral displacement on the attraction force. The force model is static and does not consider one magnet moving with respects to the other. Without a model it is not possible to predict whether the slave would accurately follow the master or experience sluggish or stick-slip motion.

This paper develops the transfer function between the master module motion and slave module motion. First a simplified model is prepared for the mechanical and magnetic components. Then classical motion equations are used to describe the slave motion where lateral magnetic stiffness has been incorporated. Experiments are then conducted to validate the transfer function model. Finally conclusions are drawn.

7.2 Transfer function modeling

A simplified 2D schematic of the system is presented in Figure 59. On top, the master module is fixed to the milling spindle outer body. The spindle is moved by a robot or a CNC machine tool. Each magnet of the slave module is subjected to a magnetic pull force F_z , out-of-plane, in the axial direction and a lateral force F_r , in-plane, in the radial direction. Both the master and slave modules are subjected to frictional forces F_{fm} and F_{fs} respectively.

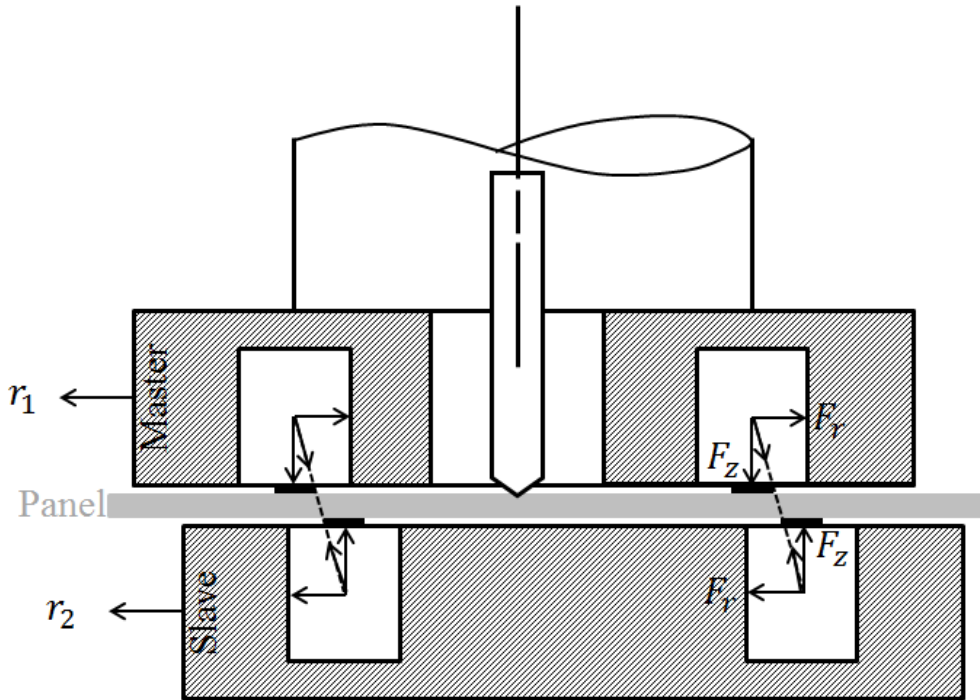


Figure 59: Master-slave magnetic forces in a simplified 2D view

This model is a two degree of freedom (in-plane and out-of-plane) mechanical system. The master module is the driver of the system. The slave module follows the master module due to the radial magnetic attraction force F_r .

The machine tool or robotic arm moves the master and causes a lateral displacement r_1 . An r_2 displacement response is imparted to the slave m_2 by the radial magnetic force F_r , ($F_r = K_r(r_1 - r_2)$) where K_r is the lateral magnetic stiffness as defined by *J.P. Yonnet* (Yonnet 1981).

A free body diagram for each of the system component (master, panel and slave) is shown in Figure 60. The master is hold by the robot by axial force $F_{robot,a}$. Master motion is dependent on the applied lateral force $F_{robot,r}$. In this analysis the robot is assumed sufficiently strong and stiff to generate the necessary force $F_{robot,r}$ to generate the desired input displacement r_1 . For the slave module the axial contact force is F_{zs} and for the master is F_{zm} which is equal to the applied axial magnetic force F_z . The cutter applies a milling thrust force F_{ma} and radial force F_{mr} to the thin skin panel.

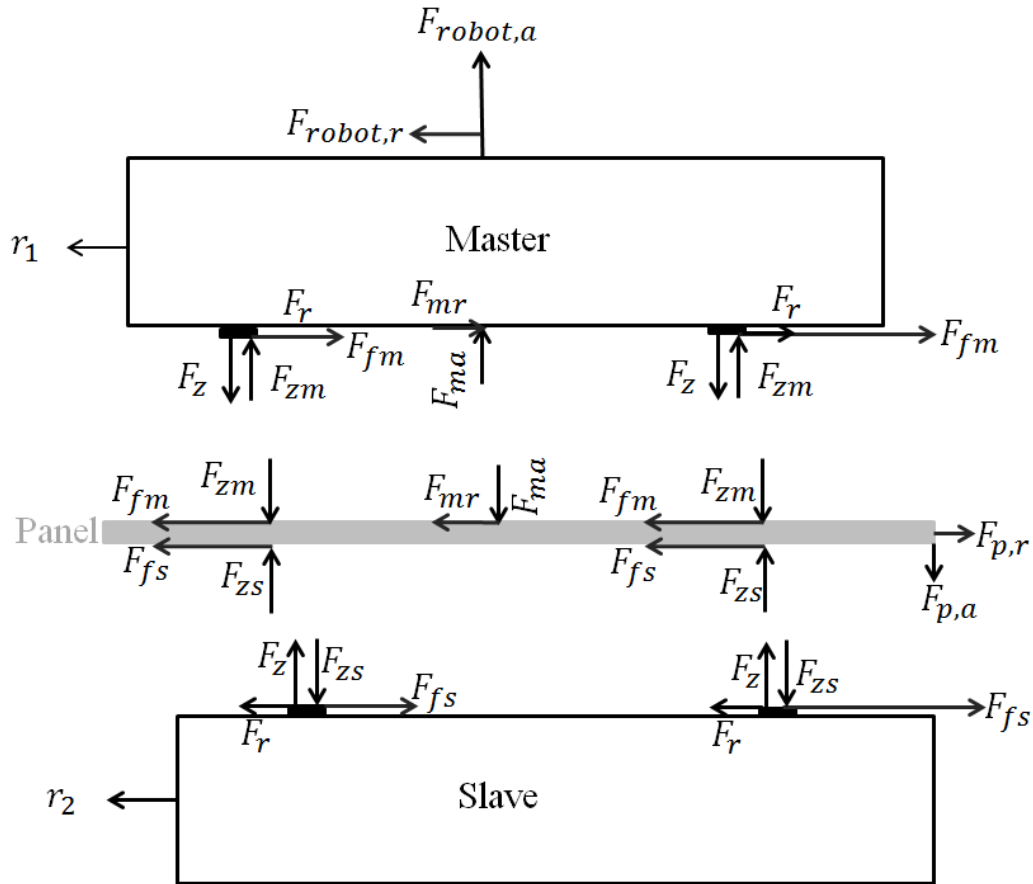


Figure 60: Free body diagram for panel-master-slave

First let's consider a simplified model without friction. If the master and slave are just pulled apart by holding the slave by a string arrangement (Figure 63 and Figure 64) without placing any plate between them there is no friction. All vertical force components can be ignored just for the time being since they do not have any contribution to lateral motion. Milling forces are ignored in the absence of milling operation. After elimination of all friction forces (F_{fs} and F_{fm}) and vertical forces (F_z , F_{zm} and F_{zs}), only the radial magnetic force F_r remains. The free body diagram is also simplified as in Figure 61.

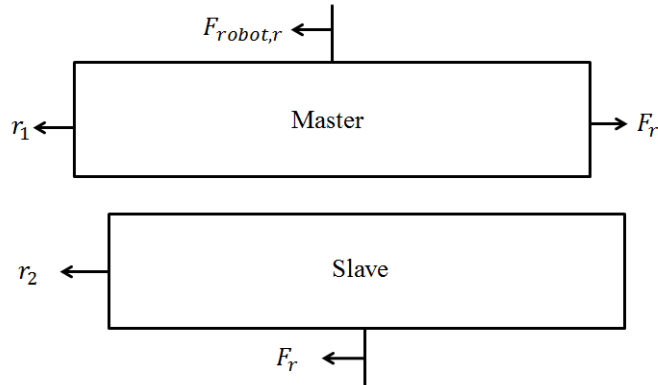


Figure 61: Modified free body diagram for master and slave

Assuming the slave has a mass m and damping coefficient C (air viscosity, string attachments) and the magnetic lateral stiffness K_r , an equivalent single degree of freedom mass-spring-damper mechanical system is used to model the system as shown in Figure 62.

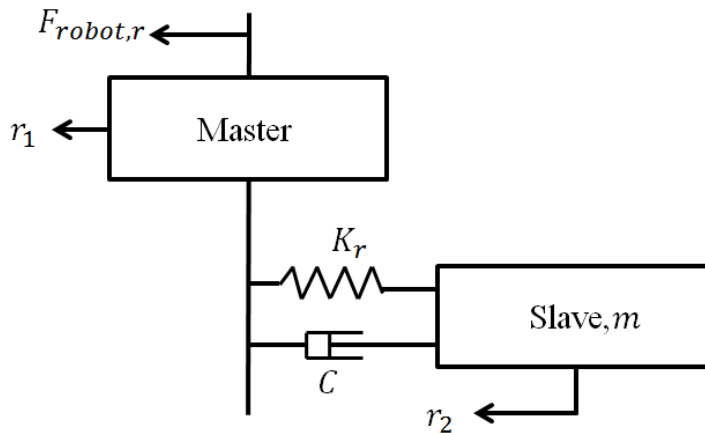


Figure 62: Master-slave equivalent mechanical system without the panel and associated friction and milling force

A single degree of freedom damped spring mass system with a moving support or base (base excitation) have been described by Rao V. Dukkipati (Dukkipati 2004). Here the master motion $r_1(t)$ is the system input so the differential equation of motion is

$$m\ddot{r}_2 + C\dot{r}_2 + K_r r_2 = C\dot{r}_1 + K_r r_1. \quad (7.1)$$

Applying Laplace transform to this equation gives (assuming zero initial conditions)

$$(ms^2 + Cs + K_r)R_2(s) = (Cs + K_r)R_1(s) \quad (7.2)$$

and the system transfer function become

$$\frac{R_2(s)}{R_1(s)} = \frac{Cs + K_r}{ms^2 + Cs + K_r} \quad (7.3)$$

We now include friction to complete the transfer function modeling. This requires considering the skin panel between the master and slave.

Sliding friction or dry friction which is considered as coulomb friction is modeled as a viscously damped system with an equivalent viscous damping coefficient (Inman and Singh 2001).

$$C_{eq} = \frac{4\mu_k F_z}{\pi\omega X} \quad (7.4)$$

where X is the approximate amplitude of the steady state motion assuming both the slave and panel surface are well lubricated ensuring a viscous medium.

$$X = \frac{F_{robot,r}}{K_r} \sqrt{\frac{1 - \left(\frac{4\mu_k F_z}{\pi F_{robot,r}}\right)^2}{\left|1 - \left(\frac{\omega}{\omega_n}\right)^2\right|}}. \quad (7.5)$$

Here ω is the frequency of motion, ω_n is the natural frequency of the slave and $F_{robot,r}$ is the driving force applied on the master causing the motion.

Equation 7.4 and 7.5 is based on the applied force $F_{robot,r}$ applied on the master. Applied driving force input is equal to the master displacement multiplied by stiffness ($F_{robot,r} = r_1 *$

K_r). So equation 7.5 can be rewritten considering master displacement r_1 as input instead of the applied force.

$$X = \sqrt{\frac{r_1^2 - \left(\frac{4\mu_k F_z}{\pi K_r}\right)^2}{\left|1 - \left(\frac{\omega}{\omega_n}\right)^2\right|}} \quad (7.6)$$

The slave applies an axial magnetic force F_z on the skin panel. For the slave the equivalent viscous damping coefficient is C_{eq} . The master to slave transfer function (equation 7.3) is rewritten with equivalent viscous damping coefficient to consider the fiction interfering during the milling operation.

$$\frac{R_2(s)}{R_1(s)} = \frac{C_{eq}s + K_r}{ms^2 + C_{eq}s + K_r} \quad (7.7)$$

7.3 System parameter identification

The slave mass m viscous damping coefficient C and lateral magnetic stiffness K_r need to be identified. The slave mass m is 0.67 kg as measured on a weighing scale.

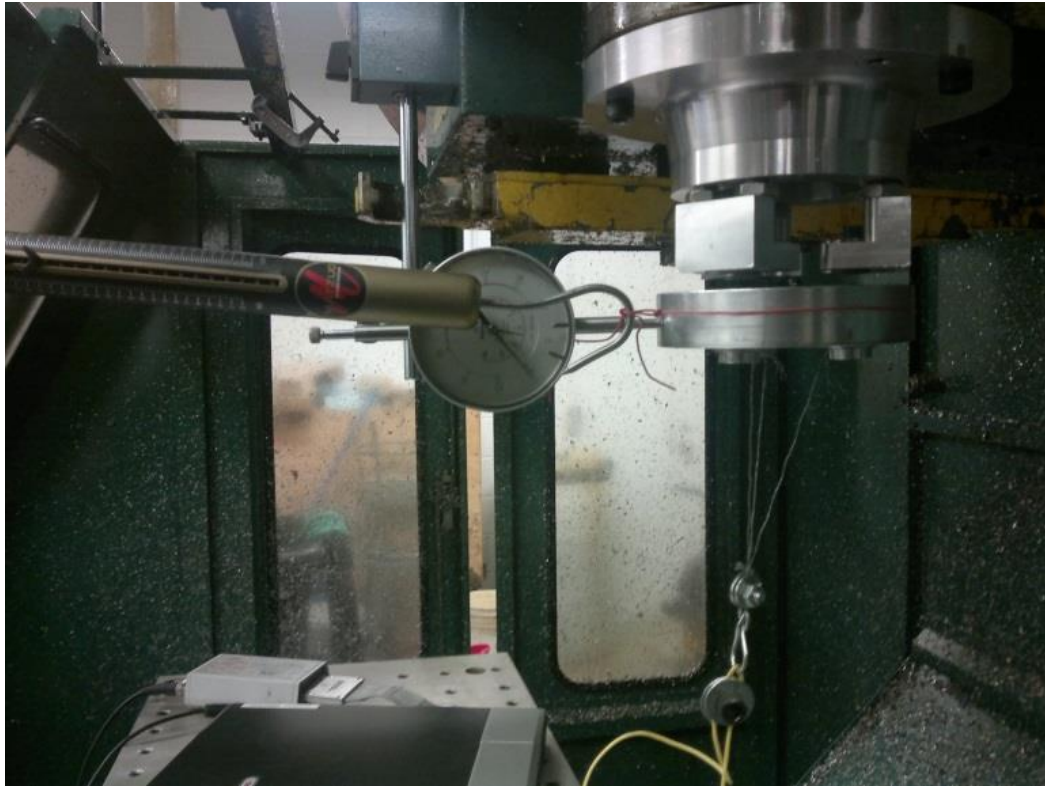


Figure 63: Lateral stiffness measurement by manual lateral force measurement with spring balance

Direct force measurement with a spring balance provides stiffness value and subsequent calculation yields the undamped natural frequency. Figure 63 shows the preliminary test setup where a gap of 5 mm is maintained by string arrangement between the master and slave which represent the thickness of a panel to machine. For a 0.003 m lateral (radial) displacement 43.51N is needed yielding stiffness ($K = \frac{F}{\delta}$) of 14500 N/m. The undamped natural frequency is calculated as

$$\omega_n = \sqrt{\frac{K}{m}} = \sqrt{\frac{1.4504E + 04}{0.67}} = 147.13 \text{ rad/sec}$$

Using the same string arrangement setup (Figure 64) a series of impact hammer test were conducted to identify the damping and lateral magnetic stiffness for different gap values.

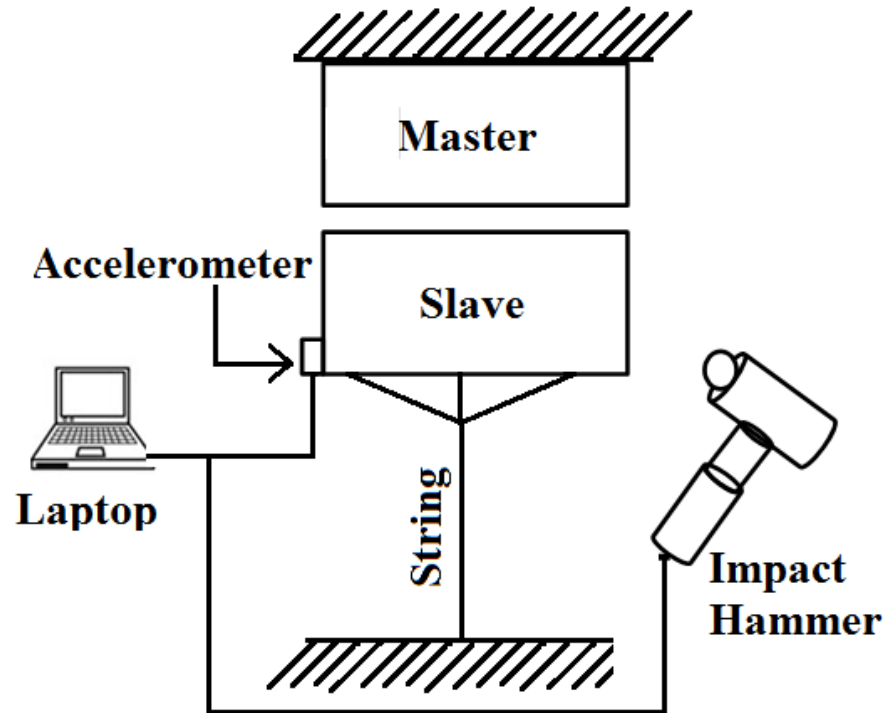


Figure 64: Test setup for system parameter identification

One miniature single axis accelerometer (model number 352C22, sensitivity 10 mV/g) and an impact hammer (model number 086D05, sensitivity 0.23 mV/N) both from *PCB PIEZOTRONICS* were connected to *MATLAB* data acquisition program via NI data acquisition card *DAQCard-AI-16E-4*. As soon as the hammer impacts the slave, vibrations are recorded. Acquired acceleration data were integrated twice to obtain the displacement data with respect to time. The calculated displacement profiles have been analyzed for slave damping and stiffness value.

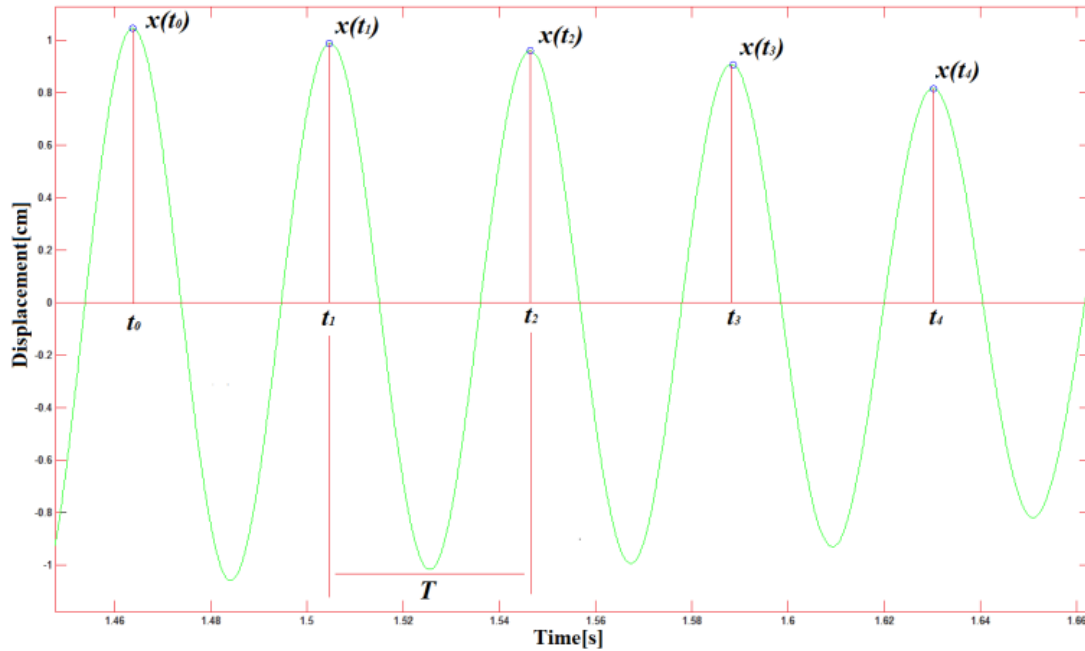


Figure 65: Displacement graph for a 5 mm gap between the master and slave

Figure 65 shows the displacement pattern for a 5 mm gap between the master and slave. Immediately after the impulse force the slave continuously vibrates at its damped natural frequency.

Logarithmic decrement δ is applied for identifying the damping ratio (Lamarque, Pernot et al. 2000).

$$\delta = \frac{1}{k} \log \left(\frac{x(t_n)}{x(t_{n+k})} \right) \quad (7.8)$$

where $x(t_n)$ is the displacement of the n th peak at the time t_n and k is the number of complete oscillation considered. R. Brincker (Brincker) converts the logarithmic decrement value to the damping ratio ζ .

$$\zeta = \frac{\delta}{\sqrt{4\pi^2 + \delta^2}} \quad (7.9)$$

The damped natural frequency ω_d is calculated using δ and the oscillation period T

$$\omega_d = \frac{\sqrt{4\pi^2 + \delta^2}}{T}, \text{ where } T = \frac{t_n - t_0}{n} \quad (7.10)$$

Then the required lateral magnetic stiffness coefficient K_r value is calculated as follows

$$K_r = \omega_n^2 m, \text{ where } \omega_n = \frac{\omega_d}{\sqrt{1 - \zeta^2}} \quad (7.11)$$

Finally, the viscous damping coefficient is

$$C = 2\sqrt{K_r m} \zeta \quad (7.12)$$



Figure 66: A 5 mm gap between the master and slave is maintained by a string arrangement

A stiffness value of $14.967\text{E}+03$ N/m (table 1) associated with a viscous damping value of 0.9090 N-sec/m has been calculated for the slave module for a gap of 5 mm between the master

and slave. This is in good agreement with the value of $K_r = 14500$ N/m obtained from the static load test.

The measured mass and stiffness values yielded a calculated natural frequency of 147.13 rad/sec for a gap of 5 mm where the accelerometer based measurement and mathematical analysis results in a natural frequency of 149.46 rad/sec.

The procedure was repeated for five gap values. Table 3 shows the results. The table also includes the natural frequency values and corresponding damping coefficients.

Table 3: System identification experiments results summary

Gap(mm)	Natural freq ω_n (rad/sec)	Stiffness K_r (N/m)	Damping Ratio ζ	Damping coeff C (Ns/m)
5	149.46	14967	0.0045	0.9090
7	108.38	7870	0.0047	0.6869
9	80.50	4342	0.0034	0.3627
11	68.05	3103	0.0034	0.3096
14	61.04	2497	0.0016	0.1307

Damping coefficient generally decreased with an increased gap. In case of stiffness a decreasing pattern is prominent. Figure 67 shows that the stiffness value is decreasing as the gap increases.

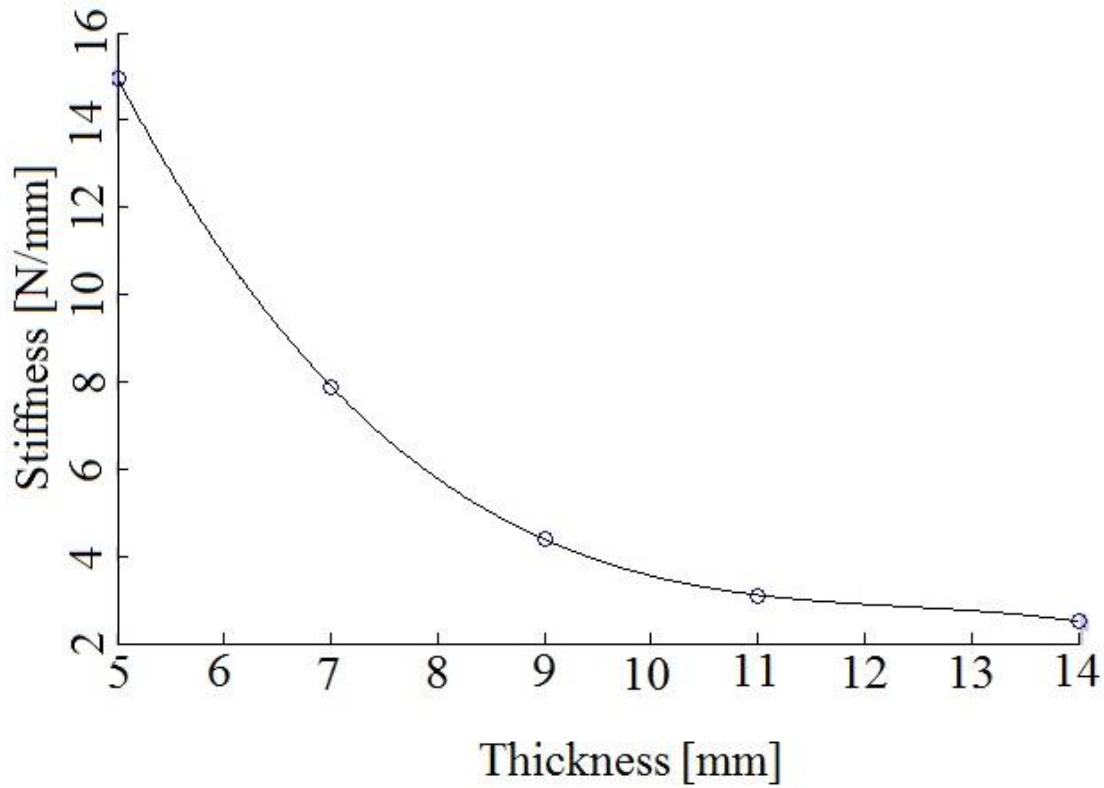


Figure 67: Stiffness reduces as the master-slave gap increases (thicker plate)

During a real milling operation the master and slave will hold the aluminum panel and friction will occur during the sliding motion. So, an experimental setup has been realized to test the friction. The plate is clamped cantilevered. Both the manual (spring balance) and accelerometer based process are used for this setup to get the friction parameter.

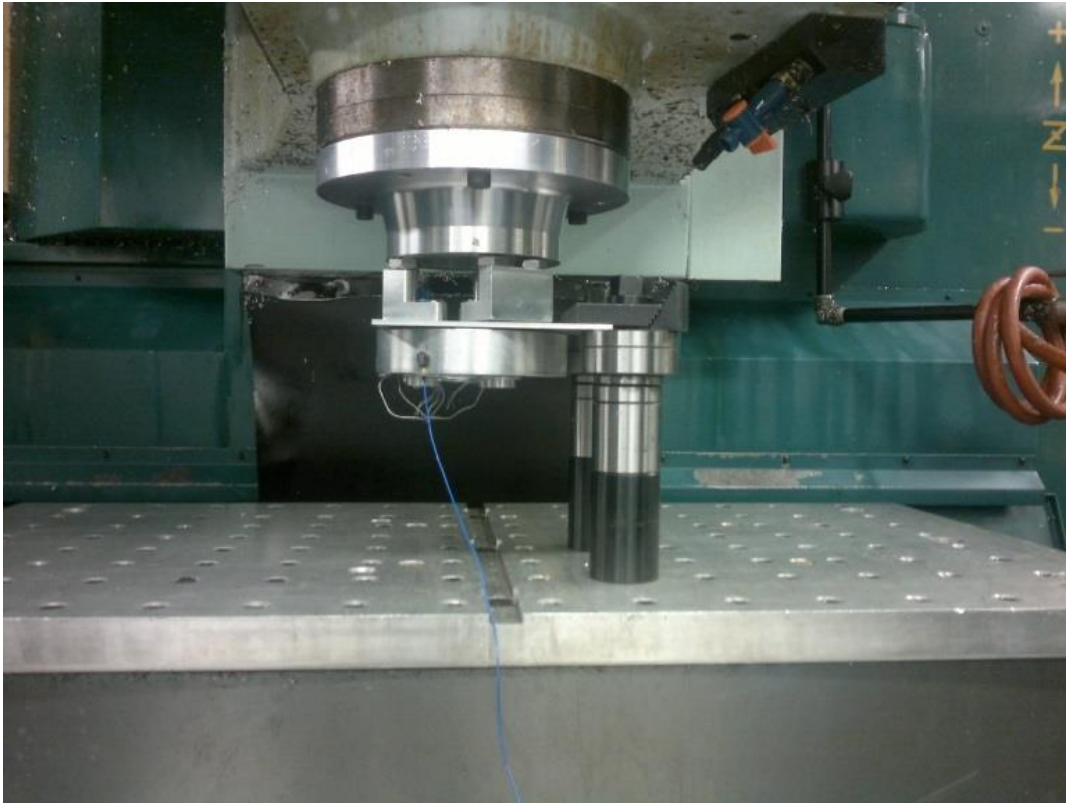


Figure 68: Plate between master and slave placed where accelerometer is positioned on the slave

A thin aluminum plate of thickness 2.54 mm with 1.25 mm slide pad on both side make a gap of 5.04 mm. The impact hammer test procedure is completed. Since the captured accelerometer data did not show any regular sinusoidal vibration pattern as shown in Figure 69, logarithmic decrement based equation was not feasible for identifying the system parameter.

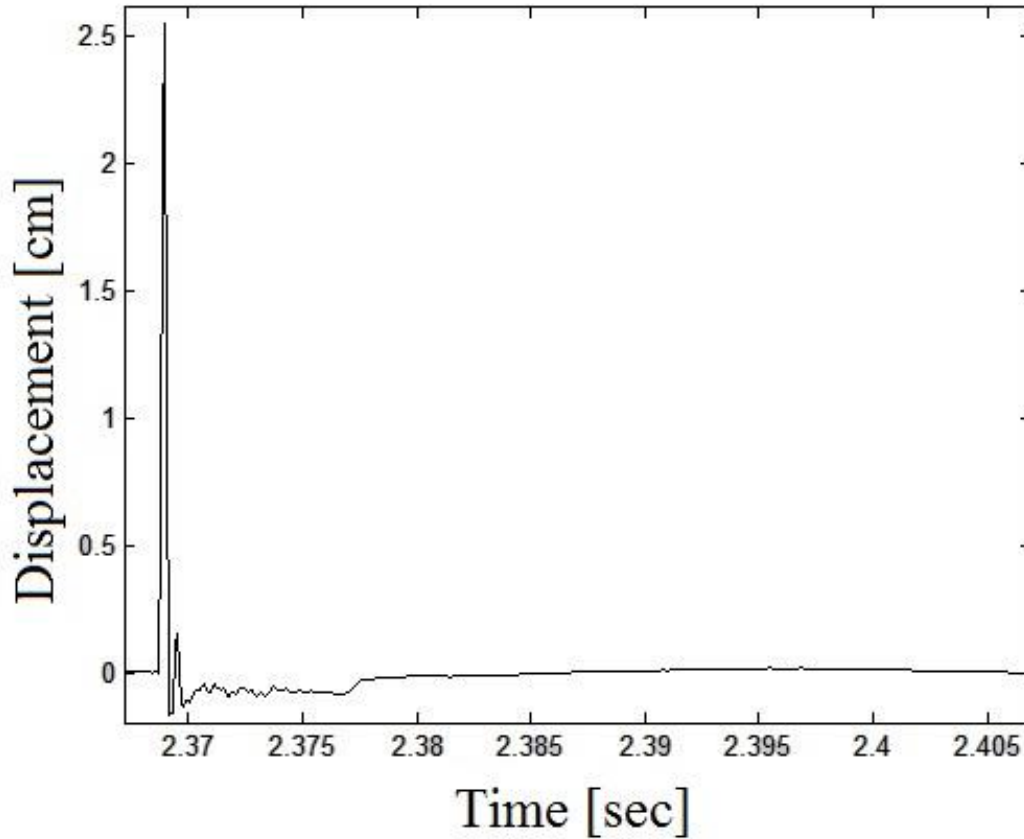


Figure 69: Slave displacement result for the impact hammer test of Figure 68

Another test has been conducted with a spring balance to measure the lateral and axial magnetic force as shown in Figure 70. At this condition spring balance direct lateral force reading is 52.92 N, and axial magnetic force, F_z force 66.64 N. Polyoxymethylene pad over aluminum panel has a friction coefficient μ_k of 0.17 (Chouinard 2011). The frictional force ($\mu_k * F_z$) is 11.32 N which is used for the calculation of equivalent viscous damping coefficient. Table 4 lists the axial magnetic force between master and slave for plates of different thickness.

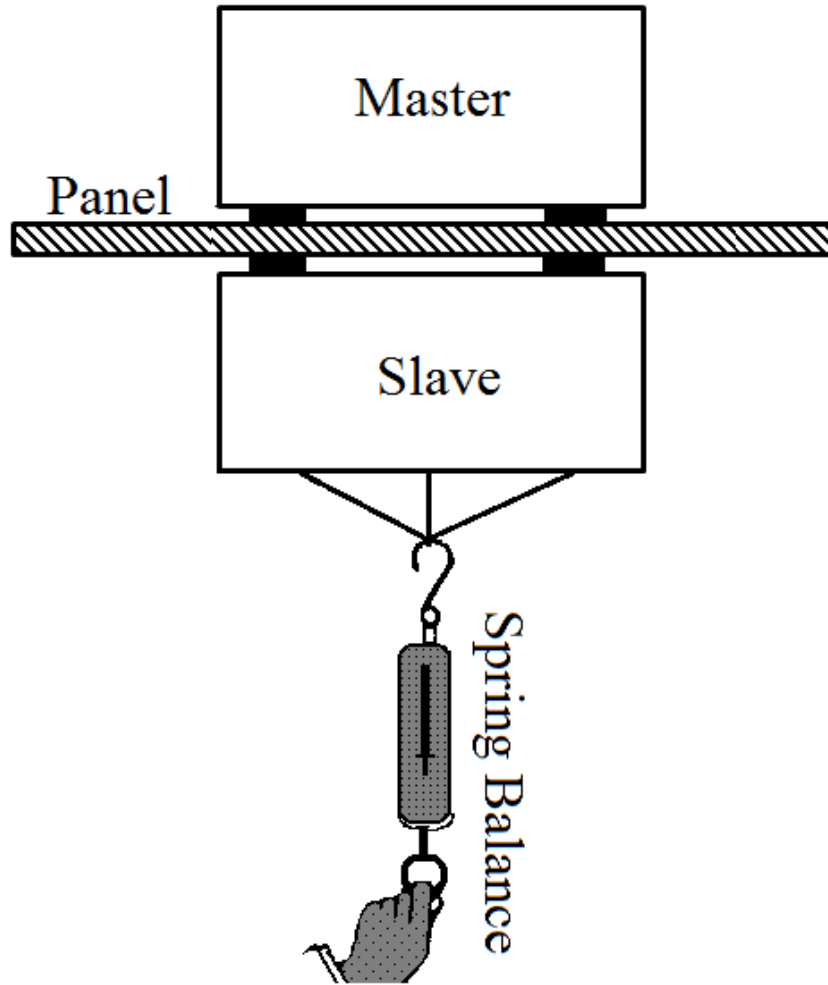


Figure 70: Test setup for axial force measurement by a spring balance

Table 4: Friction force at different plate thickness

Plate thickness (mm)	Pad thickness (mm)	Total gap (mm)	Max. axial force, F_z (N)	Frictional force ($\mu_k * F_z$) (N)
2.54	2.5	5.04	66.64	11.32
5.05	2.5	7.55	50.96	8.66
6.22	2.5	8.72	41.16	6.99
6.70	2.5	9.20	38.24	6.50

7.4 Experiments and results

The derived transfer function model does not include milling force; only magnetic attraction forces are required. So, the transfer function validation experiment is designed without milling operation.

The master was moved by manual push and pull over a skin panel with the slave following the master. Both the master and slave experienced friction.

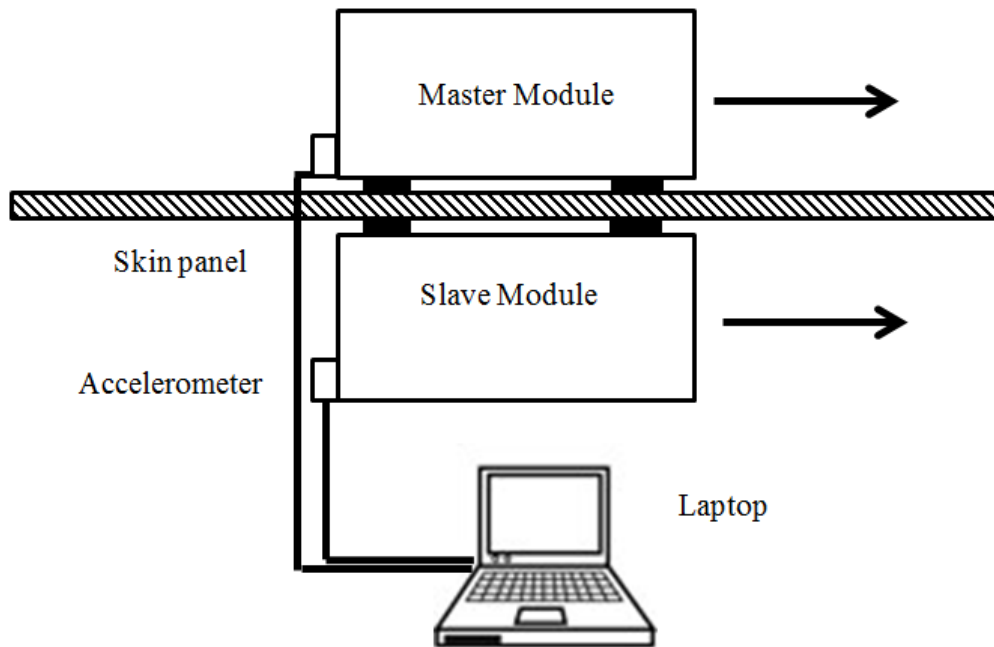


Figure 71: Simultaneous acceleration data acquisition for both master and slave

Two identical accelerometers are attached to the master module and the slave module (Figure 71). The first test is performed with a thin aluminum plate (2.54mm, pad included total master-slave gap of 5.04 mm).

Table 3 was obtained for tests without a plate between master and slave. Still, the same stiffness value would be accepted even if a plate is placed between master and slave because the stiffness is a function of distance between master and slave. This is because the stiffness is expected to come from the magnetic force and a non-magnetic plate does not influence the magnetic field. Inserting a plate would only change the damping because of friction. So an equivalent viscous damping coefficient has been calculated based on equation 7.4.

Data acquisition sampling frequency value is 10,000 Hz. Frictional force value from Table 4 has been used for calculating steady state slave motion amplitude, X . Equivalent viscous damping coefficient has been calculated for each steady state slave displacement by equation 7.6. For a 2.54 mm thick skin panel the transfer function has been defined as follows based on the transfer function model (equation 7.7).

$$\frac{R_2(s)}{R_1(s)} = \frac{C_{eq}s + 1.4966E + 04}{0.67s^2 + C_{eq}s + 1.4966E + 04}$$

Figure 72 is obtained after plotting the master and slave motion response from accelerometer reading. On the top master displacement is presented. On the bottom slave displacement is presented in a solid line. An additional dotted line is also plotted to show the simulated slave displacement based on the derived master to slave transfer function.

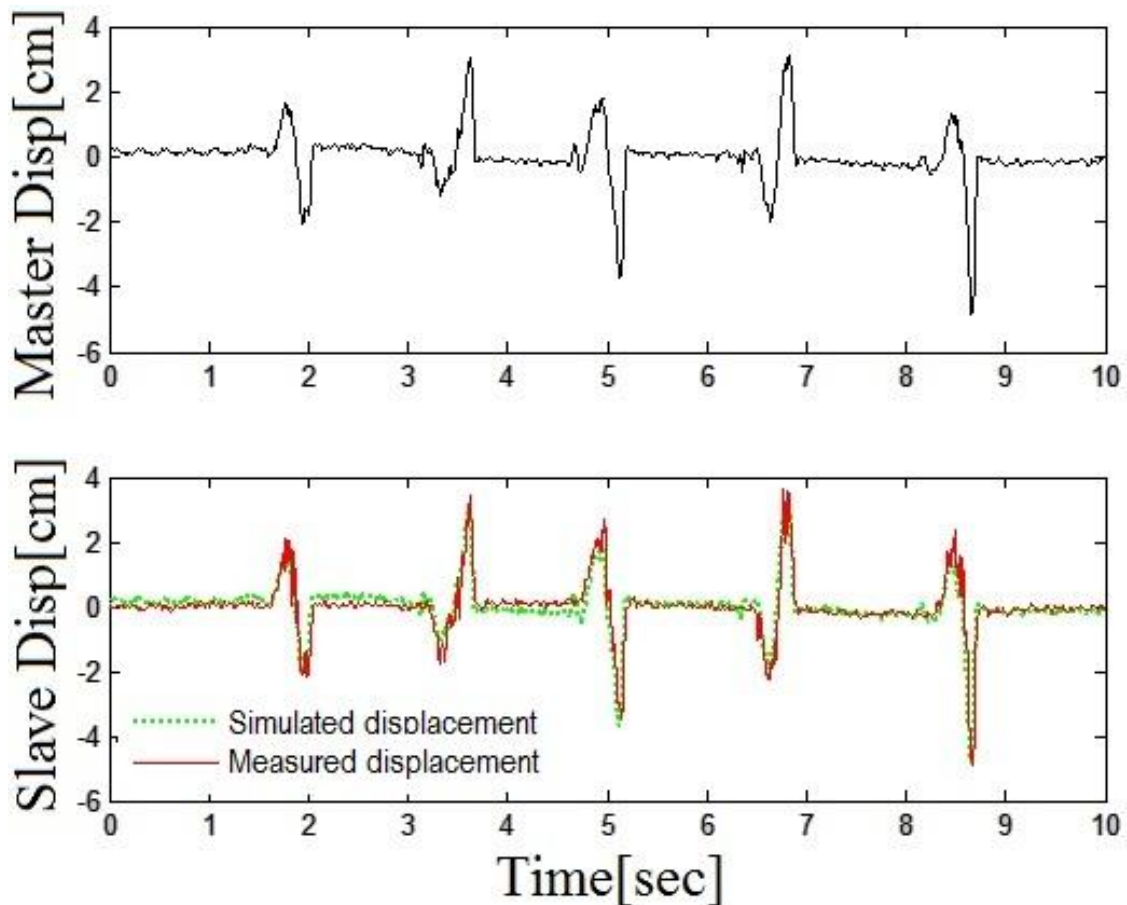


Figure 72: Comparison of transfer function based simulated motion to the actual slave motion (master slave gap 5.04 mm)

R-square value is calculated for the simulated slave displacement with respect to the measured slave displacement for a gap of 5.04 mm. An R-square value of 0.89 has been calculated showing the acceptability of the proposed slave motion model.

Magnetic stiffness was used as the prime constituent of the proposed master slave motion transfer function. Since magnetic stiffness is highly dependent on the gap between the master and slave, one more experiment has been accomplished with a thicker skin panel of 5.05 mm (total gap 7.55mm) for a reduced stiffness value of $7.8700e+03$ N/m. In this case the axial magnetic force is 50.96 N. The transfer function $R_2(s)/R_1(s)$ is still valid to predict the slave motion to an acceptable level, associated to an R-square value of 0.8340 as shown in Figure 73.

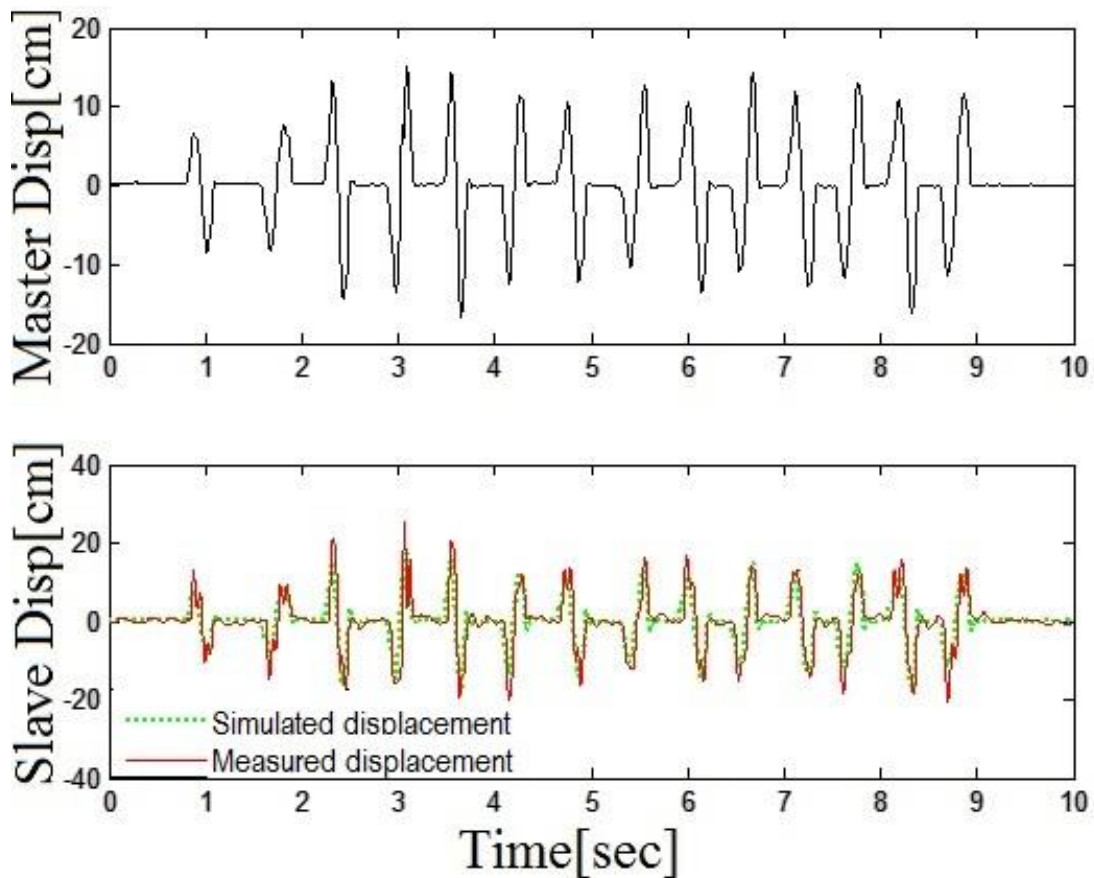


Figure 73: Comparison of transfer function based simulated motion to the actual slave motion (master slave gap 7.55mm)

7.5 Conclusion

During the skin panel milling operation the robot drive master module will follow the

instructed tool path based on the required pocket dimension, but the slave motion is depended on the magnetic attraction force against its inertia and the frictional force. A master to slave motion transfer function is proposed to calculate the slave response. The proposed transfer function based motion model was able to predict the slave position based on the input master motion.

Spring balance direct measurement provided the lateral stiffness values later verified by logarithmic decrement formula based calculation. But the most critical part of the system parameter identification is damping values. While sliding over the skin panel the slave confronts coulomb friction. Equivalent viscous damping coefficient has been used for the transfer function.

The master to slave transfer function is based on three parameter, slave mass, lateral magnetic stiffness and damping coefficient. This specific project had a slave module of 0.67 kg with an approximate lateral stiffness of 14500 N/m. Two independent experiments with different thickness skin panel have been tested to verify the transfer function model acceptability. Both of the test results satisfactorily validated the model suitability.

REFERENCES

Agashe, J. S. and D. P. Arnold (2008). "A study of scaling and geometry effects on the forces between cuboidal and cylindrical magnets using analytical force solutions." Journal of Physics D: Applied Physics **41**(10): 105001.

Altintas, Y. and P. Lee (1998). "Mechanics and dynamics of ball end milling." Journal of manufacturing science and engineering **120**(4): 684-692.

Balazinski, M., S. Gravelle, et al. (1998). Evaluation of the distance between the machining of assists for the tool tip-ring. 2nd International Conference on designing and manufacturing integrated mechanical IDMME'98 Compiegne, France: May 27-29 pp 569-575.

Bres, A., B. Monsarrat, et al. (2010). "Simulation of friction stir welding using industrial robots." Industrial Robot: An International Journal **37**(1): 36-50.

Brincker, R. "Damping estimation by frequency domain decomposition."

Cakir, O., A. Yardimeden, et al. (2007). "Chemical machining." Archives of Materials Science and Engineering **28**(8): 499-502.

Chapleau, S., É. Martin, et al. (2006). Results and Verification of Spacecraft Docking Emulation using Hardware-in-the-Loop Simulation. Romansy 16. T. Zielińska and C. Zieliński, Springer Vienna. **487**: 397-404.

Chouinard, A. (2011). Remplacement de l'usinage chimique des tooles aeronautiques minces en aluminium par de l'usinage mecanique. Departement de genie mecanique, Ecole Polytechnique de Montreal. **M Sc**.

Cubberly, W. H. and R. Bakerjian (1989). Tool and Manufacturing Engineers Handbook Desk Edition, Society of Manufacturing Engineers.

CustomPartNet (2009). "Milling Horsepower Calculator." Retrieved 14th October, 2014, from <http://www.custompartnet.com/calculator/milling-horsepower>.

Deng, H. and S. N. Melkote (2006). "Determination of minimum clamping forces for dynamically stable fixturing." International Journal of Machine Tools and Manufacture **46**(7): 847-857.

Dukkipati, R. V. (2004). Vibration analysis, Alpha Science Int'l Ltd.

Elies, P. and G. Lemarquand (1999). "Analytical study of radial stability of permanent-magnet synchronous couplings." Magnetics, IEEE Transactions on **35**(4): 2133-2136.

Gilles, P., F. Monies, et al. (2006). "Modelling cutting forces in milling on torus cutters." International Journal of Machining and Machinability of Materials **1**(2): 166-185.

Gilles, P., F. Monies, et al. (2007). "Optimum orientation of a torus milling cutter: method to balance the transversal cutting force." International Journal of Machine Tools and Manufacture **47**(15): 2263-2272.

Hamann, J.-C. (2007). Process and device for machining by windowing of non-deformable thin panels, Google Patents.

Hamann, J.-C. (2009). Process and mechanical device for machining flexible panels, in particular with a complex shape, Google Patents.

Inman, D. J. and R. C. Singh (2001). Engineering vibration, Prentice Hall Upper Saddle River.

K&J magnetics, I. (2014). "DX0X0-N52." Retrieved 14th October, 2014, from <https://www.kjmagnetics.com/proddetail.asp?prod=DX0X0-N52>.

Lamarque, C.-H., S. Pernot, et al. (2000). "Damping identification in multi-degree-of-freedom systems via a wavelet-logarithmic decrement—part 1: theory." Journal of Sound and Vibration **235**(3): 361-374.

Langdon, R. (1996). "Measurement and inspection techniques." Automotive Engineer (London) **21**(2): 4.

Li, B. and S. Melkote (2001). "Fixture clamping force optimisation and its impact on workpiece location accuracy." The International Journal of Advanced Manufacturing Technology **17**(2): 104-113.

Liu, Z., M. Y. Wang, et al. (2012). One Fast Fixture Layout and Clamping Force Optimization Method Based on Finite Element Method. ASME/ISCIE 2012 International Symposium on Flexible Automation, American Society of Mechanical Engineers.

Martinez, M. T. (1992). Machine tool installation for supporting and machining workpieces, Google Patents.

Olympus (2014). "Thickness Gages 38DL PLUS." Retrieved 14th October, 2014, from <http://www.olympus-ims.com/en/38dl-plus/>.

Panczuk, R. and P.-Y. Foissac (2010). Process and a device for the machining of panels, Google Patents.

Qin, G., D. Lu, et al. (2009). A slack-based method to clamping force optimization for fixture design. Information and Automation, 2009. ICIA'09. International Conference on, IEEE.

Ravaud, R., G. Lemarquand, et al. (2010). "Cylindrical magnets and coils: Fields, forces, and inductances." Magnetics, IEEE Transactions on **46**(9): 3585-3590.

Robertson, W., B. Cazzolato, et al. (2011). "A simplified force equation for coaxial cylindrical magnets and thin coils." Magnetics, IEEE Transactions on **47**(8): 2045-2049.

Sandvik, C. Rotating Tools and Inserts, Milling drilling Boring and Holding. Sandvik Canada INC. 5675 Royalmount Avenue, Montreal Quebec.

Scott, G. Boehm, et al. (2009) Cseries program update.

Selvakumar, S., K. Arulshri, et al. (2010). "Clamping force optimization for minimum deformation of workpiece by dynamic analysis of workpiece–fixture system." World Applied Sci J **11**(7): 840-846.

Trappey, A. and C. Liu (1992). "An automatic workholding verification system."

Vokoun, D. and M. Beleggia (2014). "Forces between arrays of permanent magnets of basic geometric shapes." Journal of magnetism and Magnetic Materials **350**: 174-178.

Vokoun, D., M. Beleggia, et al. (2009). "Magnetostatic interactions and forces between cylindrical permanent magnets." Journal of magnetism and Magnetic Materials **321**(22): 3758-3763.

Vokoun, D., G. Tomassetti, et al. (2011). "Magnetic forces between arrays of cylindrical permanent magnets." Journal of magnetism and Magnetic Materials **323**(1): 55-60.

Vučković, A. N., S. S. Ilić, et al. (2013). "Interaction Magnetic Force Calculation of Permanent Magnets Using Magnetization Charges and Discretization Technique." Electromagnetics **33**(6): 421-436.

Wang, M. Y. and D. M. Pelinescu (2003). "Contact force prediction and force closure analysis of a fixtured rigid workpiece with friction." Journal of manufacturing science and engineering **125**(2): 325-332.

Wikipedia (2014). "Neodymium magnet." Retrieved 14th October, 2014, from http://en.wikipedia.org/wiki/Neodymium_magnet.

Xiongand, C.-H., Y.-L. Xiong, et al. (2003). On Prediction of Passive Contact Forces of Workpiece-Fixture Systems. ASME 2003 International Design Engineering Technical Conferences and Computers and Information in Engineering Conference, American Society of Mechanical Engineers.

Yonnet, J.-P. (1981). "Permanent magnet bearings and couplings." Magnetics, IEEE Transactions on **17**(1): 1169-1173.

CHAPTER 8 GENERAL DISCUSSION

A magnetic grasping and milling end effector compatible with industrial robots aims at replacing current chemical methods for the machining of pockets in double curvature thin aluminum skin panels. Ensuring a smooth slave motion by avoiding stick slip is one of biggest challenge for the grasping and machining end effector. The transfer function based lateral sliding motion model can help avoiding stick slip by selecting an adequate friction constant, magnetic stiffness and slave weight. After selection of the required friction coefficient then appropriate material could be used as pad material.

Contact stiffness is important where Hertzian effect (elastic deformation of the surface due to indentation) takes place due to the clamping unit. In case of a mobile magnetic clamp, milling operation is performed on the basis of independent remaining thickness measurement. Since the measurement is independent, contact stiffness does not affect milling precision.

The range of radius of skin panel curvature varies from 24 inch to 70 inch. The grasping and machining end effector must touch the skin panel by a three point contact. The gimbal mechanism ensures the master and slave modules touch the skin panel at three contact points. The concave side of the skin panel would not face any difficulty to get the all three point in contact. However, the convex side might face the situation where the contact might be lost. A larger radius of the skin panel lowers the possibility of losing contact. CNC machine test was done on flat panel so the three point contact feature was not verified for a curved panel.

The master and slave have opposite magnetic pole (N-S-N-S) arrangement so they attract each other. Nonmagnetic aluminum Al2024-T3 skin panel is kept in-between the master and slave by their mutual attraction force. Workpiece made of magnetic material or ferrous metal cannot be machined.

Slave serves a dual purpose. First, the slave module retains the skin panel despite the thrust force by magnetic attraction force. In addition, the slave holds the sensor in position (nominal position is the tool centre point) to measure the thickness of the skin panel.

If the grasping and machining end effector provides too large clamping force that may distort the skin panel or leave rolling marks, at the three point contacts, on the panel. So the

theory of minimum clamping force is very important to keep the clamping force minimum, just enough, against the milling thrust force.

A double gimbal design allows the clamp free tilting to allow the robot to control the orientation of the cutting tool relative to the panel surface. This attribute allows the optimal use of torus milling cutter for maximum productivity.

Lateral magnetic attraction force is as important as axial magnetic attraction force. Other than the milling thrust force the slave must counteract the friction force. Selection of magnet size or internal magnet arrangement between the groups needs to be analyzed before mounting the master and slave unit.

CHAPTER 9 CONCLUSION AND RECOMMENDATION

9.1 Conclusion

Machining of shallow pockets in a thin panel is a relatively new field of study. Mechanical milling is replacing chemical milling due to lower operating cost, reduced cycle time, high precision leading to less rejection and recyclable metal chip. Industrial robotic manipulators are one of the primary technologies in industrial automation.

The main obstacle to using robot manipulator is accuracy. Here in the case of a grasping and machining end effector, the robot would only control in plane motion for pocket location which does not have tight tolerance limits. But skin panel floor thickness has a relatively high tolerance limit which would be controlled by out of plane motion aided by a machining and grasping end effector internally.

Given the initial thickness variation of 5% along with double curvature shape and low stiffness, the tolerance of ± 0.002 inch on pocket floor thickness is challenging. An ultrasonic sensor based feedback loop was integrated to cater for thickness variation. The ultrasonic sensor could not provide a continuous thickness measurement due to interrupted coupling liquid flow.

The transfer function based motion model which presents slave motion in response to master motion has influential properties. Mathematically, slave mass has been placed as a denominator in the transfer function which implies a slave with less weight will more accurately follow the master motion. The same transfer function, where K_r is presented as a multiplier which ensures a higher value in lateral magnetic stiffness, influence the slave motion in a positive manner (higher accuracy).

The pocket machined in the laboratory tests resulted in high variation of panel floor thickness with the drawback of improper edge clamping allowing twisting during machining operation. Skin panel need to be firmly gripped by proper fixture at its outer perimeter.

Lateral forces which have been predicted based on the Bessel function of first kind of order 1 showed harmony with the measured force when the lateral displacement remains within magnet radius. Outside, the measured forces have faster drop compared to prediction. Lateral sliding motion modeling without neglecting the friction force could be more valuable and

accurate, but analyzing irregular data obtained from the plate including impact test make it impossible.

An equivalent viscous damping coefficient has been used for the transfer function. The theory of minimum clamping force based on the torus milling cutter simulation may be challenged by very large force at the beginning of milling process which is highly dependent on the tool entry strategy. Tool entry strategies like ramping-in, roll-in or pilot/pre-drilled hole that can avoid this initial large force could be useful.

9.2 Recommendation

Bubbler Style ultrasonic transducers demand a continuous flow of coupling liquid (water) which was difficult in a milling scenario where lot of chips and dust obstruct the flow inside a 5 mm diameter pipe. EMAT transducer which works without couplant could be a better choice here.

Omnitrack ball transfer unit model 9101SS was selected based on the space constraint within magnets group, unfortunately not being sealed dirt and debris jammed the rolling and left rolling mark on the skin panel.

MBC12101-02 Stepper Driver which was a full step driver provided 200 steps per revolution allowed +/- 0.001 inch. Instead a micro stepping driver MBC12101 which permit 2000 steps per revolution allowing steps +/- 0.0001 inch could make milling operation smoother. The designed end effector is designed to machine double curve skin panel.

Due to cost constraint Arduino microcontroller has been used to process the command for the stepper driver. Arduino's 16MHz clock may not be fast enough. When the sensor works with 25 MHz, Arduino is not a good choice. Faster micro controller for example National Instruments 735x motion controller could be a better choice for this operation.

In the laboratory setup inside a CNC machine only X Y Z direction motion did not permit the opportunity to test double curvature machinability feature aided by double gimbal mechanism. Future work with a KUKA industrial manipulator is needed.

CHAPTER 10 BIBLIOGRAPHY

- AGASHE, J. S. and D. P. ARNOLD (2008). "A study of scaling and geometry effects on the forces between cuboidal and cylindrical magnets using analytical force solutions." *Journal of Physics D: Applied Physics* 41(10): 105001.
- ALTINTAS, Y. and P. LEE (1998). "Mechanics and dynamics of ball end milling." *Journal of manufacturing science and engineering* 120(4): 684-692.
- ANAHEIM , A. (2011). "MBC12101 - Stepper Drivers with DC Input (wiring diagram)." Retrieved 14th Oct, 2014, from <http://www.anaheimautomation.com/products/stepper/stepper-driver-item.php?sID=58&serID=15&pt=i&tID=86&cID=20>.
- BALAZINSKI, M., S. GRAVELLE, et al. (1998). Evaluation of the distance between the machining of assists for the tool tip-ring. 2nd International Conference on designing and manufacturing integrated mechanical IDMME`98 Compiegne, France: May 27-29 pp 569-575.
- BRES, A., B. MONSARRAT, et al. (2010). "Simulation of friction stir welding using industrial robots." *Industrial Robot: An International Journal* 37(1): 36-50.
- BRINCKER, R. "Damping estimation by frequency domain decomposition."
- CAKIR, O., A. YARDIMEDEN, et al. (2007). "Chemical machining." *Archives of Materials Science and Engineering* 28(8): 499-502.
- CHAPLEAU, S., É. MARTIN, et al. (2006). Results and Verification of Spacecraft Docking Emulation using Hardware-in-the-Loop Simulation. Romansy 16. T. Zielińska and C. Zieliński, Springer Vienna. 487: 397-404.
- CHOUINARD, A. (2011). Remplacement de l'usinage chimique des tooles aeronautiques minces en aluminium par de l'usinage mecanique. Departement de genie mecanique, Ecole Polytechnique de Montreal. M Sc.
- CUBBERLY, W. H. and R. BAKERJIAN (1989). *Tool and Manufacturing Engineers Handbook Desk Edition*, Society of Manufacturing Engineers.
- CUSTOM PartNet (2009). "Milling Horsepower Calculator." Retrieved 14th October, 2014, from <http://www.custompartnet.com/calculator/milling-horsepower>.

- DENG, H. and S. N. MELKOTE (2006). "Determination of minimum clamping forces for dynamically stable fixturing." *International Journal of Machine Tools and Manufacture* 46(7): 847-857.
- DUKKIPATI, R. V. (2004). *Vibration analysis*, Alpha Science Int'l Ltd.
- ELIES, P. and G. LEMARQUAND (1999). "Analytical study of radial stability of permanent-magnet synchronous couplings." *Magnetics, IEEE Transactions on* 35(4): 2133-2136.
- ELIES, P. and G. LEMARQUAND (1999). "Analytical study of radial stability of permanent-magnet synchronous couplings." *Magnetics, IEEE Transactions on* 35(4): 2133-2136.
- GILLES, P., F. MONIES, et al. (2006). "Modelling cutting forces in milling on torus cutters." *International Journal of Machining and Machinability of Materials* 1(2): 166-185.
- GILLES, P., F. MONIES, et al. (2007). "Optimum orientation of a torus milling cutter: method to balance the transversal cutting force." *International Journal of Machine Tools and Manufacture* 47(15): 2263-2272.
- HAMANN, J.-C. (2007). *Process and device for machining by windowing of non-deformable thin panels*, Google Patents.
- INMAN, D. J. and R. C. SINGH (2001). *Engineering vibration*, Prentice Hall Upper Saddle River.
- K&J Magnetics, I. (2014). "DX0X0-N52." Retrieved 14th October, 2014, from <https://www.kjmagnetics.com/proddetail.asp?prod=DX0X0-N52>.
- LAMARQUE, C.-H., S. PERNOT, et al. (2000). "Damping identification in multi-degree-of-freedom systems via a wavelet-logarithmic decrement—part 1: theory." *Journal of Sound and Vibration* 235(3): 361-374.
- LI, B. and S. MELKOTE (2001). "Fixture clamping force optimisation and its impact on workpiece location accuracy." *The International Journal of Advanced Manufacturing Technology* 17(2): 104-113.
- LIU, Z., M. Y. WANG, et al. (2012). *One Fast Fixture Layout and Clamping Force Optimization Method Based on Finite Element Method*. ASME/ISCIE 2012 International Symposium on Flexible Automation, American Society of Mechanical Engineers.

MARTINEZ, M. T. (1992). Machine tool installation for supporting and machining workpieces, Google Patents.

OLYMPUS (2014). "Thickness Gages 38DL PLUS." Retrieved 14th October, 2014, from <http://www.olympus-ims.com/en/38dl-plus/>.

PANCZUK, R. and P.-Y. FOISSAC (2010). Process and a device for the machining of panels, Google Patents.

QIN, G., D. LU, et al. (2009). A slack-based method to clamping force optimization for fixture design. Information and Automation, 2009. ICIA'09. International Conference on, IEEE.

RAVAUD, R., G. LEMARQUAND, et al. (2010). "Cylindrical magnets and coils: Fields, forces, and inductances." *Magnetics, IEEE Transactions on* 46(9): 3585-3590.

ROBERTSON, W., B. CAZZOLATO, et al. (2011). "A simplified force equation for coaxial cylindrical magnets and thin coils." *Magnetics, IEEE Transactions on* 47(8): 2045-2049.

S. SELVAKUMAR, K. P. A., K.P. PADMANABAN and K.S.K. SASIKUMAR (2010). "Clamping Force Optimization for Minimum Deformation of Workpiece by Dynamic Analysis of Workpiece-fixture System." *World Applied Sciences Journal* 11(7): 840-846.

SANDVIK, C. Rotating Tools and Inserts, Milling drilling Boring and Holding. Sandvik Canada INC. 5675 Royalmount Avenue, Montreal Quebec.

SCOTT, G. BOEHM, B. DEWAR, R. ELLIOTT, C. (2009). Cseries program update. Paris :Bombardier.

TRAPPEY, A. and C. LIU (1992). "An automatic workholding verification system."

VOKOUN, D. and M. BELEGGIA (2014). "Forces between arrays of permanent magnets of basic geometric shapes." *Journal of magnetism and Magnetic Materials* 350: 174-178.

VOKOUN, D., G. TOMASSETTI, et al. (2011). "Magnetic forces between arrays of cylindrical permanent magnets." *Journal of magnetism and Magnetic Materials* 323(1): 55-60.

VOKOUN, D., M. BELEGGIA, et al. (2009). "Magnetostatic interactions and forces between cylindrical permanent magnets." *Journal of magnetism and Magnetic Materials* 321(22): 3758-3763.

VUČKOVIĆ, A. N., S. S. ILIĆ, et al. (2013). "Interaction Magnetic Force Calculation of Permanent Magnets Using Magnetization Charges and Discretization Technique."

Electromagnetics 33(6): 421-436.

WANG, M. Y. and D. M. PELINESCU (2003). "Contact force prediction and force closure analysis of a fixture rigid workpiece with friction." Journal of manufacturing science and engineering 125(2): 325-332.

WIKIPEDIA (2014). "Neodymium magnet." Retrieved 14th October, 2014, from http://en.wikipedia.org/wiki/Neodymium_magnet.

XIONG And, C.-H., Y.-L. XIONG, et al. (2003). On Prediction of Passive Contact Forces of Workpiece-Fixture Systems. ASME 2003 International Design Engineering Technical Conferences and Computers and Information in Engineering Conference, American Society of Mechanical Engineers.

YONNET, J.-P. (1981). "Permanent magnet bearings and couplings." Magnetics, IEEE Transactions on 17(1): 1169-1173.